A NUMERICAL MODEL FOR HYDROCARBON BUBBLES FROM NATURAL SEEPS WITHIN HYDRATE STABILITY ZONE

A Dissertation

by

IN OK JUN

Submitted to the Office of Graduate and Professional Studies of
Texas A&M University
in partial fulfillment of the requirements for the degree of

DOCTOR OF PHILOSOPHY

Chair of Committee,	Scott A. Socolofsky
Committee Members,	Hamn-Ching Chen
	Steve DiMarco
	Robert Hetland
Head of Department,	Robin Autenrieth

December 2018

Major Subject: Civil Engineering

ABSTRACT

Due to the rapid vertical transportation of methane in the ocean, there is a growing concern regarding the contribution of natural gas seepage to the global atmospheric greenhouse gas budget. Hence, it is essential to understand the vertical oceanic transport of hydrocarbon gases escaping from natural seepage. The fate and transport of natural gas in water depend on the rising velocity and dissolution rates of the bubbles. Especially in the deep ocean, clathrate hydrates of hydrocarbon gases can be formed and stay stable, and it is unknown how hydrate formation may affect the fate of hydrocarbons in water. In this dissertation, we develop a numerical model to track the fate and transport of hydrocarbons released into the deep ocean. The model includes non-ideal equations of state for complex hydrocarbon mixtures and uses standard empirical correlations for rising velocity and mass transfer rates for clean and dirty bubbles. For the hydrate effects on bubbles, we hypothesize that rising velocity and mass transfer rates match those of clean bubbles immediately after release, and these rates reduce to those of dirty bubbles after a hydrate skin formation time, which depends on the initial bubble size and the hydrate sub-cooling. After the dissolution, the transport of dissolved gases in the ocean depends on the combined action of advection and diffusion. The model simulates the transport of dissolved gases based on the advective-diffusion equation with the random walk theory, and it can estimate the dissolved hydrocarbon flux through the water column. The developed model is validated by the observation of hydrate formation on bubbles from the laboratory and field experiments. The model simulation results are compared with the measurement of natural seeps, such as the rising height, the trajectory of bubbles, the spreading of bubble clouds, and the concentration distribution of dissolved methane gas. The developed model could be used to explain the hydrocarbon gases behavior through the water column within the hydrate stability zone.

DEDICATION

Dedicated to my beloved family.

For their unwavering belief, warm wishes, and endless love.

ACKNOWLEDGMENTS

The financial support offered by a grant from The Gulf of Mexico Research Initiative (GoMRI) administered through the Center for Integrated Modeling and Analysis of the Gulf Ecosystem (C-IMAGE) is gratefully acknowledged.

First, I would like to express my deepest gratitude to my advisor, Dr. Scott A. Socolofsky, for giving me the great opportunity to research with him. It is truly an honor to meet him as my Ph. D. advisor, and I have enjoyed the time working with him. His valuable suggestions and helpful advice have encouraged me to keep the motivation for studying and complete this dissertation. I also have learned many things from him not only the intellectual knowledge but also a positive role model of a good researcher. His professionalism and work ethic, and passion for teaching and research have always inspired me during my Ph. D. degree.

I would like to specially thanks to my committee members, Dr. Hamn-Ching Chen, Dr. Steve DiMarco, and Dr. Robert Hetland, for all their insightful comments and discussions for the research. They also provided me with great educational courses at Texas A&M University.

I also would like to give thanks to my research group members, Anusha, Binbin, Jonas, Kerri, Chris, Maryam, Vadoud, Katie, Alex, Meghan, Byungjin, and Soobum, for all their help and communications for the research.

Last but not least, I thanks to my best friend and the love of my life, my husband, for being there with me even when times have been tough. I would like to thanks to my parents and my parents-in-law for giving me unconditional love and believe in my life. Lastly, thanks to my beloved son, Kyle, for bringing a smile to our face every day and making me a stronger woman as a mother.

CONTRIBUTORS AND FUNDING SOURCES

Contributors

This work was supervised by a dissertation committee consisting of Professor Scott A. Socolofsky and Professor Hamn-Ching Chen of the Department of Civil Engineering and Professor Steve DiMarco and Professor Robert Hetland of the Department of Oceanography at Texas A&M University.

All work conducted for the dissertation was completed by the student, under the advisement of Dr. Scott A. Socolofsky of the Department of Civil Engineering.

Funding Sources

This work was made possible in part by a grant from The Gulf of Mexico Research Initiative to the Center for Integrated Modeling and Analysis of the Gulf Ecosystem (C-IMAGE I, II, and III).

Graduate study was supported by scholarships from the Barrett and Margaret Hindes Foundation and the American Bureau of Shipping (ABS).

NOMENCLATURE

ADCP	Acoustic Doppler Current Profiler
CTD	Conductivity-Temperature-Depth
DPM	Discrete Particle Model
GC	Gas Chromatography
GC 600	Green Canyon lease block 600
GISR	Gulf of Mexico Integrated Spill Response Consortium
GoMRI	Gulf of Mexico Research Initiative
HSL	Hydrate Stability Level
HSZ	Hydrate Stability Zone
MAPE	Mean Absolute Percentage Error
MCMC	Markov Chain Monte Carlo method
MC 118	Mississippi Canyon lease block 118
NOAA	National Oceanic and Atmospheric Administration
NODC	National Oceanographic Data Center
PDF	Probability Density Functions
ROV	Remotely Operated Vehicle
SPM	Single Particle Model
STP	Standard Temperature and Pressure
SUPR	Suspended Particulate Rosette
TAMOC	Texas A&M Oilspill Calculator
TS	Target Strength

TABLE OF CONTENTS

Page

LIST OF FIGURES

FIGURE Page

LIST OF TABLES

TABLE Page

1. INTRODUCTION

1.1 Background

The Deepwater Horizon blowout, the major oil spill accident in U.S. history, released over 4 million barrels of hydrocarbons, on the order of 1×10^{10} moles of methane, into the Gulf of Mexico over the span of 87 days. The Deepwater Horizon blowout resulted in the formation of large and deep subsurface horizontal intrusions of hydrocarbons (Richard et al. 2010, Kessler et al. 2011), and observations demonstrated that nearly all of the released methane and a significant fraction of the lighter hydrocarbons dissolved into the subsea (Ryerson et al. 2011, 2012). The plumes resulting from oil and gas spills differ from the single-phase plume because of the buoyancy of the dispersed phase (oil droplets and gas bubbles). A buoyant plume entrains ambient seawater, and it will rise until its density matches with the ambient conditions. When the ambient is stratified or a crossflow is presenting, the dispersed phase separates from the entrained ambient seawater (plume flow) due to significantly different trajectories.

In a blowout plume, the dissolution of oil and gas is the main factor setting the composition of hydrocarbons dissolved from a plume into this intruding water (Gros et al. 2017, Reddy et al. 2012, Socolofsky et al. 2011, Spier et al. 2013). The dissolution rate could affect the amount of buoyancy available to drive the near-field plume, continuously changing the near-field dynamics. In addition, the fate of hydrocarbons is vital for safety in the response zone since methane and other natural gases pose an explosion at the surface (Anderson et al. 2012). Before the Deepwater Horizon, plume models accounted for the dissolution of gas, but with some uncertainty in the effect of hydrates on the gas dissolution rate, and the dissolution of liquid oil droplets was neglected (Chen & Yapa 2001, 2004, Johansen 2000, 2003, Yapa & Zheng 1997, Yapa et al. 1999, Yapa & Fanghui 2004, Zheng & Yapa 2002). Hence, the apparent level of dissolution observed during the Deepwater Horizon accident has an essential impact on the predictions of both response-level models, and on impact assessment models.

1.2 Statement of the Problems

Hydrocarbon gas bubbles released into the ocean undergo physical and chemical processes as they rise through the water column, and the fate of each bubble depends on its rise velocity and dissolution rate (Brewer et al. n.d., Leifer & Patro 2002, MacDonald et al. 2002, McGinnis et al. 2006). Under high pressure and low temperature conditions of the deep ocean, several hydrocarbon gases, including methane (CH_4), ethane (C_2H_6), and propane (C_3H_8), and carbon dioxide (CO_2) are known to form clathrate hydrate, a solid crystalline matrix of hydrocarbon gas molecules within seawater (Sloan & Koh 2008). The depth where the temperature and pressure reach the level needed to form hydrate is known as the Hydrate Stability Level (HSL), and the water column below this depth is the Hydrate Stability Zone (HSZ). In general, the HSL for pure methane gas may exist around 530 m depth at low latitudes, and around 250 m at high latitudes based on the vertical ocean profiles of temperature (Garg et al. 2008). Other gases can form hydrates at different depths. For instance, propane hydrate forms at the lower pressure than methane for a fixed temperature. In the HSZ, the ambient temperature (T_a) is below the temperature needed to form hydrate (T_{eq}), and this difference is the degree of hydrate sub-cooling ($\Delta T = T_{eq} - T_a$). The greater the degree of hydrate sub-cooling, the greater the thermodynamic potential available to form gas hydrates.

Hydrate shells on gas bubbles can inhibit the fluid circulation within a bubble and interfere in the mass transfer between bubbles and ambient (Bigalke et al. 2010), comparable to the effect of a surfactant on the bubble (Clift et al. 1978, Fan & Tsuchiya 1990, Fan et al. 1999). Moreover, hydrates negatively impacted the response to an accidental blowout, and understanding their dynamic influence on the near-field and far-field transport is critical to response-level modeling focused on oil transport and after-the-fact impact assessment, which depends on the distribution of toxic components of the oil in the environment. Hence, the models that ignore hydrate effects may underestimate the presence of gas at the sea surface or mispredict the potential toxicity and the explosion hazard of subsea blowouts in the future. However, it is unknown to what degree hydrates formed in a plume or how hydrates may have affected the rise velocity and dissolution rates from the bubbles and droplets in a plume.

Submarine natural seeps present an idealized system where we may study the role of hydrates on bubble dynamics *in situ* in the deep ocean without the complication of a blowout plume. Natural seep is the flow of gaseous hydrocarbons from subsurface sources to the Earth's surface, and the seepage gas is composed mainly of methane and subordinately ethane, propane, and butane. Seep flares and gas bubble dynamics have been observed in several studies, and it remains a challenge to develop bubble propagation models to match the observed significant flare heights (McGinnis et al. 2006, Römer et al. 2012). These data show the observed gas bubbles rise higher in the deep ocean than the model prediction of seep flare heights. Hydrate shells inhibit mass transfer as free methane must diffuse through the shell before it can dissolve into the surrounding water. Hydrate skin formation is thought to be the main reason natural seep flares are often observed to rise to the HSL, independent of the source depth of the flare bubbles.

Despite the interest in gas hydrates as the potential future energy, the available field data is limited, and most data give an indirect measure of hydrate formation. Natural gas bubbles have been observed to form the hydrated skin or to completely convert to a hydrate matrix in laboratory experiments (Maini & Bishnoi 1981, Topham 1984). In a field experiment, Rehder et al. (2009) released methane bubbles from a remotely operated vehicle (ROV) and tracked their ascent through the water column. These data provide direct measurements of the evolving bubble location and diameter during their ascent, which can be analyzed to compute the dissolution and to infer the mass transfer. These measurements show a reduction in the mass transfer rate within HSZ. Warzinski et al. (2014) directly observed hydrate skin formation on methane bubble using high-speed imagery in a laboratory high-pressure water tunnel. They showed that hydrate shells cover bubbles on a time-scale of minutes and that cracks continuously form and refill on the bubble during ascent through the water column. Meanwhile, in field observation, Wang et al. (2016) reported the presence of hydrate shell on the bubble skin at natural seep sites in the Gulf of Mexico by using a high-speed camera. They reported the formation of hydrate occurs on a time-scale of seconds after escaping from the seafloor. Consequently, hydrate shells are expected on hydrocarbon bubbles in the HSZ, and the task remains in predicting their formation time and change of the mass transfer.

1.3 Objectives of Study

The first purpose of this study is to develop a numerical model to predict the fate and transport of bubbles when released below the HSZ in the ocean. The model uses the Lagrangian approach to track the pathways of bubbles during their rise through the water column and includes the dynamics of a bubble for the transport, such as rise velocity and mass transfer rates. We suggest a new model for hydrate skin formation on natural gas bubbles and the resulting effect of hydrates on rising velocity and mass transfer. We hypothesize that rise velocity and mass transfer rates will match those for clean bubbles immediately after release and that these rates reduce to the rates for dirty (rigid) bubbles after a characteristic time required for the hydrate shell to form. Based on observations of hydrate growth and surfactant colonization of the bubble-water interface, we choose to correlate this characteristic time with the initial bubble surface area and the degree of hydrate sub-cooling, and we refer this time-scale as a *hydrate transition time*. We calibrate our model for the hydrate transition time to the *in-situ* measurements for pure methane in Rehder et al. (2009). The predicted hydrate transition time is validated to direct observation from high-speed cameras reported for the laboratory (Warzinski et al. 2014) and for seep sites in the Gulf of Mexico (Wang et al. 2016). The calculated rise velocity and the dissolution rate are compared with the measured data in Brewer et al. (2002).

Second, we develop an approach to interpret the observed bubble rise height in the acoustic data from natural seeps on the continental margins. We focus on the ability of the model to predict the maximum flare height by comparing with the acoustic measurement of water column backscatter data, which is the most common type of natural seep observations (Weber et al. 2014). We simulate hydrocarbon bubbles from natural seeps in the Gulf of Mexico (Wang et al. 2016) and offshore Pakistan in the Arabian Sea (Römer et al. 2012). The selected natural seep sites are located below the HSZ for the natural gases present at the source. We propose three different approaches that explain where a natural seep is no longer detectable in the acoustic data and compare the performance of each method to identify the height of rising of a natural seep flare. Consequently, we suggest the optimal model for the prediction of flare height with hydrate effect. Also, the optimized model

is used to estimate the methane gas flux from methane-bubbling seep sites and its impact on the atmospheric methane gas budget, which we show to be low from these deep gas sources. These applications of the model improve the capability of bubble prediction models.

Last, we apply the model to simulate the transport of bubbles from these natural seeps and compare with the acoustic measurements for the vertical trajectory of natural seeps and the horizontal spreading of the bubble clouds. In addition, we predict the dissolved hydrocarbon concentration around natural seeps in the Gulf of Mexico and compare the model predictions to available field data that are sparse and irregularly spaced. For the simulation of natural seeps, the random walk theory is applied to the model with the measured diffusion coefficient of bubbles for these field-scale plumes. Also, the model calculates the concentration distribution of the dissolved phase using the superposition of the steady state solution of the advection-diffusion equation for a continuous line-source injection with a source for each simulated bubble. These applications of the model increase our understanding of the mechanisms controlling the fate and transport of hydrocarbons released into the ocean environment.

1.4 Dissertation Organization

This dissertation is organized as follows. Section 2 explains our new model for hydrate formation on bubble surfaces below the HSZ. We present the framework of the model, including the equations for the physical properties of bubbles, such as solubility, velocity, and mass transfer rates. In Section 3, we apply the model to predict the flare height of natural seeps with three different approaches and compare the model predictions with the observed flare heights with acoustic instruments. Section 4 describes the modeling results of the fate of hydrocarbon bubbles from natural seeps comparing with the acoustic measurements and water sampling data for natural seeps. Section 5 shows the model application to the general types of natural seeps on the continental shelf to explain the fact that the final rise height of seep bubbles are usually located around the hydrate stability level even though bubbles are released at different depths. The thesis concludes with the summary and conclusion in Section 6 followed by a set of Appendices reporting all raw data images for the model-data comparisons.

2. BUBBLE MODEL WITH HYDRATE SKIN IN THE DEEP OCEAN

Overview The fate and transport of natural gas in water, whether released from an accidental oil well blowout or a natural seep, depend on the rising velocity and dissolution rates of the bubbles. In the deep ocean, clathrate hydrates of natural gases can form due to the high-pressure and low-temperature condition, and it is unclear how hydrate skin formation may affect the fate of hydrocarbon gases in water. In this study, we present a model to track the fate and transport of hydrocarbon gases with hydrate formation effect in the deep ocean environment. The model includes the thermodynamic, chemical, and hydrodynamic properties of complex hydrocarbon mixtures in seawater with validated model parameters. For the hydrate effects on bubbles, we hypothesize that rising velocity (u_s) and mass transfer rates (β) match those of clean (mobile) bubbles immediately after release. The velocity and mass transfer rate reduce to those of dirty (rigid) bubbles after the hydrate skin form oh the surface of bubbles, the hydrate transition time depends on the initial bubble size and the degree of hydrate sub-cooling. We calibrate the model for hydrate transition time to data for pure methane bubbles in Rehder et al. (2009). The model is validated by comparing with the direct observation of hydrate formation by high-speed imagery in both laboratory and field experiments. Also, the bubble model is applied to simulate the behavior of rising CO_2 droplets having hydrate skins and confirmed the dissolution rate and the rising rate with the observation data. The developed model can explain the natural gas behaviors, the trajectory of bubbles and bubble shrinkage rate, with hydrate skin in the deep ocean environment and enhance understanding of the vertical oceanic transport of hydrocarbon gases escaping from natural seepage to the atmosphere.

2.1 Introduction

Under high-pressure and low-temperature conditions of the deep ocean, several hydrocarbon gases and carbon dioxide are known to form a clathrate hydrate, a solid crystalline matrix of gas molecules within water (Sloan & Koh 2008). The depth where the temperature and pressure reach the level needed to form hydrate is known as the hydrate stability level (HSL), and the water column below this depth is the hydrate stability zone (HSZ). In general, the HSL for pure methane gas may exist around 530 m depth at low latitudes, and around 250 m at high latitudes based on the vertical ocean profiles of temperature (Garg et al. 2008). Other gases can form hydrates at different depths. For instance, propane hydrate forms at the lower pressure than methane for a fixed temperature. In the HSZ, the ambient temperature (T_a) is below the temperature needed to form hydrate (T_{eq}), and this difference is the degree of hydrate sub-cooling ($\Delta T = T_{eq} - T_a$). The greater the degree of hydrate sub-cooling, the greater the thermodynamic potential available to form gas hydrates.

Many natural seeps in the oceans release bubbles below the HSL of the released gas composition, and hydrate skins, or hydrate armoring, have been observed on bubbles in the laboratory and the field (Römer et al. 2012, Warzinski et al. 2014). Recent high-resolution images in laboratory experiments show details of the hydrate skin formation during bubble rise and the skin dynamics, including cracking and refilling (Warzinski et al. 2014). Experiments by Warzinski et al. (2014) show that the behavior of a bubble is different between pure bubbles, which can include interfacial waves on the bubble-water interface, and hydrate-coated bubbles, which appear to have a rigid bubble-water interface. As hydrate forms on a bubble, it appears on the surface of the bubble and is moved to the downstream part of the bubble, where it accumulates. Because of these differences in the bubble dynamics at the bubble-water interact, it is possible that different parameters are required to simulate pure bubbles and hydrate-coated bubbles.

Previous bubble models have been tried to handle the change of dissolution by the formation of hydrate on the bubbles. McGinnis et al. (2006) defined the *freezing point* as the transition of dissolution rate by the hydrate, and this point occurs when the bubbles become between 2.7 and 4 mm in diameter. Rehder et al. (2009) observed the rapid transition in dissolution behavior by

hydrate nucleation, and they used the observed transition points from the data sets to implement the simulation using the bubble propagation model described in Leifer & Patro (2002). Sun et al. (2017) used the hydrate nucleation time to control the hydrate formation time based on the initial thermodynamic condition when the bubble is released. However, they validated their model only for the specific range of the initial water depth (1,000 - 1,500 m). None of the previous studies derived the general form of the transition time and validated in the various water depths from shallow to deep.

In this study, we develop a numerical model for the prediction of fate and transport of bubbles when released in deep ocean environments with hydrate formation on the surfaces of bubbles. The developed model uses the Lagrangian approach to track the pathways of bubbles during their rise through the water column. In addition, we suggest a new model for hydrate skin formation on natural gas bubbles and the resulting effect of hydrates on rising velocity and mass transfer. We hypothesize that rising velocity and mass transfer rates will match those for clean bubbles immediately after release and that these rates reduce to the rates for dirty (rigid) bubbles after a characteristic time required for the hydrate shell to form. Based on observations of hydrate growth and surfactant colonization of the bubble-water interface, we choose to correlate this characteristic time with the initial bubble surface area and the degree of hydrate sub-cooling, and we refer it as a *hydrate transition time*. We calibrate our model for the hydrate transition time to the *in-situ* measurements for pure methane in Rehder et al. (2009). The hydrate transition time prediction is validated to direct observation from high-speed cameras reported for the laboratory (Warzinski et al. 2014) and for seep sites in the Gulf of Mexico (Wang et al. 2016). The calculated rising velocity and the dissolution rate are compared with the measured data in Brewer et al. (2002).

This section is organized as follows. Section 2.2 explains the model framework including the equations for the physical properties of bubbles, such as solubility, velocity, mass transfer rates. The model for the transition time due to hydrate formation on bubbles is given and calibrated to the measured data in Section 2.3. The model validation is presented in Section 2.4, followed by the conclusions in Section 2.5.

2.2 Bubble Model

We use the Texas A&M Oilspill Calculator (TAMOC) to conduct all simulations presented in this study. TAMOC is an integrated modeling suite developed for predicting the behavior of petroleum fluids released from subsea sources in the oceans (Dissanayake et al. 2018). TAMOC is coded in Python and Fortran and is freely available from http://github.com/socolofs/tamoc. TAMOC contains modules for predicting fluid particle properties (Discrete Particle Model, DPM) and for tracking individual fluid particle (Lagrangian Particle Model, LPM). Here, *fluid particle* refers to both liquid droplets and gas bubbles. Other modules within TAMOC provide integral models for simulating strong blowout plumes, both in stratification and crossflow. Since we are interested in natural seeps at weak gas flow rate with limited entrained water and ambient crossflows, the coupled DPM and LPM were used for the work in this study.

2.2.1 Discrete Particle Model (DPM)

TAMOC calculates the thermodynamic, chemical, and hydrodynamic properties of the individual fluid particle in seawater and applies their predicted dynamics to the particles along their path. This method is known as the Discrete Particle Model (DPM) approach in multiphase plume literature. Wüest et al. (1992) first introduced the DPM for modeling aeration plumes in lakes and reservoirs, and the method was further developed for lakes by Bryant et al. (2011), Little & McGinnis (2001), McGinnis et al. (2004), and Singleton & Little (2006). McGinnis et al. (2006) adapted the DPM to non-ideal gases for predicting methane dissolution from seeps in the Black Sea; which is very similar in the approach used in TAMOC. The main differences between TAMOC and the model in McGinnis et al. (2006) are in the way hydrates are treated. There are also some minor differences in choices for the thermodynamic equations-of-state and a few other particle properties, but although different methods are used, similar results are attained for these elements of both models. A brief overview of the solution used in TAMOC follows.

2.2.1.1 Fluid Particle Shape and Circulation

Hydrodynamic properties of fluid particles, including rising velocity and mass transfer rates, depend on their shape and boundary conditions at the water-particle interfaces (Clift et al. 1978, Haberman & Morton 1953). The shape of fluid particles can be grouped into different regimes, based on the value of dimensionless numbers. Fluid particle shapes vary from spherical to ellipsoidal to spherical-cap depending on the particle size and the properties of the particle and ambient water. Clift et al. (1978) correlate particle shape with several dimensionless numbers which can describe fluid particle characteristics. These includes the Eötvös number (Eo), the Morton number (M), the Reynolds number (Re):

$$\begin{aligned} Eo &= \frac{g(\rho - \rho_p)d_e^2}{\sigma} \\ M &= \frac{g\mu^4(\rho - \rho_p)}{\rho^2\sigma^3} \\ Re &= \frac{\rho d_e U}{\mu} \end{aligned} \tag{2.1}$$

where g is the acceleration of gravity [L/T^2], ρ is the density of water (continuous phase) [M/L^3], ρ_p is the density of fluid particle [M/L^3], d_e is the equivalent spherical diameter [L], σ is the interfacial tension with seawater [M/T^2 or F/L], μ is the dynamic viscosity [M/LT or FT], and U is the velocity of fluid particle [L/T]; the subscript p denotes a property of the fluid particle (dispersed phase) and the unsubscripted terms represent the properties of the water (continuous phase).

There is some ambiguity regarding the boundaries of the ellipsoidal shape regime. We use the parameter H defined in Clift et al. (1978) to help define the boundaries

$$H = \frac{4}{3} Eo M^{-0.149} \left(\frac{\mu_p}{0.0009} \right)^{-0.14} \tag{2.2}$$

where μ_p is the dynamic viscosity of fluid particle [M/LT or FT]. The boundary between spherical and ellipsoidal particles is taken as $H = 2$; spherical-cap particles are assumed when $Eo > 40$ or $M > 0.001$ or $H > 1,000$. Ellipsoidal-shaped particles are assumed between these two boundaries.

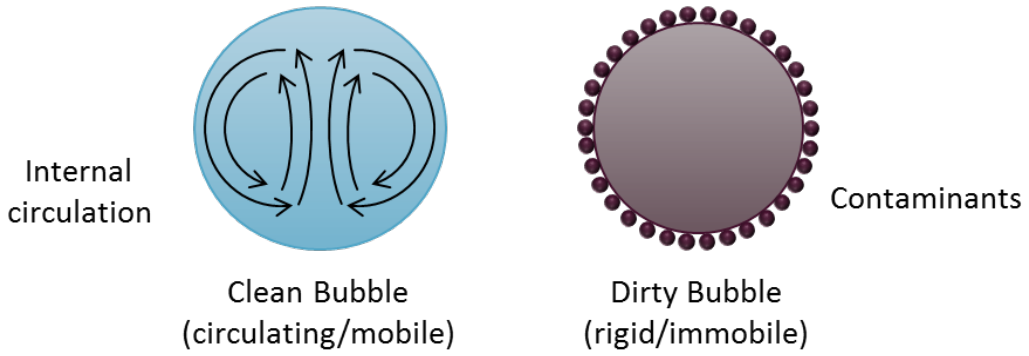

Figure 2.1: Schematic diagram of clean and dirty bubble.

The mobility at the water-particle interface determines the circulation inside a bubble or droplet. When the interface is flowing, internal circulation occurs, and rising velocity and mass transfer rates are maximized. On the other hand, if the interface is rigid, there is no internal circulation. In this case, the no-slip boundary condition on the rigid interface gives larger drag and a lower rising velocity. The lack of internal circulation also stops the internal convection, leading to slower mass transfer rates. The rigid interface can occur for solid particles, fluid particles with solid shells, and for fluid particles in contaminated systems. For contaminated particles, naturally occurring surfactants populate the water-particle interface and the gradients of the concentration of these surfactants on the interface produce *Marangoni* forces, which arrest the interfacial motion. Because surfactants are ubiquitous in nature, bubbles or droplets in the environment become contaminated quickly after they are released. Moreover, since the primary mechanism for fluid particles to behave as rigid is by surfactant contamination, we refer particles with moving interfaces as *clean* bubbles or droplets and particles with rigid interfaces as *dirty* bubbles or droplets. Figure 2.1 explains the difference between the *clean* bubble and the *dirty* bubble.

Both clean and dirty fluid particles have different correlation equations for rising velocity and mass transfer rates. Differences between these rates are largest for ellipsoidal particles, which are in size range of about 3 to 8 mm diameter for natural gas bubbles in the oceans across a wide range of depths. This is a typical bubble size observed at natural seeps; hence, both clean and dirty fluid particle behavior may be observed for bubbles from natural seeps.

2.2.1.2 Mixture Equation of State

The fundamental thermodynamic properties needed to simulate the fate of hydrocarbon fluid particles include density, fugacity, solubility, diffusivity, viscosity, and surface tension. TAMOC uses the Peng-Robinson equation of state to predict the fluid density and fugacity (McCain 1990, Michelsen & Mollerup 1986). The Peng-Robinson equation of state with volume translation accounts for the non-ideal behavior of the compressible gas and liquid hydrocarbons in complex mixtures at high-pressure and low-temperature (Peng & Robinson 1976, Robinson & Peng 1978, Gros et al. 2016). The solubility is computed from the modified Henry's law, with the correction for temperature and pressure following King (1969) and the correction for salinity using a Setschenow salting out coefficient (Schwarzenbach et al. 2003).

Molecular diffusivity, dynamic viscosity, and surface tension are computed from correlations in the literature (Danesh 1998, Hayduk & Laudie 1974, Pedersen et al. 2015). Some of these correlations depend on the properties of seawater, which we obtain from the seawater equation of state in Millero & Poisson (1981) and from correlations summarized in Sharqawy et al. (2010). Hydrocarbon mixtures are represented in the DPM module by their explicit composition on a component mass basis. The properties of the pure compounds needed by these equations of state and correlations (e.g., critical point properties, acentric factors, Henry's law constants, Setschenow constants, the heat of solution, molar volume at infinite dilution) are distributed in a database within TAMOC. For the mixtures of light gases, these thermodynamic constants were obtained directly from data in the literature (McCain 1990, Poling et al. 2001).

The equation of state in TAMOC is validated by a wide range of literature data for both pure compounds and hydrocarbon mixtures. An example that combines several thermodynamic properties and that is critical for the fate of gas bubbles from natural seeps is the solubility of methane. Figure 2.2 compares the estimated solubility of pure methane gas in water using TAMOC to data from the literature and to an industry standard model for thermodynamic properties of petroleum fluids, the Multiflash program by Infochem (https://www.kbc.global/software/simulation-and-optimization/advanced-thermodynamics). Figure 2.2(a) illustrates the solubility

of methane as a function of pressure under the fixed temperature of 4 °C and 25 °C, and Figure 2.2(b) shows the variation of methane solubility as a function of temperature at atmospheric pressure (1 atm). Multiflash uses a similar equation of state but includes data assimilation to yield better performance.

As a measure of model error, we report the mean absolute percentage error (MAPE), which is the mean absolute relative error expressed as a percentage. For Figure 2.2(a), TAMOC has a MAPE of 11 % at 4 °C and 3.9 % at 25 °C; Multiflash has a MAPE of 4.9 % and 5.4 % for these two temperatures, respectively. For Figure 2.2(b), the MAPE of TAMOC is 7.9 % and that of Multiflash is 5.5 %. Multiflash with data assimilation is somewhat better than TAMOC overall. However, both models slightly overestimate solubilities compared to the measurements and have a similar order of magnitude in their errors and similar biases. The percentage error in TAMOC of less than 10 % in most cases is acceptable for our purposes. Hence, the equations of state in the model yield good performance for the integrative property of solubility.

2.2.1.3 Slip Velocity

The DPM module calculates the terminal rising velocity, or slip velocity u_s, of bubbles or droplets using the correlation equations in Clift et al. (1978). For dirty particles, these equations are summarized in Zheng & Yapa (2000), and we follow the criteria in Section 2.2.1.1 to define the particle shape and then apply the correlations for the corresponding shape regime. The clean particle slip velocity $u_s|_{clean}$ is evaluated from the dirty particle velocity $u_s|_{dirty}$ following the expression from Clift et al. (1978)

$$u_s|_{clean} = u_s|_{dirty} \left(1 + \frac{\Gamma}{1+\kappa}\right) \tag{2.3}$$

where $\kappa = \mu_p/\mu$ (viscosity ratio) and Γ is evaluated from their Figure 7.7. The equation for Γ is not provided in the reference, and we approximate Γ from their figure as

$$\Gamma = 2\exp\left[\frac{-(\log_{10}\chi + 0.6383)^2}{(0.2598 + 0.2(\log_{10}\chi + 1.0))^2}\right] \tag{2.4}$$

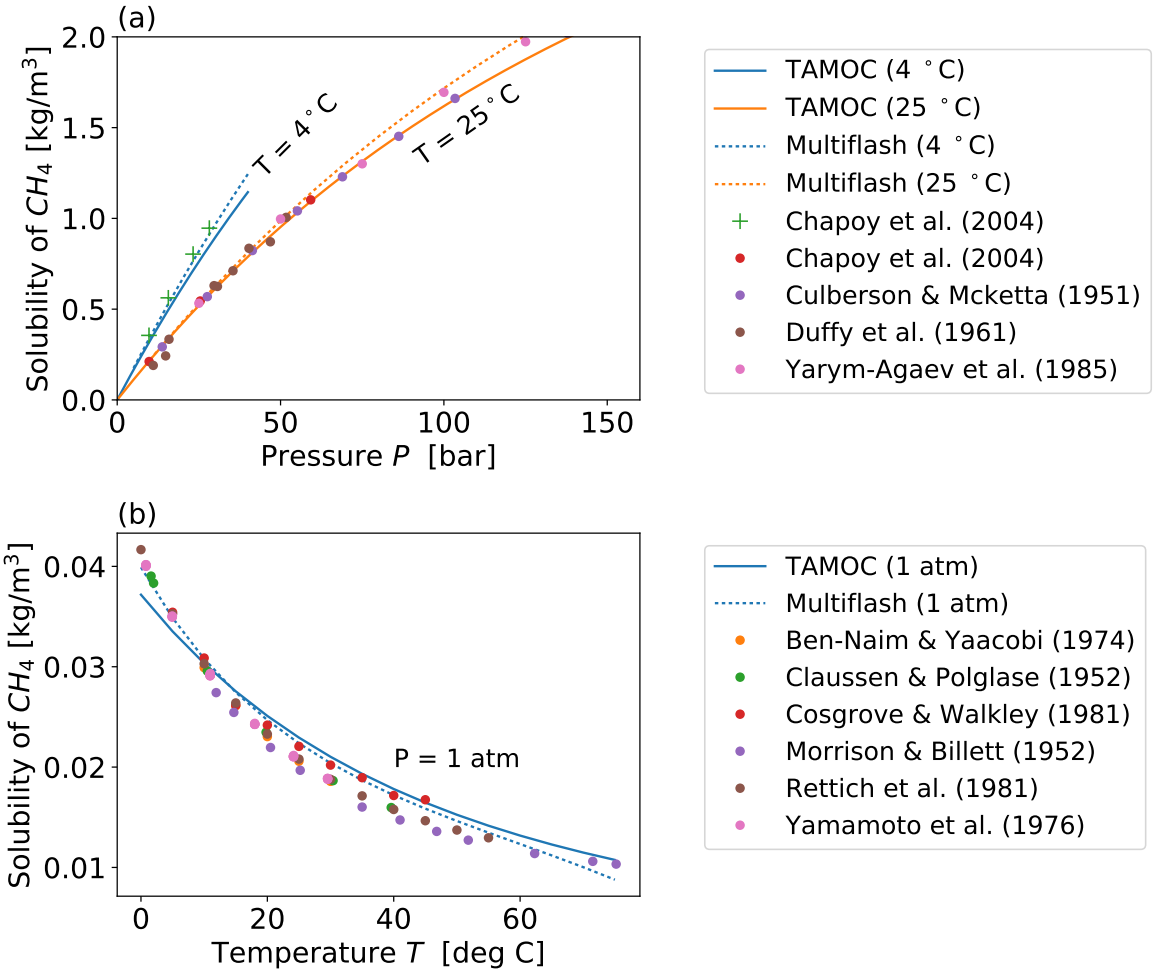

Figure 2.2: Solubility of methane gas (C_{s,CH_4}) in TAMOC, Multiflash and laboratory data (a) at 4 °C or 25 °C, and (b) at 1 atm.

where $\chi = Eo(1 + 0.15\kappa)/(1 + \kappa)$. Together, these equations are applicable to oil droplets, gas bubbles, and hydrate particles.

We validate the correlation equations across the full range of particle shape (spherical, ellipsoidal, and spherical cap) and interface conditions (dirty and clean) for air bubbles. Figure 2.3(a) shows the comparison of model and data for the slip velocity of air bubbles rising in water at STP condition (20 °C and 1 atm). Circles represent data for clean (circulating) bubbles, and pluses denote data for dirty (rigid) bubbles. The curve for the model prediction for clean bubble slip velocity is designed to predict the maximum envelope of measured values in the clean bubble regime. Hence, the figure shows that most of the clean bubble slip velocities fall below the curve, which is the expected behavior. The MAPE is found to be 16 % for the clean bubble and 6.6 % for the dirty bubble predictions across the full parameter space of the figure. These error percentages are a similar order of magnitude to that of the solubility. Moreover, some of this error is contributed from the variation of the measured data. For tracking bubbles rising in the ocean water column over time periods of a few hours, these errors are in an acceptable range.

The slip velocity of CO_2 droplet is also validated with and without hydrate at different P-T conditions (Figure 2.3(b), which compares with experimental data of rising CO_2 droplets from Bigalke et al. (2008)). Bigalke et al. (2008) demonstrate the impact of hydrate skin on the slip velocity of CO_2 under simulated oceanic conditions inside and outside the hydrate stability zone, which can also be captured by our model prediction. The rising velocity of CO_2 with hydrate is well predicted by the model for a dirty bubble, while that without hydrate appears to be lower than the value for a clean bubble, but higher than the dirty-bubble rising velocity. As mentioned previously, since the model for a clean bubble is developed to predict the maximum envelope of measured values in the clean bubble regime, this difference between measurements and the model is not unexpected, and the results suggest that bubbles with hydrate skins appear to rise at dirty bubble slip velocities while bubbles without hydrate skins behave as clean bubbles.

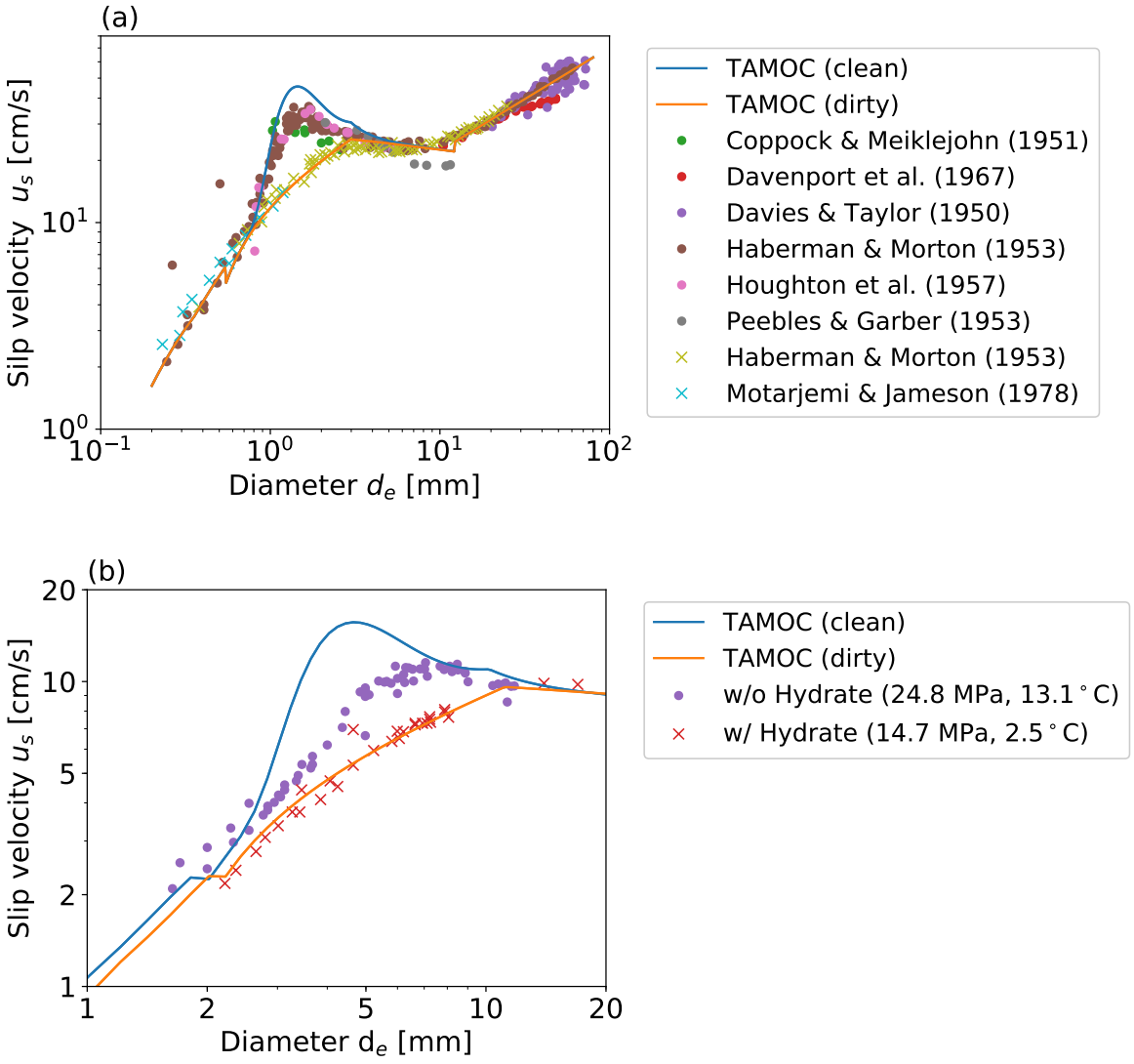

Figure 2.3: Slip velocity (u_s) of (a) air bubbles for clean and dirty status (• and ×), and (b) CO_2 droplets with and without hydrate formation (• and ×) by using σ_{CO2} = 33.77 dyne/cm from Bozzano & Dente (2014).

2.2.1.4 Mass Transfer

Similar to slip velocity, mass transfer rates are different for clean and dirty particles. TAMOC combines correlation equations for mass transfer from Clift et al. (1978) and Johnson et al. (1969). Equations for dirty particles follow Clift et al. (1978), with spherical and ellipsoidal particles modeled by correlations for solid spheres and spherical-cap particles by a separate correlation. Johnson et al. (1969) give a correlation for clean particles valid over the full shape regime from spherical to spherical-cap. For some cases, the Johnson et al. (1969) correlation predicts slower mass transfer than those using the dirty-particle equations in Clift et al. (1978); in those cases, TAMOC uses the higher prediction as the mass transfer coefficient, so that mass transfer rates for clean particles could never be smaller than those for dirty particles.

The mass transfer coefficient is an empirical parameter that gives the bulk gas transfer velocity averaged over the surface of a fluid particle, and this coefficient depends on hydrodynamics and diffusion coefficient (Clift et al. 1978). The dissolution process is occurring at the water-particle interface, inside of a non-uniform concentration boundary layer surrounding the particle. Turbulent motion in the continuous phase transports dissolved material away from the particle. Integrated over the particle surface, the total mass transfer rate (dissolution) from a particle to dissolved form can be described by the empirical Ranz-Marshall equation:

$$\frac{dm_i}{dt} = -A\beta_i \left(C_{s,i} - C_{a,i}\right) \tag{2.5}$$

where m_i is the flux of a component i inside the particle (e.g., methane) [M], A is the surface area of the particle [L^2] , β_i is the mass transfer coefficient of compound i [L/T], $C_{s,i}$ is the solubility of component i at the water-particle interface [M/L^3], and $C_{a,i}$ is the concentration of component i far away from the particle [M/L^3]. The parameter β groups the physical process of turbulent transport around the bubble together with the thermodynamic process of molecular diffusion at the water-particle interface. Since we express dm_i/dt in terms of $C_{s,i}$ and $C_{a,i}$ we are explicitly assuming that there is adequate methane transport inside the particle to maintain the concentration $C_{s,i}$ at the

interface; hence, we assume the mass transfer is limited on the seawater side of the particle. This is a valid assumption for gas bubbles that have efficient mixing within their boundaries.

We can compare measurements of β for different gases in different systems using the dimensionless expression for mass transfer rate (dissolution), given by the Sherwood number (Sh)

$$Sh = \frac{\beta de}{D} \tag{2.6}$$

where D is the molecular diffusivity of the dissolving compound in seawater at the ambient conditions [L^2/T]. The dimensionless quantities are useful since it can be predicted from other dimensionless numbers which describe the physical properties of the fluid particle. Figure 2.4 shows the validation for the Sh values predicted by TAMOC compared to measured data from the literature over a wide range of d_e. The MAPE values are found to be 20.8 % for clean CO_2, 21.4 % for clean O_2, and 48.3 % for dirty O_2. These larger apparent errors compared to those for solubility and slip velocity are due to the greater uncertainties in the measured data. The clean particle model solution appears to have little bias compared to the data in the figure; the dirty particle solution is biased a little low compared to the Vasconcelos et al. (2002) data, but lies above the Aiba & Toda (1964) data; hence, the model predictions are well within the trends of the data.

The correlation equations in Clift et al. (1978) and Johnson et al. (1969) each predict Sh. To convert the estimates of Sh to mass transfer coefficient β, the diffusivity D at local conditions is required. As described in Section 2.2.1.2, we estimate D from Hayduk & Laudie (1974), which depends on the viscosity of seawater and the molar volume of the dissolving compound at its normal boiling point. Since each of the light compounds emitted in natural seep gases is included in the calibration and validation data used by Hayduk & Laudie (1974), the error due to errors in estimating the diffusivity will be small for the results presented herein.

2.2.2 Lagrangian Particle Model (LPM)

Using the particle properties from the DPM, the Lagrangian Particle Model (LPM) tracks the evolution of individual bubbles or droplets rising through the water column. The LPM simulates

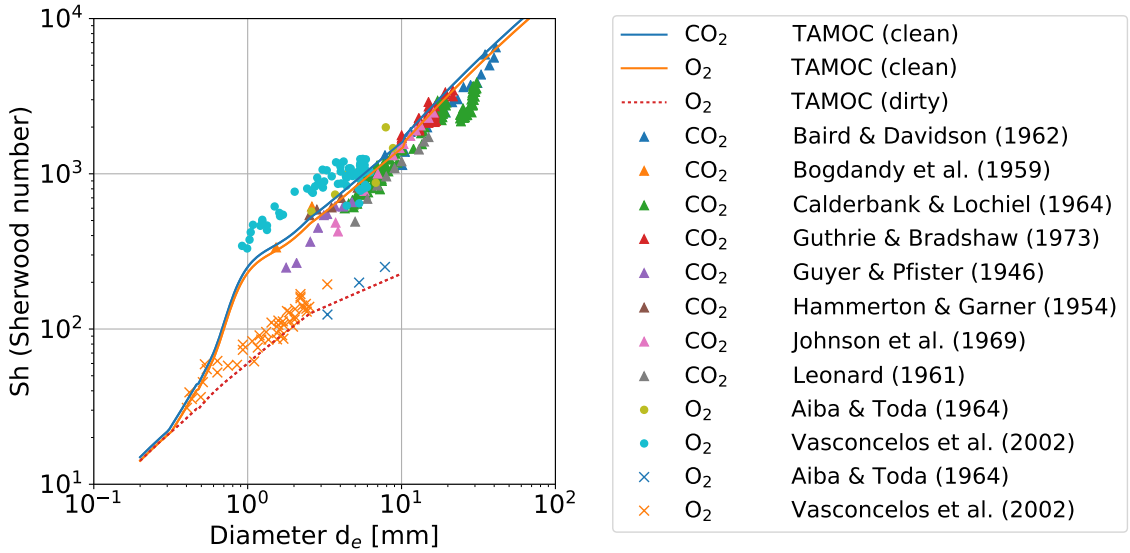

Figure 2.4: Sherwood number (Sh) for clean CO_2 ($\triangle$), and clean and dirty O_2 ($\bullet$ and $\times$) bubbles in water at STP condition (20 °C and 1 atm).

the rising bubble or droplet by the advection equation for a single particle coupled with the mass transfer equation for each chemical component in a particle and the heat transfer equation for the whole particle. These equations yield a coupled set of non-linear Ordinary Differential Equations (ODE), which are solved with a variable step size numerical solver designed for stiff ODEs (the VODE integrator with backward differentiation formulas available in the SciPy package of Python). Figure 2.5 shows the Schematic diagram of LPM.

2.2.2.1 Trajectory of Bubble

The mean trajectory of a stream of particles is assumed to be the superposition of the vertical slip velocity computed for a stagnant ambient and three-dimensional the ambient current velocity. This advection equation ignores random walk due to turbulence and is expressed as

$$\frac{d\vec{x}}{dt} = \vec{u} + u_s\vec{k} \tag{2.7}$$

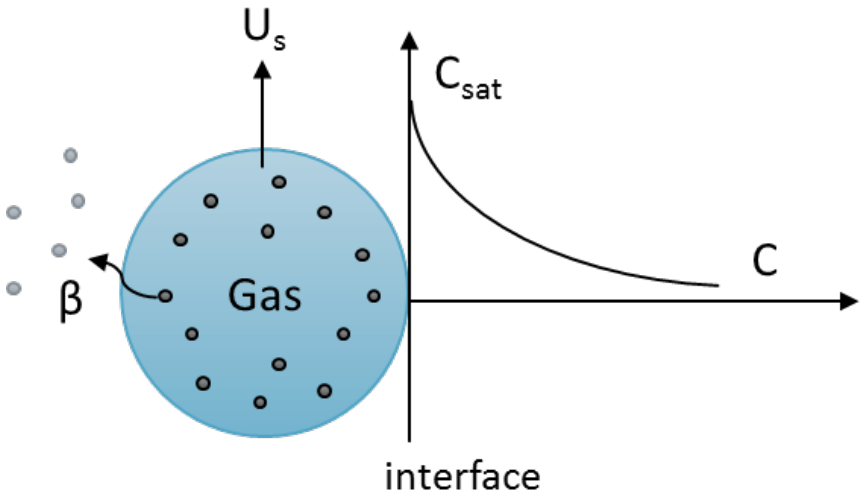

Figure 2.5: Schematic diagram of Lagrangian Particle Model (LPM): β is the mass transfer rate, u_s is the slip velocity of fluid particle relative to the ambient seawater, C_{sat} is the solubility of component at water-particle interface, and C is the ambient concentration of component far way from the particle.

where $\vec{x}$ is the vector position of the particle [L], $\vec{u}$ is the vector velocity of the ambient current [L/T], and $u_s\vec{k}$ is the slip velocity of the bubble or droplet relative to the ambient seawater [L/T], taken in the vertical direction only ($\vec{k}$). This equation predicts well the centerline trajectory of bubbles rising from a natural seep during steady current conditions. On the continental shelf in the Gulf of Mexico, mean ocean currents include a diurnal inertial oscillation, with current direction continuously changing. In the present work, we have considered these ambient currents to be steady over time-scales of six hours or less. Because the rise time for particles from the seafloor to their maximum height of rising is a few hours, we use averaged current data to predict the steady flare trajectory and update our simulation predictions with new current data every six hours. In Section 4, we also include a random-walk capability to the model to track the pathways of individual bubbles; in that application, however, we perform particle tracking with the same time-average mean currents that are updated every six hours.

2.2.2.2 *Dissolution of Bubble*

Mass transfer depends on the mass transfer coefficient, surface area, and the driving potential, as shown in Equation 2.5. The total mass transfer from the bubble or droplet is simulated through Equation 2.5 expressed for each component in the mixture. The mass transfer equations are coupled to the advection equation through the slip velocity, which depends on particle properties (e.g., particle density, particle size), the mixture composition, and ambient conditions. Hence, together the DPM and LPM can simulate the evolving composition and trajectory of natural gas bubbles released in the deep ocean. Figure 2.6 shows the flow chart of the bubble model in TAMOC.

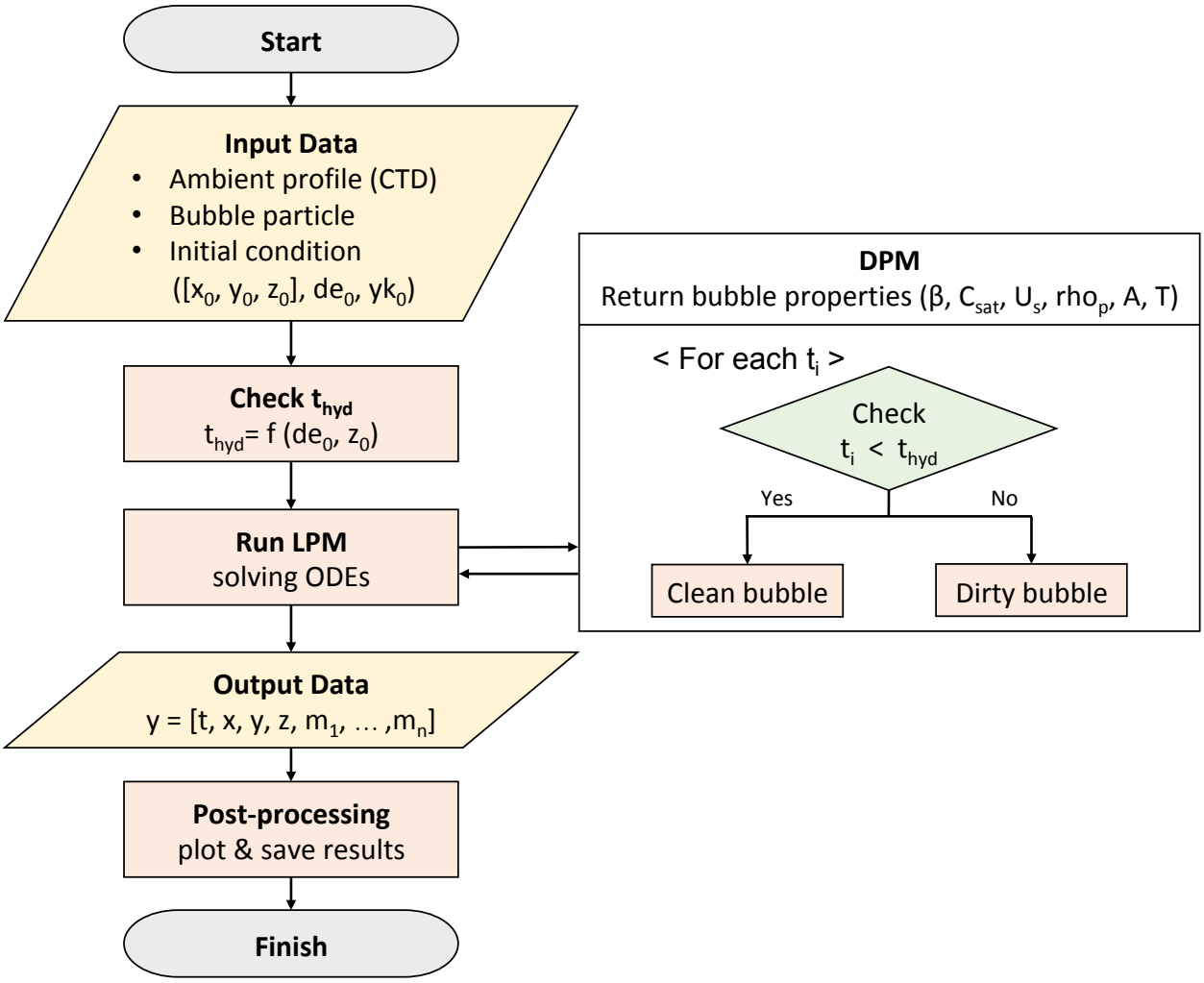

Figure 2.6: Schematic diagram of flow chart of bubble model in TAMOC.

2.3 Model Development for Hydrate on Bubbles

2.3.1 Hypotheses of Model

We propose a hypothesis here to study the effects of hydrate formation on the mass transfer. We hypothesize that seep bubbles behave as clean bubbles for slip velocity and mass transfer immediately after they are released, and the slip velocity and mass transfer rate will reduce to that for dirty bubbles after a characteristic time required for the bubble-water interface to be colonized by a surfactant or covered by hydrate. We will refer to this time as the transition time (t_{trans}). Although free gas must diffuse through the hydrate film to dissolve into seawater after hydrate formation, the model hypothesizes that diffusion away from the interface into seawater is the rate-limiting step because free gas can leak through cracks in the hydrate shell and because the hydrate shell may be thin. Hence, we postulate that the mass transfer rate is equivalent to the dirty bubble rate after hydrate formation. Our model calculates seep bubble properties from correlations for clean bubbles until the transition time (t_{trans}) and computes bubble properties from dirty bubble correlations thereafter. Figure 2.7 shows the schematic diagram of the model for seep bubbles within HSZ.

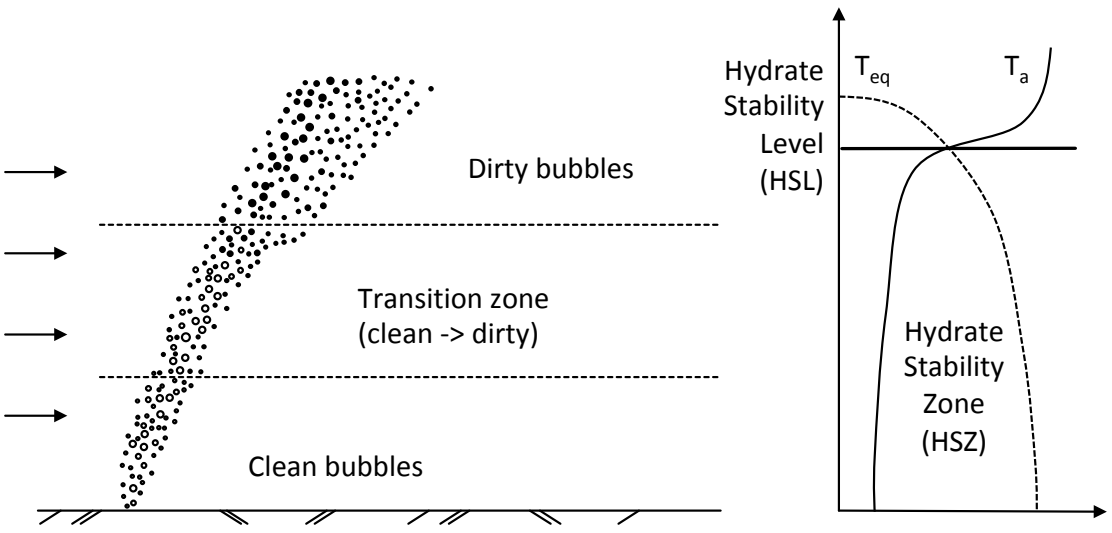

Figure 2.7: Schematic diagram of the model for bubbles emitted from a natural seep located within HSZ.

To predict the transition due to hydrate formation, we consider models for surface contamination in the literature. Jähne et al. (1987) observed the transition of bubble behavior due to surfactants, and Vasconcelos et al. (2002) suggested that the transition time for surfactant contamination depends on the initial bubble size and gas concentrations in the water. McGinnis et al. (2006) used a similar approach, with a calibrated fast and slow mass transfer rate for clean and dirty bubbles. They postulated that hydrate could not cover the top surface of a bubble until the bubble shrinks to a certain size, calibrated as 3.5 mm diameter in their model. Here, we hypothesize that the hydrate formation process is similar to surfactant contamination depending on the surface area of the bubble, but that hydrate can cover bubbles of any size after an appropriate length of time. We further expect that the formation time may be accelerated as hydrates become more thermodynamically favorable at deeper depths. In our model, hydrate stability is accounted for using the degree of hydrate sub-cooling, and the model computes T_{eq} based on the K_{vsi} method in Sloan & Koh (2008). Hence, we assume a general form of the hydrate transition time model (t_{trans}) as

$$t_{trans} = \alpha A_i \Delta T^{\beta} = \alpha(\pi d_{e,i}^2)\Delta T^{\beta} \tag{2.8}$$

where t_{trans} is the mass transfer transition time in [mm^2], $d_{e,i}$ is the initial equivalent spherical diameter in [mm], and ΔT is the degree of hydrate sub-cooling at the release depth in [K]. The coefficients α and β will be obtained by model calibration with the data in the following Section.

2.3.2 Model Calibration

2.3.2.1 Data for Hydrate Formation Time

Following a similar approach for modeling the bubbles within HSZ from McGinnis et al. (2006) and Rehder et al. (2009), we used the field experimental data obtained by Rehder et al. (2002) to calibrate our predictive model for hydrate formation time. Rehder et al. (2002) released pure methane bubbles in Monterey Bay from a remotely operated vehicle (ROV) and observed bubble shrinkage through the water column during rising using ROV video cameras, and Rehder et al. (2009) reported the detail information of measurement data which is used for the model calibra-

tion. We collect all datasets from Rehder et al. (2009) and McGinnis et al. (2006) to enhance the accuracy of the model calibration.

Figure 2.8 shows the ambient water column data used for the simulation. The temperature profile is from Rehder et al. (2009). The salinity and dissolved oxygen (O_2) profiles are adopted from McGinnis et al. (2006), which is the CTD data from a 1991 cruise within the WOCE project (code: 225) near Monterey Bay. NODC cruise ID is US-12540 for this data set, and it is available from the National Oceanographic Data Center (NODC) website. The dissolved Argon (Ar) and Nitrogen (N_2) profiles are calculated using standard atmospheric equilibrium assumptions following Exline et al. (2006) because of a lack of field measurements. To do this, we compute the aqueous solubility of air at the air-water interface (atmospheric pressure) and then correct for seawater compressibility at all water depths. Computed Ar and N_2 profiles through the water column are close to that predicted by Pilson (2013), Hamme & R. Emerson (2004), McGinnis et al. (2006).

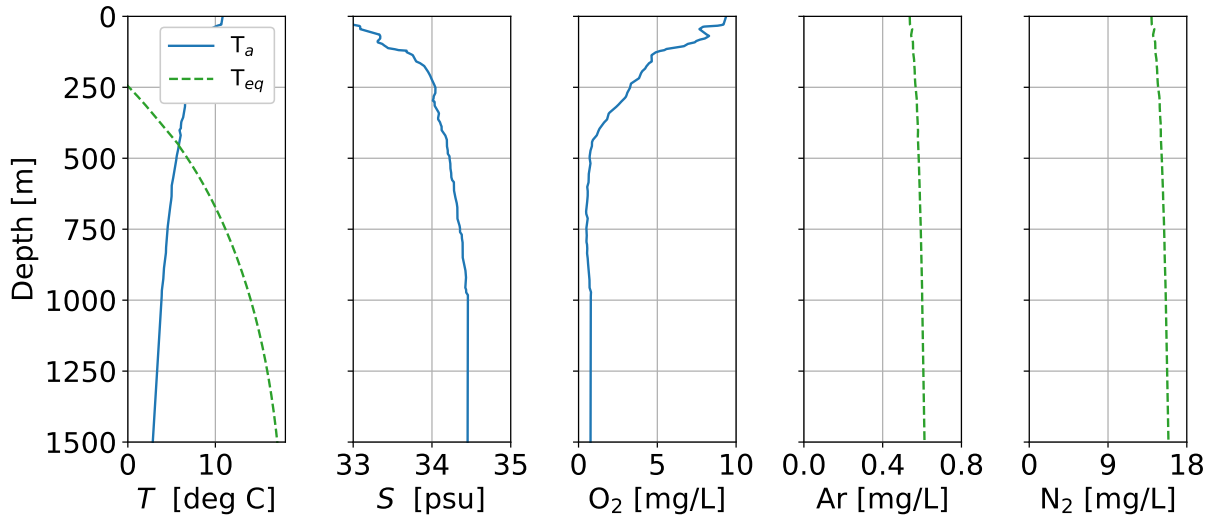

Figure 2.8: Ambient profile of temperature (T), salinity (S), and dissolved oxygen, argon, and nitrogen (O_2, Ar, N_2) in Monterey Bay, CA. The blue solid line indicates measured data, and the green dashed line represents calculated values. T_a is the ambient temperature and T_{eq} is the hydrate stability curve for the gas mixture.

Table 2.1: Parameters for adjusting the bubble release depth.

Case	$z_{i,\ data}$ [m]	$de_{i,\ data}$ [mm]	$t_{i,\ data}$ [sec]	$u_{s\ i,\ model}$ [cm/sec]	$z_{i,\ adjusted}$ [m]
590	587.7	6.4	38	23.9	596.8
593	593.8	7.4	53	23.5	606.3
704	683.3	9.2	57	22.8	696.3
802	799.0	6.2	5	23.8	800.2
825	824.6	5.0	117	24.6	853.4
1209	1,207.5	7.0	70	23.1	1,223.7
1495	1,492.5	6.2	160	23.3	1,529.7
1511	1,509.7	5.8	190	23.5	1,552.3

Rehder et al. (2009) reported the depth of their first measured data point for each bubble, and it is different from the actual release depth since there is a time gap between the release point and the first measurement. We back-calculate the release depth based on their reported depth of the first data point, the reported time gap from each release to the first measurement, and the calculated slip velocity for the clean bubble at the first data point. Table 2.1 summarizes the parameters for adjusting the bubble release depth for each case. Based on the measured bubble sizes (column 3), we calculate the slip velocity for the clean bubble (column 5). We use this rising velocity as a constant to calculate the rising height during the time between the bubble release and the first measurement (column 4), which is added to the reported measurement depth (column 2), obtaining the bubble release depth (column 6).

2.3.2.2 Model Calibration Procedure

We applied the probabilistic Bayesian calibration with the Markov Chain Monte Carlo (MCMC) method to figure out the initial bubble size ($d_{e,i}$) and the transition time (t_{trans}) parameters in the bubble model with the dataset from Rehder et al. (2009). The goal of this calibration is to sample the *posteriori*, which updates our background knowledge based on relevant evidence (Denison et al. 2002). The posteriori of model parameters ($P(\theta|E)$) can be expressed as

$$P(\theta|E) = \frac{P(E|\theta)P(\theta)}{P(E)} \tag{2.9}$$

where θ is the model parameters, and E represents the observed data which features the bubble size along the time in this study. The *prior* ($P(\theta)$) defines the range of each parameter based on our background information of dataset to control the random variation. From the iterative process of calibration, the MCMC algorithm randomly generates both the bubble size and the transition time parameters and optimize the non-linear regression within the range of our given priors. We define the objective function from the quantified error between the observed data and the modeling data by the TAMOC (as the forward modeling). The likelihood function ($P(E|\theta)$) minimize this objective function for the optimization during the iteration process. The selected sample sets start to show the stationary condition when the objective function reaches the global minimum. The distribution of selected samples near the global minimum becomes a normal distribution, and we can quantify the uncertainty of our optimized model parameters from the standard deviation values of this normal distribution.

Following the MCMC algorithm, for each experiment in the Rehder et al. (2009) dataset, we select 1,000 appropriate *a posteriori*, as the pair of initial bubble size and the transition time. The ranges of bubble size and transition time span the ranges that bracket the observed values in the measurements for each experiment. Figure 2.9 represents the distributions of the likelihood function for the sampled bivariate data, organized into separate plots for each case. The case numbers correspond to the release depths reported in Table 2.1. This plot shows the value of the probability that the model result is optimal for each pair of values. The bottom and left axes report the variable values; the distributions plotted on upper and right axes shows the integrated probability along each of their normal axes. The maximum point of joint density distribution function for two variables, the initial bubble size and the transition time, is defined as the best model fit for each case.

The model performance compared to the measured data using each combination of initial bubble size and transition time from the MCMC method is shown in Figure 2.10. In Figure 2.10, each dot represents a measured bubble diameter, and each line is TAMOC simulation results based on the MCMC method. The slope of the model curve is set by the rising velocity and mass transfer

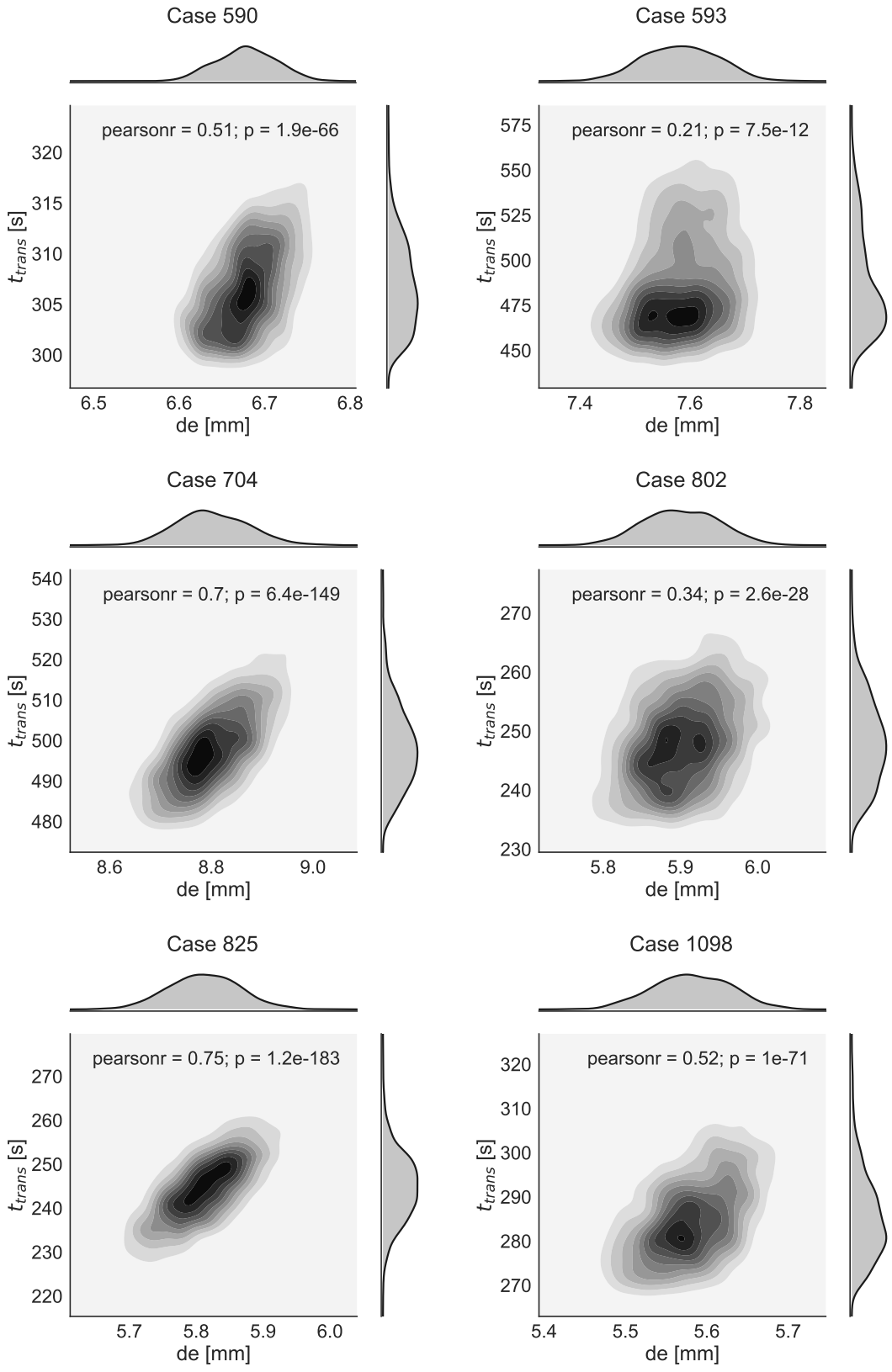

Figure 2.9: Visualization of a bivariate distribution of two variables ($d_{e,i}$ and t_{trans}) sampled by MCMC method.

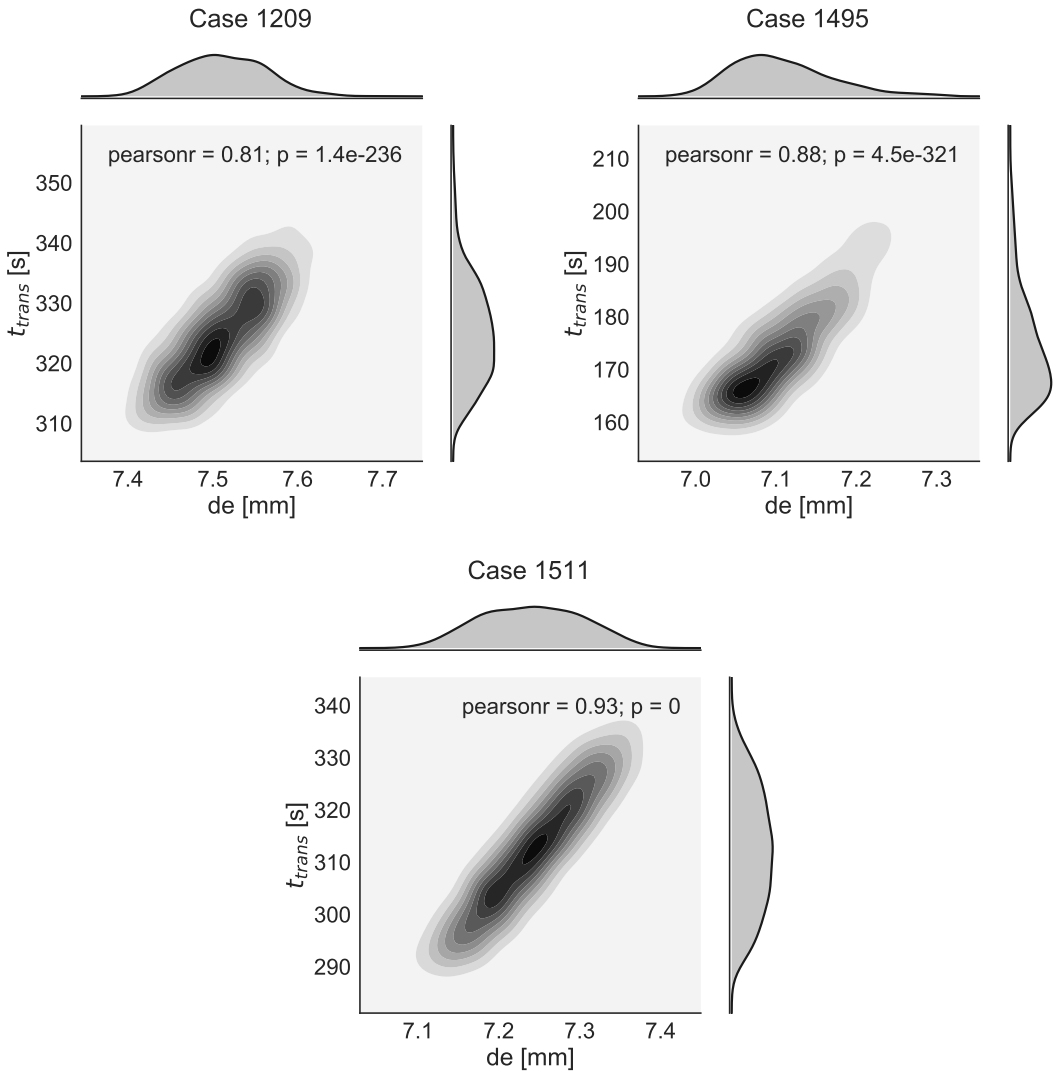

Figure 2.9: Continued

Table 2.2: Summary of estimated de_i and t_{trans} using the MCMC algorithm.

Case	de_i [mm]	ΔT [°C]	t_{trans} [s]
590	6.68	3.70	305
593	7.58	3.87	468
704	8.78	5.64	497
802	5.89	7.46	247
825	5.81	8.24	246
1098	5.58	11.22	281
1209	7.50	12.40	322
1495	7.08	14.38	167
1511	7.25	14.51	312

rate predicted by the DBM equations or the SBM solution; hence, is not part of the calibration. Only the initial point along the model solution (i.e., the initial bubble size) and the point where the solution slope changes from clean bubble mass transfer to dirty bubble mass transfer (i.e., the transition time) are included in the calibration. The model optimal model inputs for each case along with the corresponding sub-cooling temperature is summarized in Table 2.2. Using the data in Table 2.2, we can fit the parameters in Equation 2.8 to obtain

$$t_{trans} = 3.915 A_i \Delta T^{-0.337} = 3.915(\pi d_{e,i}^2)\Delta T^{-0.337} \tag{2.10}$$

t_{trans} depends on the initial surface area and, based on our calibration, can be accelerated by the hydrate sub-cooling.

2.3.3 Statistical Model Evaluation

We perform a statistical evaluation of the model performance using the calibration data. Figure 2.11 shows the comparison between observed and predicted bubble sizes. The comparison shows that $R^2 > 0.9$ for most of the cases, with Case 1495 having $R^2 = 0.73$ and Case 1511 having $R^2 = 0.83$. These two cases have the deepest release depths, and comparing to Figure 2.10 these cases have the greatest scatter in the experimental observations. Indeed, much of the difference between the model and the measurements arises from the inherent measurement error.

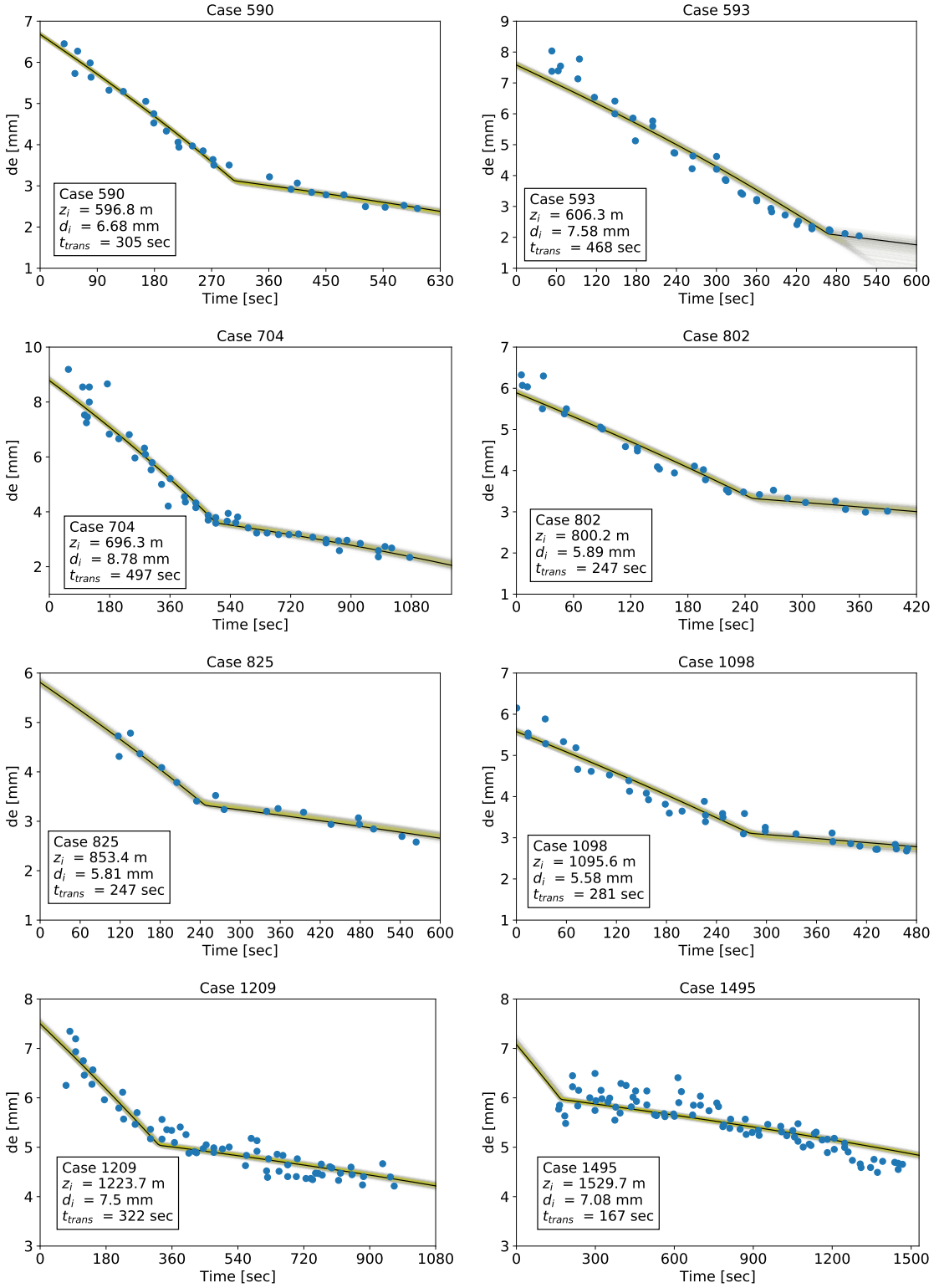

Figure 2.10: Simulation results with MCMC algorithm and best fit model.

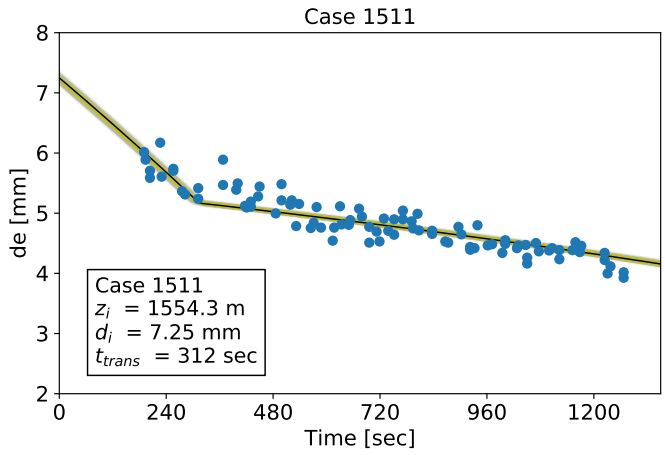

Figure 2.10: Continued

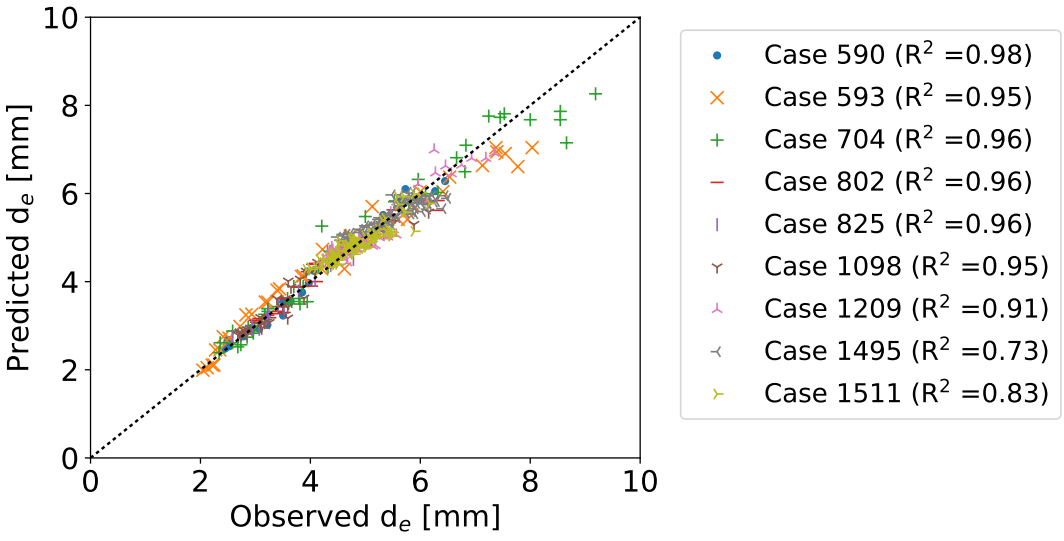

Figure 2.11: The comparison between model prediction with the measurement of bubble size for each case.

Table 2.3: Statistics analysis in model error.

Case	μ_{error} [mm]	σ_{error} [mm]	Bias [%]
590	0.014	0.160	0.437
593	-0.006	0.402	1.982
704	-0.024	0.392	0.282
802	-0.015	0.219	0.141
825	-0.013	0.140	-0.240
1098	0.009	0.227	0.686
1209	0.005	0.227	0.329
1495	0.011	0.261	0.566
1511	0.012	0.201	0.500
Average	0.002	0.264	0.520

As another naïve metric of the model error, we compute the mean (μ), standard deviation (σ), and bias of errors between the model prediction and observed data (Table 2.3). The averaged errors between the model and measurement are 0.002 mm of the diameter, the averaged standard deviation of errors is less than 0.264 mm of diameter, and the averaged bias of errors is 0.52 %. The mean and standard deviation of the errors are similar to the scatter in the measurements observed in Figure 2.10. Likewise, the model bias is negligible over the whole dataset. The model does show a weak tendency to underestimate the bubble diameter for shallow cases (500 m $< z <$ 1,000 m) and overestimate for deep cases ($z >$ 1,000 m). However, within the scatter of the observations, there is no basis to reject the model simulations.

To estimate the magnitude of the experimental error and to obtain a better measure of the model performance, we attempt to quantify the inherent measurement error. We quantify this error using an estimate of the standard deviation of the data based on a two-point moving average. Thus, the true sample standard deviation (σ) may be approximated by the root-mean-square average of the paired data ($\hat{e}$). Hence,

$$\begin{aligned} \sigma &= \sqrt{\frac{1}{N}\Sigma_i^n (y_i - \bar{y})^2} \\ \hat{e} &= \sqrt{\frac{1}{N-1}\Sigma_i^{n-1} \left\{ \frac{(y_{i+1} - y_i)^2}{2} \right\}} \end{aligned} \tag{2.11}$$

For the limiting case of an infinite number of samples, it is possible to show that $\sigma = \hat{e}$. Here, we have limited samples, and this calculation will be approximate. The standard deviation of the entire measured dataset is calculated as 0.398 mm, comparing this to the average standard deviation of error in the model of 0.264 mm. We conclude that the model performs slightly better than the two-point moving average; hence, the model accurately reproduces the trends in the data.

2.4 Model Validation

2.4.1 Validation with Experimental Data

Two independent datasets of direct observation of the transition time for the hydrate skin formation are reported in the literature. These are laboratory experiments of rising methane bubbles in Warzinski et al. (2014) and field observations of seep bubbles rising in the Gulf of Mexico by Wang & Socolofsky (2015), Wang et al. (2016). These datasets allow a direct comparison between the modeled transition time to the observed hydrate formation timescale.

First, Warzinski et al. (2014) observed the hydrate morphology on a 10 mm diameter methane bubble using high-resolution and high-speed imagery. In their experiments, a visible hydrate skin covered the bubble 481 s after the start of injection. Their experiment began with a pressure of 6.59 MPa (corresponding to 650 m ocean depth) which was increased to 10.03 MPa (corresponding to 1,000 m ocean depth) after 236 s at a constant temperature of 8.8 °C. At this condition, their experiment was always within the HSZ of pure methane. We calculate the transition time of that bubble to be 710 s based on Equation (2.10) for the maximum hydrate sub-cooling (5.04 K). The model predicts a longer formation time than observed, but the order of magnitude is well-preserved. The faster transition time in Warzinski et al. (2014) than our prediction may be attributed to the difference of ambient conditions between their experiments (lab tank with non-zero background methane gas concentration) and that for our calibration data (open ocean measurements with negligible background methane gas concentration). We expect that the elevated background concentration in Warzinski et al. (2014) can reduce the nucleation time for hydrate crystal formation compared to that in Rehder et al. (2009). Indeed, for the laboratory experiment, hydrates do not

form on the bubbles until the background concentration becomes saturated with respect to the solubility of the hydrate. At that point, hydrate crystals form in the background water, and these tiny particles nucleate the hydrate process on the bubble/water interface.

The second validation dataset for transition time is for the bubbles at a seep site in Green Canyon lease block 600 (GC 600), observed during a cruise led by the Gulf Integrated Spill Research (GISR) consortium in 2014 (Wang et al. 2016). In GISR, the hydrate formation was observed when the water-particle interface changes from a mobile to a rigid interface, which can be detected in the high-speed videos collected near the seafloor. The high-speed camera system used stereoscopic imaging to obtain accurate measurements of bubble size. The transition time was estimated from the observed bubble mobility at different heights above the seafloor. Because they were also using a calibrated stereo camera system, they could simultaneously measure bubble rising velocities. Bubbles were also collected during the cruise and analyzed for composition. Based on their observations, the hydrate skins were wholly formed between 0.5 m and 20 m of rising above their release to the water column. From the seafloor to 0.5 m altitude, most of the bubbles have a mobile surface, while all bubbles have a rigid interface at 20 m. They also observed many rigid bubbles at about 2 m, but it was difficult to discern the detailed morphology on the bubble-water interface with certainty at that height. Conservatively, we conclude that bubbles were fully hydrated at 20 m. We calculate that the hydrated skin is formed around the bubbles between 2.5 s and 100 s of rising time using an average rising velocity of 20 cm/s observed in the field. In our model, the transition time is calculated as 60 s for the population-median bubble size (D_{50}), 35 s for the lower quartile bubble size (D_{25}), and 105 s for the upper quartile bubble size(D_{75}), which is shown as a box-and-whiskers plot in Figure 2.14(a). From the comparison, the model may overestimate the transition time for large bubbles in the top 25 % of the bubble population density function. One reason this may be the case is that abundant seed crystals for the hydrate formation in the sediment could facilitate rapid formation of hydrate for the leakage of stored CH_4, but our model calculates the formation time from the release point, which is the seafloor.

Lastly, we compare the predicted and observed values for the hydrate transition time (t_{trans}) in

Figure 2.14(a). The coefficient of determination value (R^2) is 0.8 for all cases including Rehder et al. (2009). Hence, these direct validations confirm that our hydrate model is consistent with observations in laboratory experiment data in Warzinski et al. (2014), field experimental data in Rehder et al. (2009), and field observation data for bubbles from the natural seep in Wang et al. (2016).

2.4.2 Validation for CO_2 Droplets

Although our model is calibrated and validated for methane bubbles, we expect the model to be applicable to other hydrate-forming gasses, including hydrocarbon bubbles or droplets. Here, we demonstrate a model application for CO_2 droplets, using the data in Brewer et al. (2002), who measured the rising velocity and dissolution rate of hydrated CO_2 droplets released below the HSL in Monterey Bay, CA. Before performing the simulations, we compare TAMOC predictions with measured data for key thermodynamic properties of CO_2 droplets. Figure 2.12(a) shows the phase diagram of CO_2 and the gray area represents the hydrate region of CO_2. The blue line is the observed temperature-depth profile (T_a) during the experiment in Brewer et al. (2002). The green line (between Q_1 and Q_2) is the model prediction of the equilibrium temperature (T_{eq}), and experimental data from the literature support the model prediction as seen in the figure. In addition, the dashed line is the phase transition between gas and liquid (the boiling curve) of pure CO_2 at its saturation state (http://www.peacesoftware.de/einigewerte/co2_e.html). Here, we get the quadruple point (Q_2) as 10.31 °C and 4.57 MPa by finding the point the intersection for two lines, the boiling curve and the equilibrium temperature line). The result agrees with the theoretical value of the Q_2 of CO_2, 9.85 °C and 4.499 MPa, in Sloan & Koh (2008).

Figure 2.12(b) shows the density of CO_2 calculated using the IUPAC equation of state (IUPAC-EOS) and the Peng-Robinson equation of state (PR-EOS) as implemented in TAMOC compared with the measured data in Brewer et al. (2002). Comparing to the measurements, the MAPE of IUPAC-EOS is 0.312 %, while the MAPE of PR-EOS is 0.663 %. Because the rising velocity of the droplets is very sensitive to the density, we use the IUPAC-EOS for the simulations presented here since it has the lower error, especially at the depth near the release point.

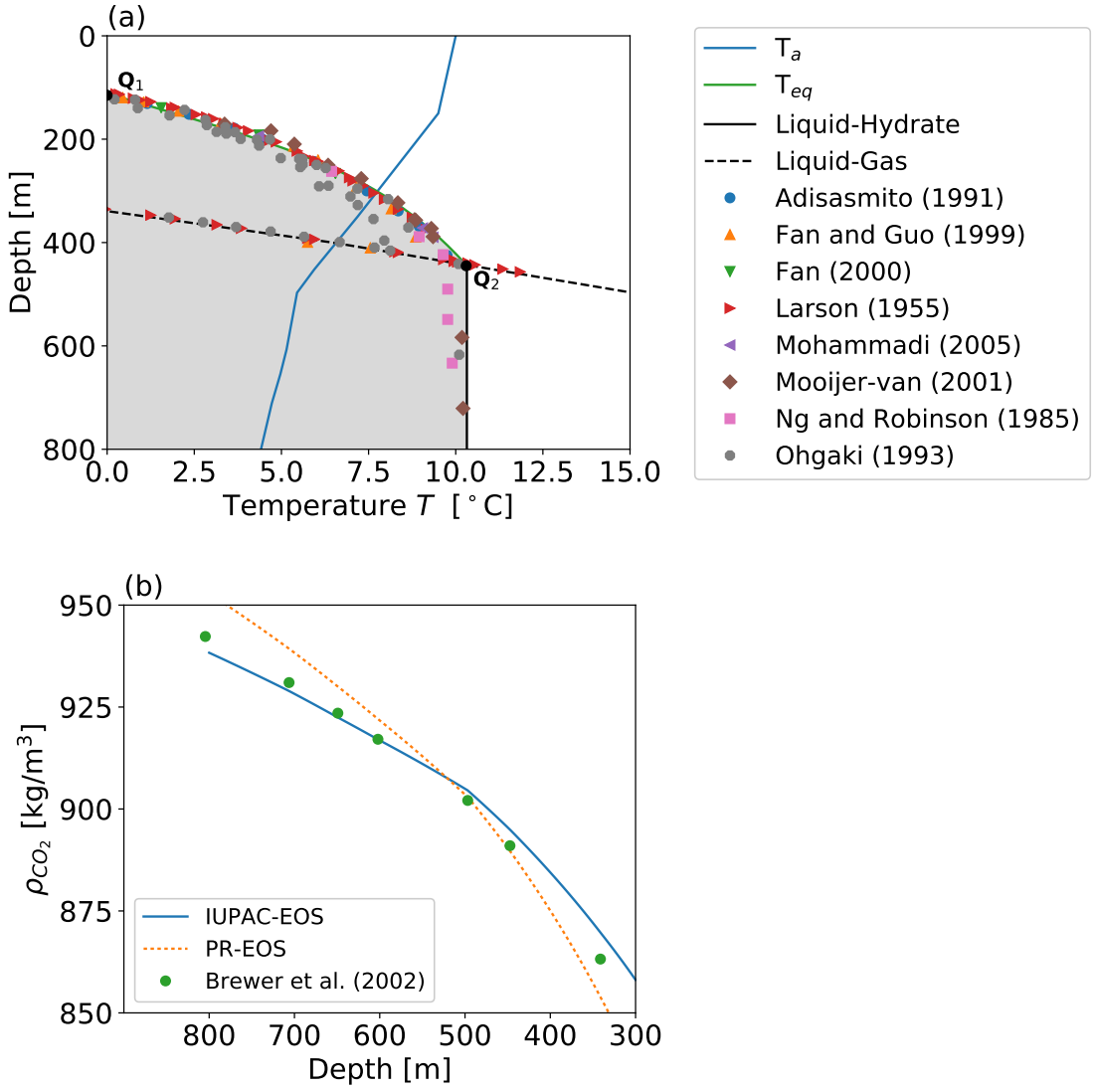

Figure 2.12: Model validation for CO_2 droplet using the experimental data from the literature: (a) the phase diagram of CO_2 and (b) the density of CO_2.

Figure 2.13 shows a comparison between the measured data and the model prediction for bubble size and position for two CO_2 droplets. We initialize the model with dirty droplets (e.g., we assume the droplets begin with a hydrate skin) since Brewer et al. (2002) observed the rigid surface of CO_2 droplet and its spherical shape, which indicate the presence of a hydrate skin, immediately after the injection. Moreover, Brewer et al. (1998, 1999) demonstrated rapid hydrate formation on a vigorous mixing of CO_2 and seawater in their previous experiments. We also imposed a 3 cm/s upwelling velocity resulting from the upward movement of the ROV and containing plexiglass sleeve following values reported in Rehder et al. (2009) for a similar apparatus. With these modeling choices, the TAMOC predictions match well with the experimental data. This also means the CO_2 droplets covered with a hydrate skin seem to behave like a dirty (rigid) fluid particle—consistent with our model hypothesis fo hydrate-coated bubbles and droplets. The model prediction agrees well with the measured data, with an overall MAPE of for 20.96 % and 3.54 % for diameter and depth, respectively.

2.4.3 Comparison with Other Model

Recently, Sun et al. (2017) suggested an alternative model for hydrate-coated bubbles rising in deep water using a different approach. The main difference between our model and that of Sun et al. (2017) is in the assumption of the mechanisms for dissolution. In our approach, the gas or liquid phase inside the bubble or droplet is assumed to dissolve directly into the water, perhaps leaking through crakes or fissures in the hydrate skin; we also assume the mass transfer rate for this dissolution is equivalent to that of dirty bubbles with no other accommodation for the hydrate skin. In the Sun et al. (2017) model, they add a kinetic model for hydrate growth and assume that dissolution into the water phase is happening from the hydrate matrix. That is, hydrate is formed inside of the hydrate shell by water imbibition through the hydrate skin to the gas or liquid phase inside the bubble or droplet, and the hydrate decomposes outside of the hydrate layer into the water by dissolution of hydrate. Thus, the dissolution rate depends on the gas solubility in its hydrated state at the hydrate-water interface. In addition, Sun et al. (2017) uses the initial thermodynamic condition to determine the hydrate nucleation time based on Natarajan

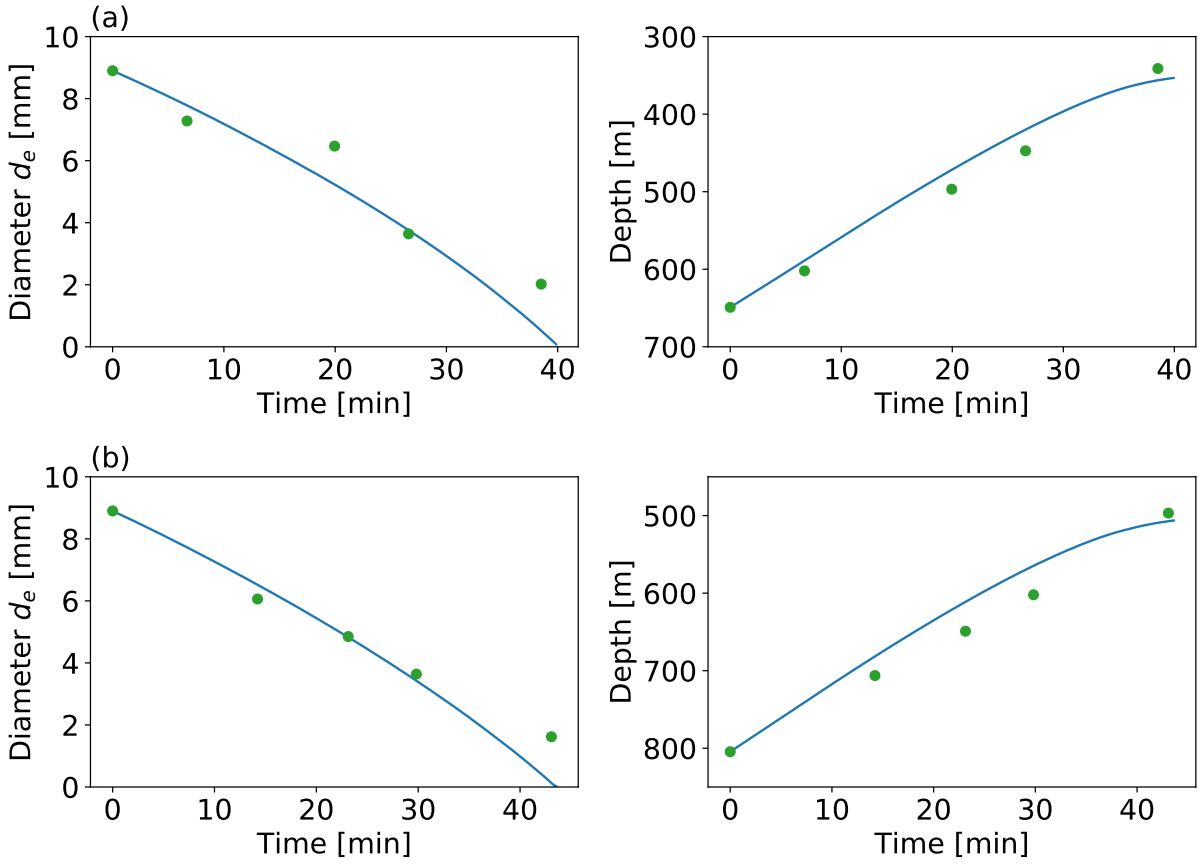

Figure 2.13: Dissolution and transport of CO_2 droplets released at (a) 649.1 m and (b) 804.5 m depth.

et al. (1994) while our model assumes that the hydrate formation time is determined by not only the initial thermodynamic condition but also the initial bubble size. Nevertheless, both models agree that hydrate formation can change the hydrodynamics of the bubble and reduce the dissolution rate since hydrate aggregation alters the bubble surface mobility and, potentially, the solubility at the bubble-water interface.

In the model of Sun et al. (2017), the hydrate nucleation controls the hydrate formation time, and it depends on the initial thermodynamic condition when the bubble is released. The equation for hydrate nucleation time is

$$t_{trans}|_{Sun} = K(f_g/f_{eq} - 1)^{-m} \tag{2.12}$$

where f_g and f_{eq} are the gas fugacity at the initial thermodynamic condition and at the three-phase equilibrium condition, respectively. K is 311.64 in [s] and m is 1.21 for a methane bubble according to Natarajan et al. (1994). The form of this equation implies that the hydrate formation time should only depends on the initial water depth. On the other hand, TAMOC provides a range of transition times for differently-sized bubbles at the same water depth. That is, in Sun et al. (2017) all bubbles of any size released at a given depth have the same hydrate formation time; whereas, in TAMOC bubbles of different sizes have different hydrate formation times even though they are released at the same depth.

Figure 2.14(b) shows a comparison between the model of Sun et al. (2017) and measured data for the transition time. For the deep cases, from 1,000 m to 1,500 m, the model of Sun et al. (2017) can be used. However, the model significantly over-predicts the hydrate formation time for the shallow cases. In Sun et al. (2017), they validated their model only for the bubbles released in deep water (1,098 m, 1,209 m, and 1,511 m). However, as demonstrated by the figure, if we use their equation for shallow cases, then the model does not predict the hydrate transition time accurately. In contrast, the TAMOC model matches the data well over all depths. Because TAMOC includes bubble size where the Sun et al. (2017) model does not, we conclude that initial bubble size is an important parameter affecting the hydrate transition time in the ocean.

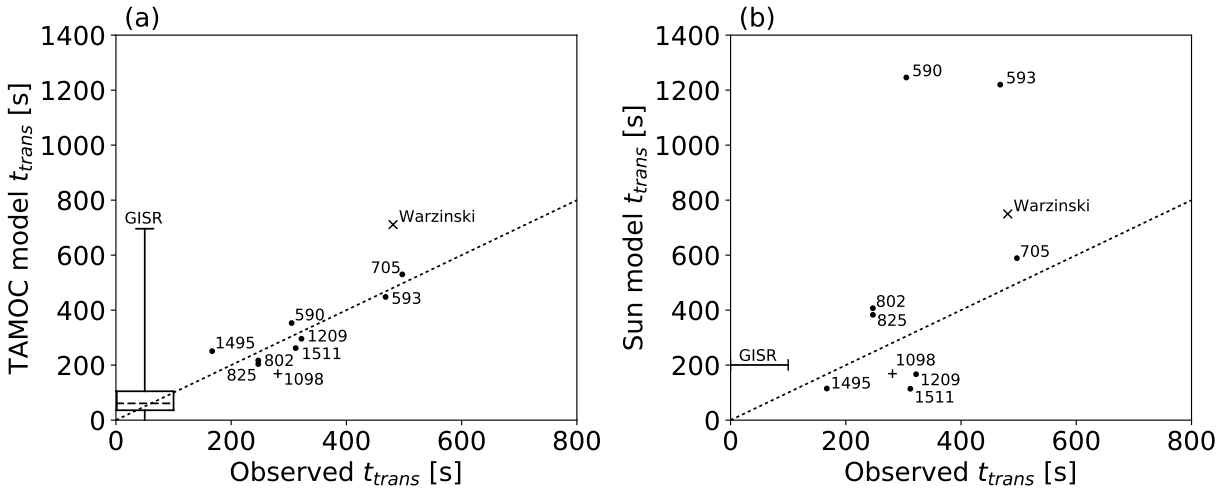

Figure 2.14: Comparison between observed data and the predicted transition time (t_{trans}) by (a) TAMOC and (b) the model of Sun et al. (2017).

2.5 Conclusions

In this section, we have presented a model to predict the fate and transport of fluid particles containing hydrate-forming gasses in deep oceans, below the HSL of these gasses. The model includes non-ideal equations of state for complex chemical mixtures and uses standard empirical correlations for rising velocities and mass transfer rates for clean and dirty fluid particles. Below the HSL, certain gasses form clathrate hydrate shells which affect the mass transfer rates. We hypothesized that the rising velocities and mass transfer rates follow clean bubble equations immediately after release and that they reduce to those for dirty bubbles after formation of a hydrate skin. We further correlate the transition time with the initial bubble size and the degree of hydrate sub-cooling. We apply the MCMC algorithm to identify the transition time due to hydrate formation from the data reported in Rehder et al. (2009).

We validated the model to the available field and laboratory data for methane and carbon dioxide. Some of the validation cases test model predictions of the fluid particle properties (e.g., solubility, dissolution rate, and slip velocity) compared to measured data. In addition, we validate the model with the direct observation of the hydrate transition time using high-speed imagery over a

wide range of hydrate sub-cooling in both the field (Wang et al. 2016) and the laboratory (Warzinski et al. 2014). Lastly, we further validate the mass transfer rates in our model using data for the behavior of rising CO_2 droplets in the deep ocean (Brewer et al. 2002). In each case, the model simulation results could explain both the mass transfer rate and, where observed, the hydrate transition time in the deep ocean environment.

The developed hydrate model–the formation time and the bubble rising velocities and rates of mass transfer–can be used in simulations for other types of hydrocarbon releases, including for subsea accidental oil well blowouts (Gros et al. 2017). For these cases, separate predictive models are available to estimate the initial oil droplet and gas bubble size distributions (Johansen et al. 2003, Zhao et al. 2016, Zheng & Yapa 2000). There is some uncertainty in the role oil coatings and dispersant addition play in altering the hydrate skin formation time. As regards oil, the natural seep at GC 600 released gas bubbles having a significant amount of oil so that the bubbles appeared black in the ROV high definition camera view. In the high-speed camera images, as the hydrate formed, oil streaks on the outside of the hydrate shell were evident. For a subsea accidental blowout in deep water, the oil phase will be a live oil, containing significant dissolved gas so that one may expect hydrate shells to form on both the released bubbles and droplets. Hence, the model here potentially capable of providing accurate predictions of bubble dynamics for both natural seeps and accidental subsea blowouts.

3. PREDICTION OF FLARE HEIGHT OF NATURAL SEEPS

Overview The vertical transport of hydrocarbons through the ocean water column originating from gases escaping from natural subsea seepage is an important part of the biogeochemical cycling of these gasses, including methane. In this study, we compare numerical simulations with field observations for natural gas seep sites in the northern Gulf of Mexico and offshore Pakistan in the Arabian Sea, focusing on the ability of the model to predict the observed acoustic flare heights. We simulate the dynamics of bubbles rising through the water column using the observed data as boundary conditions in the model. We use the single particle model (SPM) in the Texas A&M Oilspill Calculator (TAMOC), which is developed to estimate the fate and transport of gas bubbles released from subsea. Specifically, our model can handle the hydrate effects on rising bubbles from these natural gas seep sites below the Hydrate Stability Zone (HSZ). The physical and chemical parameters of bubbles are potentially affected by the formation of clathrate hydrates on their surface, which immobilize the bubble interface. The new model predicted the evolution of the bubbles originating from 7 seeps observed with source depths of 890 - 2,890 m. We suggested and tested three different methods to compare the model predictions with acoustic observations of the seep bubble flares and discovered that the method using the acoustic target strength of a large bubble is able to predict flare height within $\pm$ 40 m of bias. The simulation results help explain the mass transport of hydrocarbons through the water column and increase our understanding of the fate of hydrocarbons in the oceans.

3.1 Introduction

Acoustic observations show that seep bubble flares tend to rise to the top of the gas Hydrate Stability Zone (HSZ). These large extents of rising are difficult for numerical models to predict. In this paper, we apply our numerical model to simulate bubbles originating at natural seeps and compare the acoustic properties of the model predictions to the *in situ* acoustic observations. This work is important to explain a large amount of existing acoustic data and to validate models for bubble evolution for natural seep flares. Ultimately, these validated models can predict the vertical extent of methane dissolved into the ocean water column above natural seep sites.

In this paper, we use our model, the Texas A&M Oilspill Calculator (TAMOC), to simulate natural seeps within the HSZ. The model is developed for predicting the behaviors of fluid particles released subsea (Dissanayake et al. 2015, 2018, Gros et al. 2016, 2017, Socolofsky et al. 2015) and it includes the dynamics of a bubble for the transport, such as rise velocity and mass transfer rates. The model can handle the impact of the presence of hydrate on the dynamics of bubbles. In the model, bubbles within the HSZ are assumed to dissolve initially at rates equivalent to that for clean bubbles. After the transition time by hydrate skin formation, the mass transfer rates are assumed to reduce to that of dirty bubbles. This transition time depends on the hydrate sub-cooling and the initial bubble size. The model is calibrated using the measured data for pure methane bubbles in Rehder et al. (2009). Our previous work in Section 2 found that the hydrate formation timescales agree with both laboratory experiment and field observation.

Natural gas seeps and gas bubble dynamics in the deep ocean have been observed (MacDonald et al. 2002, Milkov et al. 2000). However, it remains a challenge for the numerical models of bubbles rising from these natural seeps to match the observed significant flare heights for a wide range of observations (McGinnis et al. 2006, Römer et al. 2012, Zhang 2003). These data show the observed gas bubbles rise higher in the deep ocean than the model prediction of natural seep flare heights. Hydrate skin formation on the surface of the bubble is thought to be the main reason for the observed extreme rise height of natural seep flares. Hydrate shells on gas bubbles inhibit the fluid circulation within a bubble and interfere in the mass transfer between bubbles and ambient,

comparable to the effect of a surfactant on the bubble (Clift et al. 1978, Fan & Tsuchiya 1990, Fan et al. 1999).

The water column backscatter data from the multibeam echosounder is becoming a powerful tool to identify natural seeps and the most common type of natural seep observations. Bubbles emit backscatter because they can resonate in the acoustic beam. It is important when comparing models to understand both what the acoustic instrument is capable of hearing and what sound a model predicted flare bubble would emit. In this paper, we combine acoustic models of multibeam excitation of bubbles with a model for bubble evolution with the goal of consistently predicting the observed rise heights of natural seep data.

This section is organized as follows. Section 3.2 describes study sites of natural seepages and the assumptions for the simulations. Section 3.3 describes the hypotheses for predicting the height of natural seeps in the acoustic data. We report simulation results in three different approaches comparing with observed flare heights in Section 3.4. In Section 3.5, we discuss the optimal model for predicting the maximum flare height, and it is followed by the estimation of methane mass flux through the water column with the final model. Lastly, Section 3.6 presents our conclusions.

3.2 Study Sites

To validate the model developed in Section 2, we compare the numerical simulation results with the field observation data for natural seep sites in the ocean. Many natural seeps release bubbles in the oceans below the hydrate stability level (MacDonald et al. 2002, Milkov et al. 2000, Zhang 2003). Here, we selected measurements reported for natural gas seeps in the Gulf of Mexico from Wang et al. (2016) and offshore Pakistan from Römer et al. (2012). We selected these two studies because they include both hydro-acoustic measurements of the seep flares using haul-mounted multibeam and *in situ* observations of the gas flow rates and bubble size distributions at the seafloor using imaging from a remotely operated vehicle (ROV). The *in situ* data is important to provide accurate initial conditions for the model simulations, and these data are generally lacking for studies that report only the hydro-acoustic observations of seep flares.

Table 3.1: The detail information of each of the main seafloor vents investigated during the GISR cruise.

Seep Site	Vent Name	Depth	Latitude	Longitude
MC 118	Woolsey Mound	888.3 m	28° 51.1373' N	88° 29.5338' W
GC 600	Confetti	1185.4 m	27° 22.1954' N	90° 34.2624' W

3.2.1 Gulf of Mexico

A data set of two natural gas seep sites in the Gulf of Mexico exists from the Gulf Integrated Spill Research (GISR) consortium funded by the Gulf of Mexico Research Initiative (GoMRI) (Socolofsky 2015*a*,*b*, Breier 2016). They observed two natural gas seep sites, Mississippi Canyon block 118 (MC 118) and Green Canyon block 600 (GC 600), during two different cruises, the G07 cruise in July 2014 and G08 cruise in April 2015. Figure 3.1 shows the location of MC 118 and GC 600 and the ship track for the GISR G07 cruise. Table 3.1 summarizes the detail information for each natural gas seep site. In the cruise datasets, the seep site at MC 118 was called the Sleeping Dragon based on prior email communication with another research team using that name. The correct, official name for that site is Woolsey Mound, and this is the name we use herein.

These two natural seep sites are in water depths of about 1,000 m well within the HSZ for methane and for the gases emitted at these sites. The GISR research team collected field measurements around natural seeps to characterize the bubble flares and their fate in the water column. They measured the ambient water column conditions, bubble size distribution at the seafloor, the gas composition and gas flux at the emission point, the maximum height of rise of the seep flares in the water column, and the concentration of seep gases within the bubble flare from the seafloor to heights of about 400 m above the seafloor for each natural seep site. The bubble size distribution and gas flow rate were measured using a high-speed stereoscopic camera system (Wang & Socolofsky 2015). From the high-speed imagery, it is possible to confirm the complete immobilization of the bubble-water interface, consistent with the presence of a hydrate shell on the bubble skin.

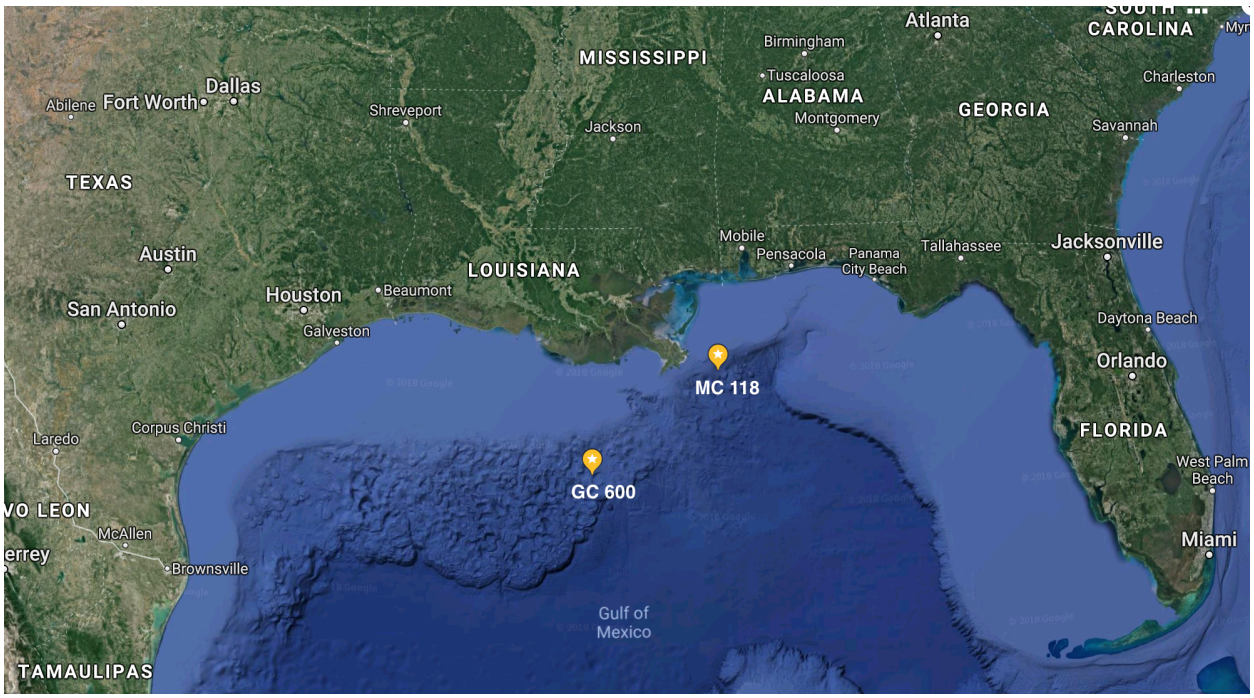

Figure 3.1: The location of Mississippi Canyon block 118 (MC 118) and Green Canyon block 600 (GC 600) in the Gulf of Mexico (Google map, 2018).

3.2.1.1 Ambient Conditions

The ambient water column profiles of measured conductivity (as salinity) and temperature and estimated oxygen, argon, and nitrogen concentration during the GISR cruises are shown in Figure 3.2(a)-(c); measured profiles of salinity, temperature, and oxygen concentration together with estimated profiles of argon and nitrogen concentration for the Römer et al. (2012) dataset are shown in Figure 3.2(d). Figure 3.2(a) is for the MC 118 site from the G08 cruise, and Figure 3.2(b) and (c) are for the MC 118 site and the GC 600 site from the G07 cruise. The temperature and conductivity data were obtained from a SeaBird (Sea-Bird SBE 49 FastCAT) CTD mounted on the frame of the ROV. The ambient dissolved gas profiles (oxygen, nitrogen, and argon) are estimated due to a lack of field measurements. We compute the aqueous solubility of air at the air-water interface, then correct for seawater compressibility and temperature at all water depths. The computed argon and nitrogen profiles are similar to the observed profiles in Pilson (2013), Hamme & R. Emerson (2004), and McGinnis et al. (2006). Biological processes may alter the oxygen profile, and the

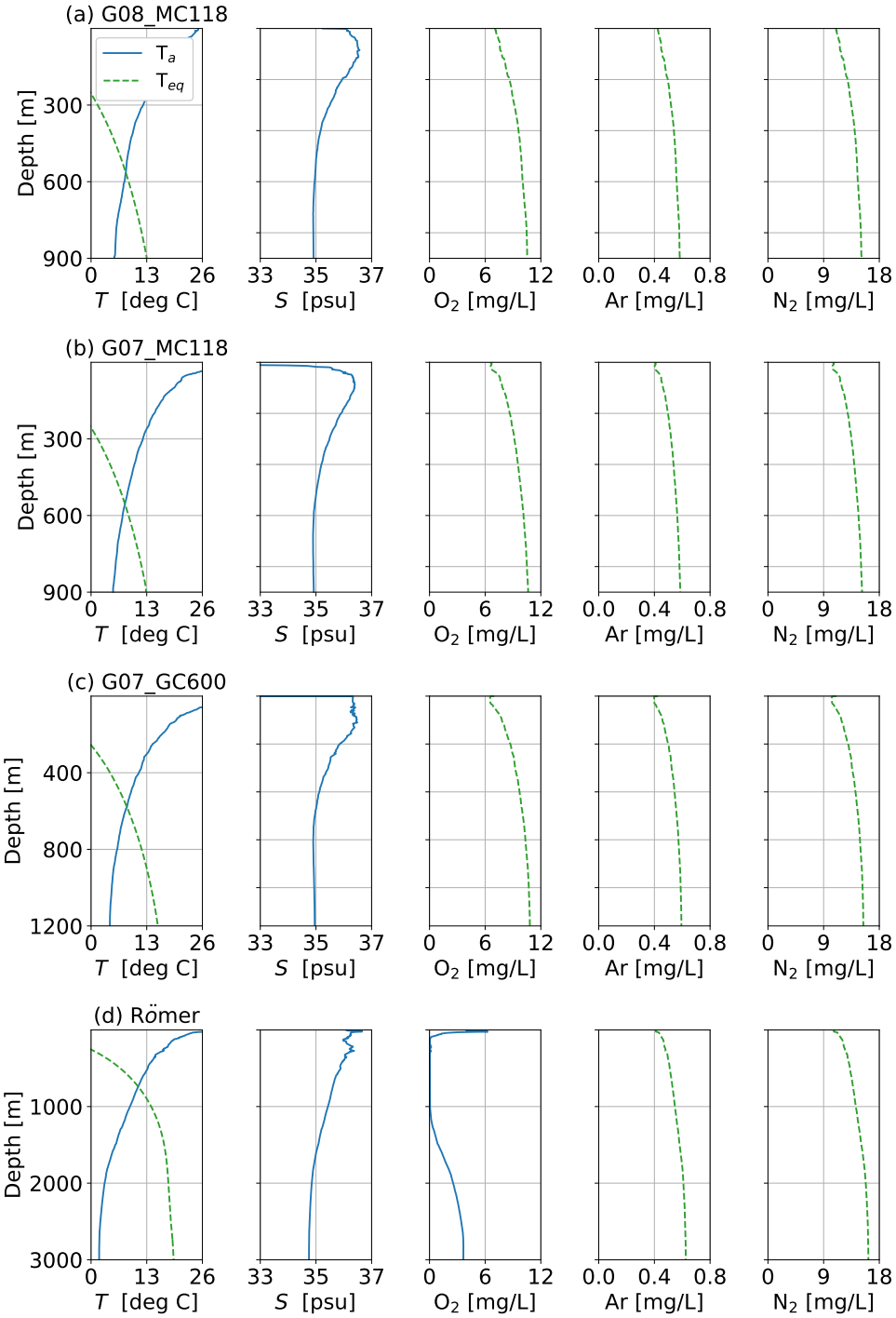

Figure 3.2: Vertical ambient profiles of temperature (T), salinity (S), and dissolved oxygen, argon, and nitrogen (O_2, Ar, N_2) for each site: (a) MC 118 from G08 cruise, (b) MC 118 from G07 cruise, (c) GC 600 from G07 cruise, and (d) offshore Pakistan from Römer et al. (2012). The solid lines indicate measured data, and the dashed lines indicate the calculated value from TAMOC. T_a is the ambient temperature, and T_{eq} is the hydrate stability curve for the gas mixture released at each seep.

estimate computed here is used for lack of any observational data.

For the ambient current data, we use observations for local Acoustic Doppler Current Profilers (ADCP). For the MC 118 site for the G07 cruise, GISR measured the ambient current data during the cruise. For the MC 118 site for the G08 cruise, we use the data from station 42883 from the National Data Buoy Center (NDBC) of the National Oceanic and Atmospheric Administration (NOAA). Station 42883 was the closest station in the database and was located a distance of 2 km from Woolsey Mound seep. The main current oscillations on the Gulf of Mexico continental shelf are inertial, with periods of about 24 hours (DiMarco & Reid 1998); hence, for all numerical simulations, we use 3-hourly averaged currents.

3.2.1.2 Characteristic of Bubbles

During the GISR cruises, researchers measured the size distribution of seep bubbles at the source using a high-speed camera system mounted on the Remotely Operated Vehicle (ROV) (Wang & Socolofsky 2015). Figure 3.3(a) shows the measured bubble size distribution for each cruise at the source point based on the optical measurements together with a fitted log-normal distribution. The probability density function (PDF) of bubble size is reported using the number of bubbles in each size class as the bases for estimating the probability Wang et al. (2016). The fitted PDFs in this figure are used for the initial conditions for the simulations herein.

For the flow rate of each seep on each dive, the high-speed camera system was used to measure the bubble size and bubble rise speed simultaneously. By measuring and counting bubbles as they passed a virtual horizontal team, the flow rate could be estimated (Wang et al. 2016). In addition, gas bubbles were collected from the seeps during the ROV dives, and the gas composition of these bubbles were measured by Gas Chromatography (GC) (Wang et al. 2016). The measured composition of gas at the source is summarized in Table 3.2. The averaged mole fraction of each composition is reported, averaged over all dives. The bubbles contain 68.7 - 87.6 % of methane and some longer-chain hydrocarbons, including ethane and propane. These mixtures are likely similar in nature to the light gas composition that may be emitted during an accidental oil well blowout.

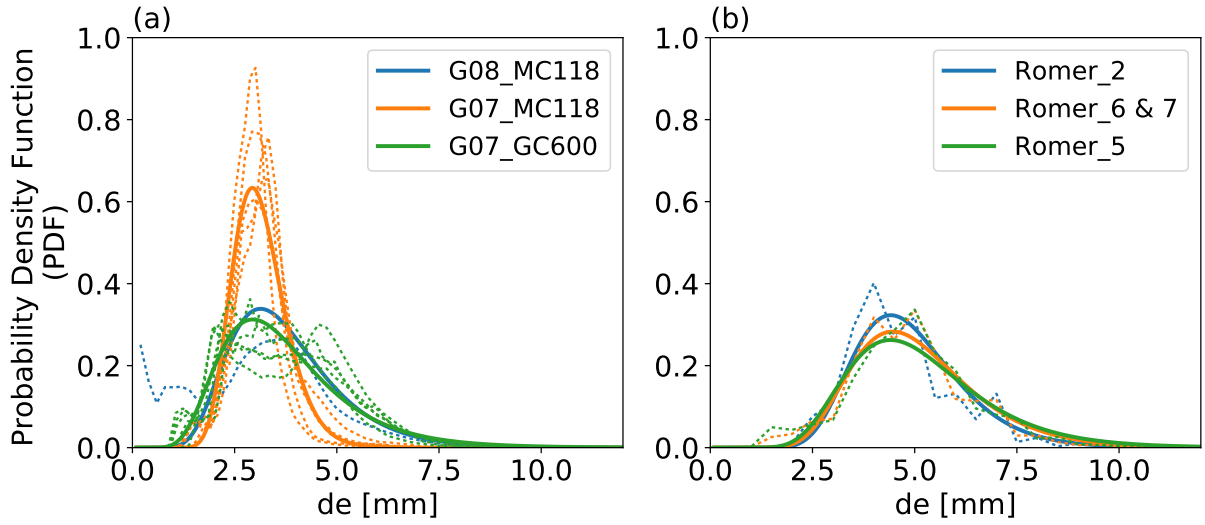

Figure 3.3: Probability density functions (PDF) of bubble size distribution (equivalent diameter) for each seep site: (a) GISR cruise and (b) Römer et al. (2012). The dashed lines represent the measured bubble size distribution from each dive, and the solid lines indicate the fitted log-normal distribution.

Table 3.2: Composition of gas at the MC 118 and GC 600 sites (in mole fraction [%]) from the G07 and G08 cruises

Composition	G08_MC118	G07_MC118	G07_GC600
Nitrogen	19.21	2.68	1.37
Carbon dioxide	1.68	1.96	1.90
Methane	68.73	86.28	87.63
Ethane	2.46	3.35	2.44
Propane	1.48	1.51	1.01
iso-Butane	0.37	0.30	0.14
n-Butane	0.32	0.37	0.35
iso-Pentane	-	0.17	0.09
n-Pentane	-	0.05	0.06

3.2.1.3 Acoustic Investigation

During the GISR cruises, the trajectory of the seep flare in the water column was observed using two different acoustic platforms. Acoustic images of the complete flare trajectory were obtained from the acoustic anomaly in the water column from a ship-mounted Kongsberg EM 302 multibeam echosounder. The sonar frequency of EM 302 is 30 kHz with an angular coverage sector of up to 140 ° and 864 soundings per ping. The achievable swath width on a flat bottom will normally be up to six times the water depth. The data from the EM 302 were post-processed using the Watercolumn module of the Fledermaus software package. In addition to the EM 302, *in situ* observations of the flare cross-sectional view were obtained from the seafloor up to the top of the flare using a Kongsberg Mesotech M3 sonar, mounted on the ROV and oriented in a forward-looking view. The detailed information for the acoustic measurement data is provided in Appendix A and Appendix B of this thesis. All data sets for the GISR cruise are available through the Gulf of Mexico Research Initiative Information and Data Cooperative (GRIIDC) (Socolofsky 2016*a*,*b*).

3.2.2 Pakistan Offshore in the Arabian Sea

Römer et al. (2012) observed submarine hydrocarbon seep sites on the Makran continental margin (offshore Pakistan) in the Arabian Sea. They investigated the water column signature of the seep flares using the ship parametric sediment echosounder system (PARASOUND). The primary sonar frequency of PARASOUND is 18 kHz and the nominal transducer spreading angle is 4 ° resulting in a footprint size up to 7 % of the water depth. The primary frequency of 18 kHz allowed recording of hydroacoustic anomalies in the water column. The single beam parametric echosounder PARASOUND is different from a multibeam echosounder. The single beam echosounder measures the double way transit time of an acoustic signal reflected on the seabed. Water depth under the echo sounder base is computed knowing the sound velocity in water. On the other hand, the multibeam echo-sounder generates the acoustic signal through a wide angular lateral aperture transducer. The reflections of the lateral echoes of the seabed are received from

multiples narrow beams. From the water column acoustic anomaly of the multibeam, they reported the maximum height of rising of the seep flares. Figure 3.2(d) shows the measured CTD profile from Römer et al. (2012). The dissolved oxygen profile is taken from field measurements, and the profiles of dissolved nitrogen and argon were computed using the procedure described for the GISR cruise data, above.

Römer et al. (2012) analyzed the initial bubble size distribution for each flare site by analyzing the HD camera images from the ROV and reported the average molecular composition of hydrocarbons in the bubbles based on analysis of collected gas samples. The bubble at these sites offshore Pakistan consist primarily of methane (over 99.944 %) with a small percentage of ethane, propane, and butane present. The measured gas bubble size distributions are shown with fitted log-normal distributions in Figure 3.3(b).

3.3 Methodology

3.3.1 Numerical Model

The Texas A&M Oilspill Calculator (TAMOC) is used to conduct the simulations. TAMOC is a model developed for predicting the behaviors of fluid particles (droplets and bubbles) released subsea (Dissanayake et al. 2015, 2018, Gros et al. 2016, 2017, Socolofsky et al. 2015). TAMOC contains several general modules (ambient, seawater, chemical properties, and discrete particle module) for supporting the three main models (single particle model, stratified plume model, and bent plume model).

The Discrete Particle Module (DPM) is the module to treat the properties of the fluid particle. DPM handles the chemical properties of several hydrocarbons, the equation of state, and predicts the physical properties of fluid particles, including rising velocity, surface area, heat, and mass transfer coefficients. The Peng-Robinson equation of state with the modified Henry's law is used in the model to estimate the thermodynamic properties of hydrocarbon mixtures, such as density, fugacity, solubility (Gros et al. 2016). Hence, TAMOC can accommodate a complete thermodynamic and physical description of hydrocarbon mixtures.

The Single Particle Model (SPM) can track the trajectory of a bubble or droplet as it rises through the water column. We use SPM to simulate natural seep flares since natural seeps are weak plumes and ambient crossflows strip all entrained water from the flares. In SPM, the transport of a bubble or droplet is modeled by coupling the advection equation for an individual fluid particle to the mass transfer equation for each chemical component in a particle and the heat transfer equation for the whole particle. The trajectory of a particle with time is assumed to be the sum of the slip velocity and the ambient ocean current. This type of particle dynamics may occur for very weak plumes rising from a natural seep in the oceans. The mass transfer equation expresses the dissolution rate of each chemical component, and the mass transfer coefficient is evaluated through correlations from both Clift et al. (1978) and Johnson et al. (1969), as described in Gros et al. (2016). Moreover, SPM can handle the impact of the presence of hydrate on the dynamics of bubbles. In the model, bubbles within the HSZ are assumed to dissolve initially at rates equivalent to that for clean bubbles. After the transition time by hydrate skin formation (t_{trans}), the mass transfer rates are assumed to reduce to that of dirty bubbles. This transition time depends on the degree of hydrate sub-cooling and initial bubble size. The model is calibrated using the measured data for pure methane bubbles in Rehder et al. (2009).

3.3.2 Hypotheses of Modeling

In this paper, we use the observed maximum bubble rise height from the acoustic data and compare this to the predicted rise height from our model simulations of these natural seeps. To make a reliable comparison between the observations and the simulations, we hypothesized three potential mechanics to explain where a natural seep will disappear in the acoustic data. These three hypotheses are:

1. The water column backscatter is the sum of the acoustic target strength within the sample volume of the multibeam, and the bubble will disappear when the integrated target strength falls below the ambient noise or measurement resolution of the multibeam. In this hypothesis, all bubbles exiting the seafloor combine at each measurement height to predict the flare rise height.

2. The bubbles spread out enough that the multibeam will sense the bubble plume as long as one bubble has a target strength large enough to be above the noise level of the instrument. In this case, the largest bubbles exiting the seafloor can be used alone to predict the flare rise height.

3. The flares are will remain observable as long as a certain percentage of the initial gas flow rate is still present in the bubble flare. Like hypothesis 1, all bubbles exiting the seafloor combine to predict the rise height, but it is the bubble mass and not their acoustic backscatter that sets the criterion for being observable.

Each of these hypotheses assumes that some bubbles continue to rise above the observed flare height, and that the flare height observed in multibeam data corresponds to some criteria for which the bubbles become acoustically transparent or at least indistinguishable from background. These hypotheses can be also be understood by considering the acoustic resonance of bubbles in the multibeam path.

3.3.3 Acoustic Target Strength

The acoustic measurement of gas seeps uses the mechanical resonance and acoustic impedance of a bubble (Weber et al. 2014). Each individual bubble has its own target strength (TS), the acoustic backscatter produced by the bubble due to the insolification by the sonar with the specific frequency level. The TS can be expressed as

$$TS = 10 \log_{10} \frac{\sigma}{4\pi} = 10 \log_{10} \frac{a^2}{(f_R/f - 1)^2 + \delta^2} \tag{3.1}$$

where σ is the total scattering cross section of the bubble, a is the radius of a bubble, f is the frequency of insonification, f_R is the resonance frequency of the bubble, and δ is a damping coefficient due to energy loss. The model uses the formulation for f_R and δ in Medwin & Clay (1998), which depends on interfacial tension between bubble-water and density of bubble and seawater. Using Equation (3.1), we calculate the target strength for a bubble for the study sites in both Wang et al. (2016) and Römer et al. (2012). The bubble response for each dataset is different since the

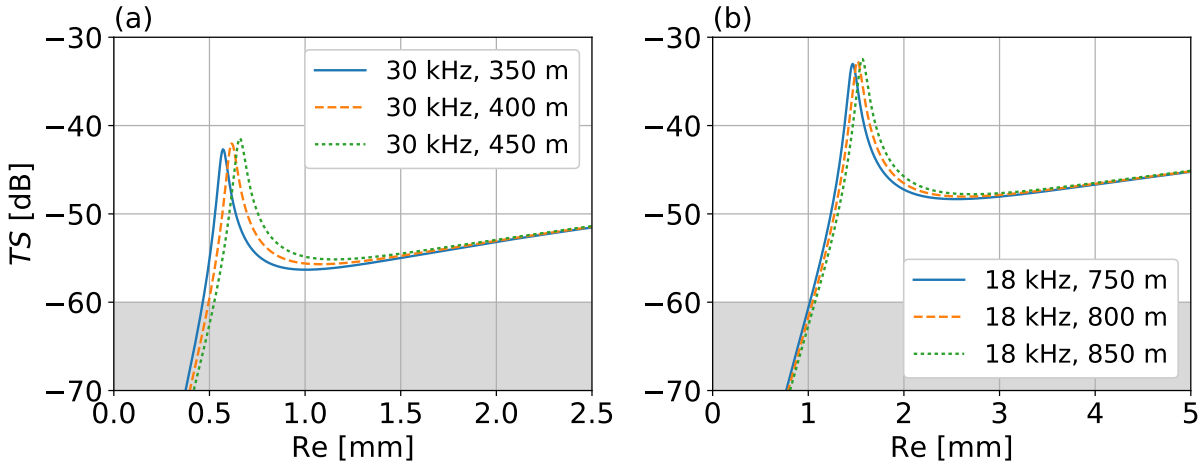

Figure 3.4: Computed acoustic target strength for a methane gas bubble of different radii at the top of the seep for the echosounder in the GISR experiments and those experiments reported in Römer et al. (2012).

GISR cruises used a multibeam with a frequency of 30 kHz; whereas, the Römer et al. (2012) dataset used an acoustic excitation frequency of 18 kHz. Figure 3.4 shows the target strength of a bubble (or backscattering sound level produced by a bubble) with various radii at 30 kHz and 18 kHz. In Figure 3.4, the grey area shows the assumed background noise level of the acoustic data (N.L. < -60 dB). Here, noise arises because of the oceanic ambient noise and as a result of the internal noise of the sensor electronics. We assume that a bubble cannot be observed when its target strength falls below this noise threshold. From the intersection of the TS-curve with the noise threshold, we found for each instrument the critical radius of a visible (detectable) bubble at the top of the flare is 0.5 mm for the GISR cruise data and 1.0 mm for Römer et al. (2012), respectively. Hence, there is evidence that millimeter-scale bubbles may exist in the water column yet not be detected by these acoustic instruments, and the purpose of our working hypotheses is to find the best method to predict where the multibeam will observe the top of the plume.

3.4 Results

In this section, we simulate three cases in from the GISR cruises (G08_MC118, G07_MC118, and G07_GC600) and four cases from Römer et al. (2012) (Romer_2, Romer_5, Romer_6, and

Romer_7). For each simulation, we calculate the flare height using the three different approaches outlined in our hypotheses, above, and compare the results with the observed maximum flare heights in the acoustic observations.

The SPM in TAMOC includes the prediction of the effect of clathrate hydrate skins on the dissolution rate. In the model, we let the dissolution rate and rise velocity of a bubble change from a *clean* bubble to a *dirty* bubble after the hydrate forms on the bubble surface. The transition time (t_{trans}) required for hydrate formation and transition from clean to dirty behavior depends on the initial bubble size and the hydrate sub-cooling, which depends on the released depth. However, for both the G07_MC118 and Romer_Flare5 cases, we run the model with the hydrate formation time being zero ($t_{trans} = 0$). In other words, we run the model for a dirty bubble from the beginning of the simulation, instead of using a clean bubble. For G07_MC118, the bubble size distributions were measured somewhat above the release, and the bubbles were observed as rigid bubbles already at this height; hence, the initial conditions of the measurements were at a point already beyond the transition point. The high-speed stereoscopic imagery confirmed immobilization of the bubble-water interface, consistent with the presence of a hydrate skin on the bubbles. The source of Romer_Flare5 (2,870 m) is much deeper than the model calibration range (500 - 1,500 m, see Section 2). Through our analysis of the available calibration data, we found the hydrate skin formation time could be zero if the degree of hydrate sub-cooling ($\Delta T = T_{eq} - T_a$) is larger than 19 °C. Since the degree of hydrate sub-cooling is about 18 °C in Romer_Flare5, we could consider that the hydrate formed immediately after the bubbles escape from the seafloor—especially given that hydrate nucleation crystals are likely available at the seep release point.

3.4.1 Target Strength of a Flare

Following our first hypothesis, we run the SPM to calculate the TS of the entire flare. To do this, we generate a discrete bubble distribution based on the fitted log-normal distribution and the measured volume flow-rate. We simulate the trajectory and evolution of each of these discretely sampled bubbles, and we calculate the TS for each bubble through the water column. At each computed depth, we compute the total TS of the flare cross-section by summing the contributions

Table 3.3: Representative large bubble sizes ($d97$ - $d99$), volume flow-rate (Q), emission frequency of bubbles (f_b) for each site.

Case	G08_MC118	G07_MC118	G07_GC600	Romer 2	Romer 5	Romer 6 & 7
$d99$ [mm]	8.07	5.00	8.76	8.89	10.49	9.86
$d98$ [mm]	7.33	4.72	7.86	8.26	9.59	9.09
$d97$ [mm]	6.90	4.55	7.33	7.89	9.07	8.62
Q [ml/min]	1,000	100	175	1,588	765	-
Total f_b [no./s]	443	93	73	*260	*229	-

* = Measured bubble emission frequency

from each bubble. This method was applied only to the five cases with known the volume flow-rate (G08_MC118, G07_MC118, G07_GC600, Romer_2, and Romer_5; see Table 3.3).

Figure 3.5 shows the model simulation results using Hypothesis 1. The horizontal lines represent the measured maximum flare height from the echosounders, given by the point where the multibeam no longer distinguishes the bubble flare from the background noise. The solid line is the mean of the maximum flare height (μ) when there are multiple measurements, and the dashed line represents the standard deviation of these measurements ($\pm\sigma$). In most cases, we found that the modeled value of the total TS is about -50 dB at the top of the flares, even though the initial TS values vary for different seeps. Hence, for this hypothesis, we infer that -50 dB is the criterion that should be applied to the modeled total TS to predict the top of these flares.

3.4.2 Target Strength of Single Bubble

Following our second hypothesis, we run the SPM to predict the maximum rise height using characteristic bubble sizes from the measured bubble size distribution and compare the target strength of individual bubbles with the noise level criteria we assumed for these sonar data (refer to Figure 3.4). We simulate three representative large bubble sizes ($d97$, $d98$, and $d99$), which are the intercepts for 97 %, 98 %, and 99 % of the cumulative bubble size distribution; Table 3.3 reports the exact bubble diameter for each case. Figure 3.6 plots the evolution of each of these bubble sizes with height as a means to test Hypothesis 2. The grey area on the right-hand-side of each subplot represents the assumed noise level of the acoustic data (-60 dB), which corresponds

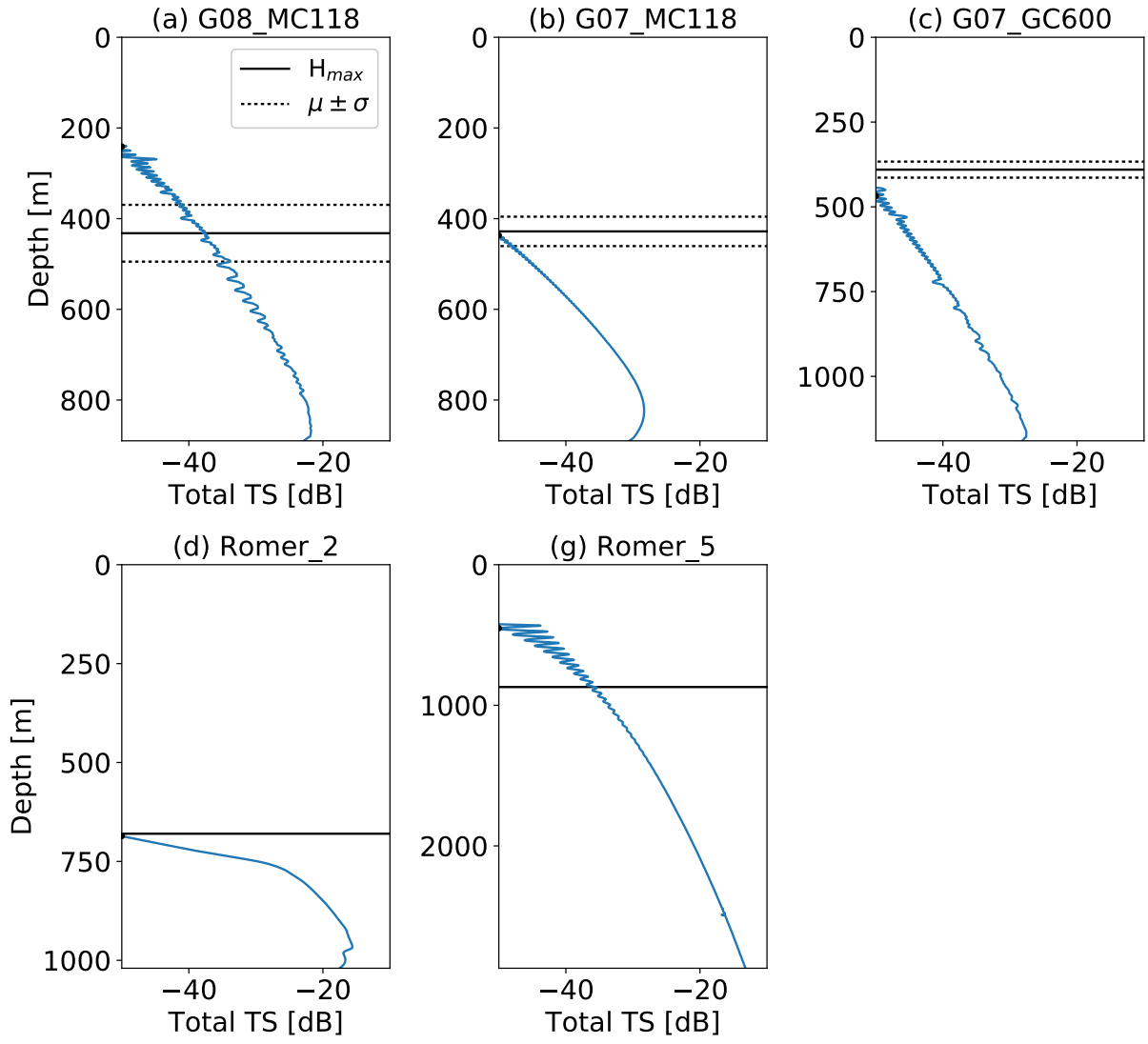

Figure 3.5: Prediction of natural seep flare heights using the total target strength (TS) of all bubbles within the plume for each seep site.

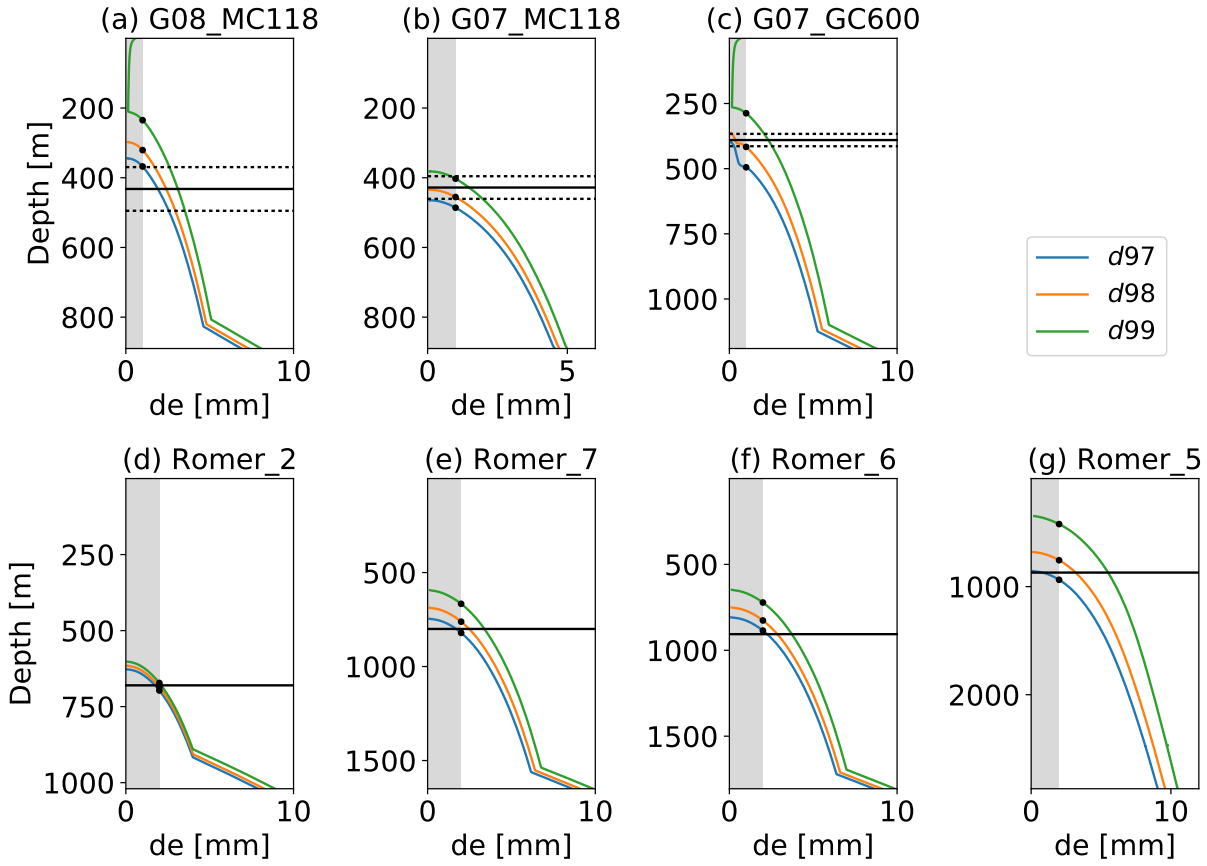

Figure 3.6: Prediction of natural seep flare height using the target strength of the representative large bubbles ($d97$ - $d99$) through the water depth with noise level of acoustic data (gray shaded region).

to 0.5 mm for the GISR cruise data and 1.0 mm for Römer et al. (2012) (refer also to Figure 3.4). Using this method, we find that initial bubble sizes between $d97$ and $d99$ reach the top of the flare at sizes that are visible to acoustic measurements.

To test whether bubbles with this probability are expected to pass within the acoustic sample volume while the ship transits over a seep, we use the measured flow rate to predict the emission frequency of these bubble sizes. Table 3.3 reports the volume flow-rate and the bubble emission frequency for each seep site. Although the flow-rate (Q) varies with each case, these are all weak plumes, with an order of magnitude variation between the highest and lowest flow-rates of order one. In the seeps simulated here, the emission frequency of large bubbles (f_b for $d97$ - $d99$) is between 2.2 and 13.3 bubbles per second depending on the case. Moreover, during the G08 cruise, the cross-sectional view of acoustic data for the measurements 400 m above the seafloor (z = 490 m) has a very weak bubble signal because only a few bubbles were remaining in the vicinity of the top of the flare, which is spread out over a region about 30 m in diameter. These data support our modeling hypothesis which is that the large bubble sizes remaining at the top of the flare may become acoustically transparent at the height where the multibeam observes the top of the flare. Based on these simulations, the criterion for Hypothesis 2 is that the top of the flare is observed where TS of the largest bubbles falls below -60 dB.

3.4.3 Mass Flux of Bubble Flare

Lastly, following our third hypothesis, we calculate the evolution of the mass remaining in a flare through the water column, and Figure 3.7 shows the simulation results using this Hypothesis 3. For these seep flares, we found that the remaining mass at the maximum measured rise height is about 0.1 % of the initial mass flux for all cases. That is, 99.9 % of the total mass flux of a flare has been dissolved into the water column below the detectable maximum flare height. Referring again to Table 3.3, we point out that the flow rates of gas at each of these seep sites are similar, ranging over one order of magnitude. It is possible that seeps with much different flow rates may have different criteria for the amount of dissolved mass below the flare maximum rise height. From the simulations of the present cases, which represent low gas flux rates, we obtain 0.1 % of remaining

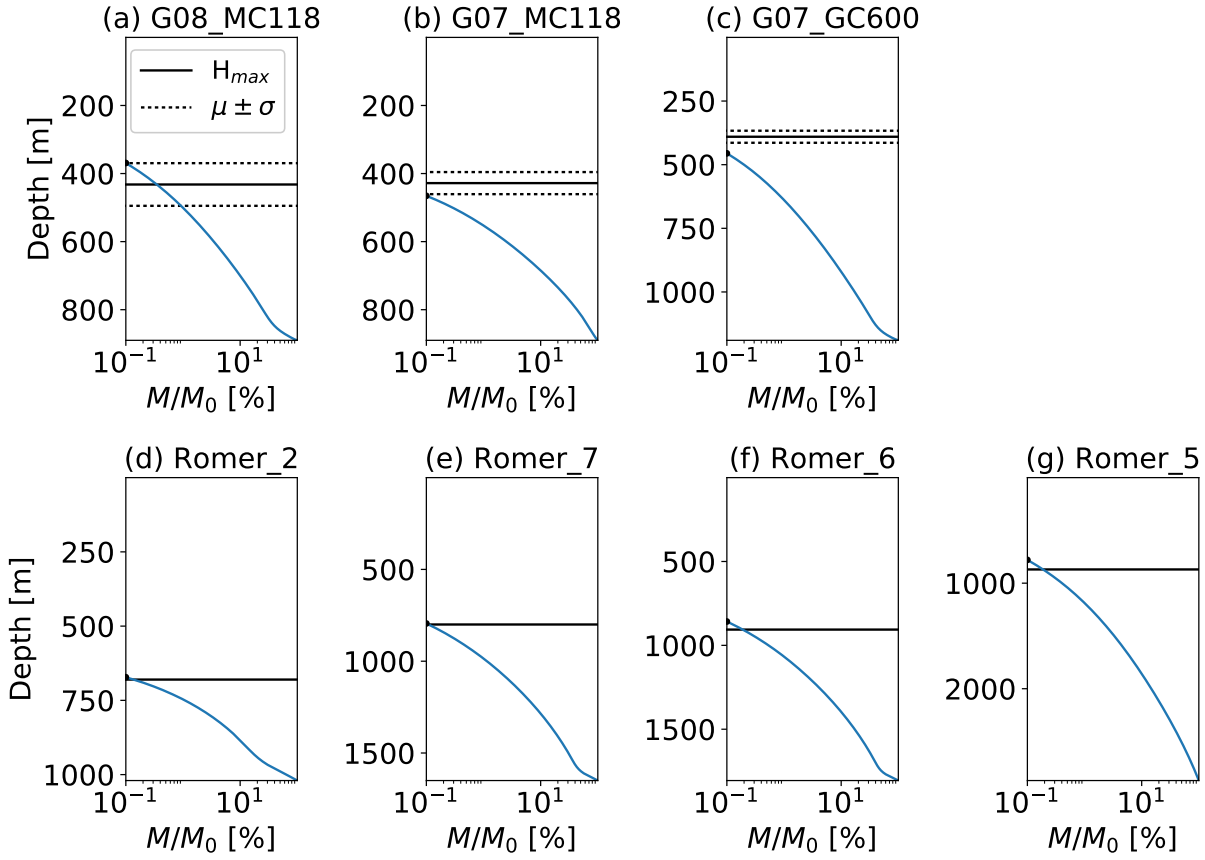

Figure 3.7: Prediction of natural seep flare height using the percentage of remaining initial mass ($\frac{M(z)}{M_0}$) in a flare as a function of water depth.

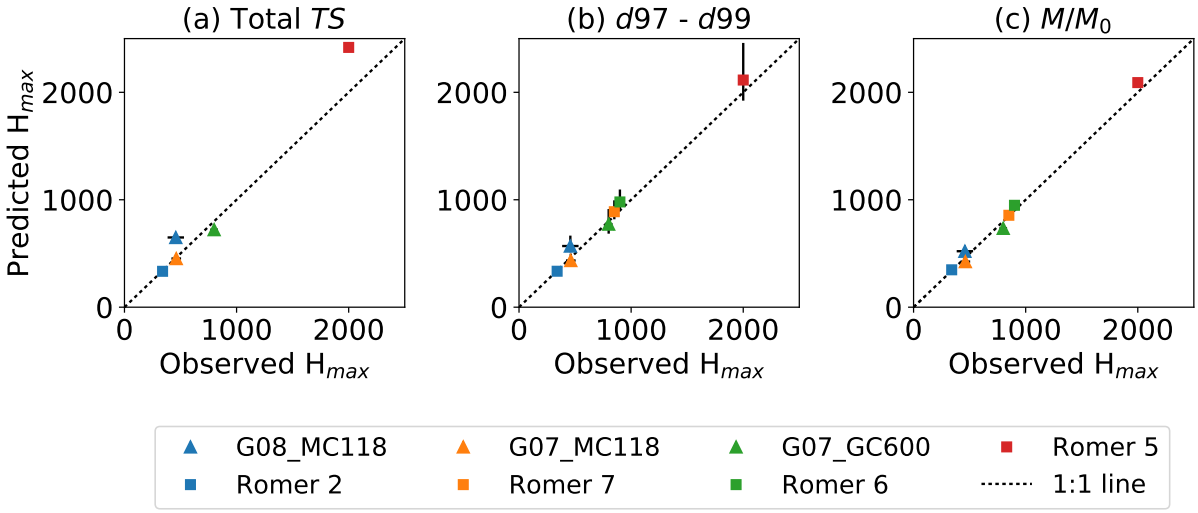

Figure 3.8: Comparison of model performance for the three different approaches to predict the top of a natural seep flare using acoustic data: (a) The total TS (Total TS) of all bubbles, (b) the target strength of the representative single bubble ($d97$ - $d99$), and (c) the ratio of the remaining mass in the flare to the initial release mass (M/M_0).

mass as the criterion to predict the flare height.

3.5 Discussion

3.5.1 Comparison of Model Predictions

To evaluate our hypotheses, we compare the performance of each of these different methods at identifying the height of rising of a natural seep flare. Figure 3.8 shows a comparison between predicted and observed flare height for each of the three different approaches. As derived above, the criterion for the model-predicted top of the flare are: (1) -50 dB for the total TS of the flare; (2) -60 dB for the TS individual large bubbles (in the range $d97$ - $d99$); and (3) 0.1 % remaining of the initial mass flux in the flare. The error bars in the figure show the uncertainty for the predictions and observations. The horizontal error bars describe the standard derivation for the measured height-of-rise data, while the vertical error bars indicate the prediction results for the different bubble sizes (i.e., only Hypothesis 2 yields a predicted height range for bubbles in the range $d97$ - $d99$; the other methods predict a single rise height).

Table 3.4: Summary of the simulation results for the prediction of flare rising height

Case	Observed H_{max}		Predicted H_{max}		
	μ	σ	Total TS	$d98$	M/M_0
G08_MC118	457.83	62.66	649	569	521
G07_MC118	461.88	32.46	453	435	425
G07_GC600	799.72	23.67	722	774	735
Romer_2	340	-	334	335	348
Romer_7	850	-	-	889	856
Romer_6	900	-	-	980	948
Romer_5	2,000	-	2,418	2,114	2,091
R^2			0.93	0.98	0.99
Bias			103 m	41 m	16 m
Ave. PE			9.85 %	4.68 %	1.49 %

We summarize the fit statistics of the data in Figure 3.8 in Table 3.4; the result for Hypothesis 2 is shown for $d98$, only. The R^2 value between the prediction and observation is over 0.9 and the average Percentage Error (PE) is less than 10% for all three methods. The total TS method (Hypothesis 1) gives the least accurate result of the three methods for the maximum flare height (R^2 = 0.93, Bias = 103 m, PE = 9.85 %), although this method is the most realistic prediction because the comparison between total TS and the measured flare height using sonar data is more direct than the other two methods. The disadvantage of this method is that it is only applicable when the flow-rate and bubble size distribution is known since we must evaluate a statistical realization of the total TS for all bubbles in the flare. The single bubble TS method (Hypothesis 2) gives a better prediction compared to Hypothesis 1 (R^2 = 0.98, Bias = 41 m, PE = 4.68 %) with the shortest computing time. Also, this method can be used without knowing the flow-rate information—only an estimate of the bubble size distribution or the diameter of the largest bubbles is required. The method using the mass remaining (Hypothesis 3) gives the best prediction accuracy (R^2 = 0.99, Bias = 16 m, PE = 1.49 %) among the three approaches. Like Hypothesis 1, to compute the mass remaining one requires an estimate of the complete bubble size distribution, but a unit flux can be applied; hence, this method is intermediate among these three methods in terms of the required understanding of the initial conditions.

From the model evaluations in this section, we conclude that all three methods have merit and skill to predict the maximum flare height. For each of use and for application when the gas flow rate is unknown, we recommend using the single bubble TS method, which corresponds to Hypothesis 2. For the single bubble TS method, we assume that the acoustic measurement can detect bubbles when the resonance of the largest single bubble is larger than the ocean ambient noise level, taken here as -60 dB. This assumption relies on the assumption that only one large bubble is needed at the top of the flare to be observable and that the flare spreading is enough so that the sonar may only sense a single bubble in each ping and interrogation window. The main advantage of this method is the good prediction accuracy, with the acceptable error for the seeps analyzed here of 4.68 % and 41 m, respectively for $d98$.

When the bubble size distribution is unknown, one would have to assume a distribution. Figure 3.3 shows that the PDFs of bubble size vary from site to site and from day to day at a given site. Likewise, as reported in Table 3.3, bubble sizes for $d98$ vary from 4.72 mm to 9.59 mm among the seeps evaluated here. Hence, while large bubbles are often of the order of 10 mm in diameter, individual seeps can show wide variability, and a measurement of the bubble size would be needed to obtain reliable estimates from any of these methods.

3.5.2 Optimal Model Prediction of Flare Height with Hydrate Effect

The success of our modeling approach in each of the hypotheses tested above relies on our model's validated approach for handling the effect of hydrate skins. To demonstrate the need for this element of the simulation approach, we show results for $d98$ using the method from Hypothesis 2. According to the comparison the simulation results with the measured data, we selected the optimal model for predicting the flare height, using the representing single bubble simulation for $d98$. Moreover, the advantage of our model is its ability to include hydrate effect on the dissolution of a bubble, which means surface contamination from a clean bubble up to a fully contaminated bubble. The model can deal with the change of dissolution rate due to the hydrate formation on the bubble surface, and the model can simulate different types of dissolution rates for a *clean* bubble, a *dirty* bubble, and a *transition* bubble by the hydrate skin formation. In the literature for natural

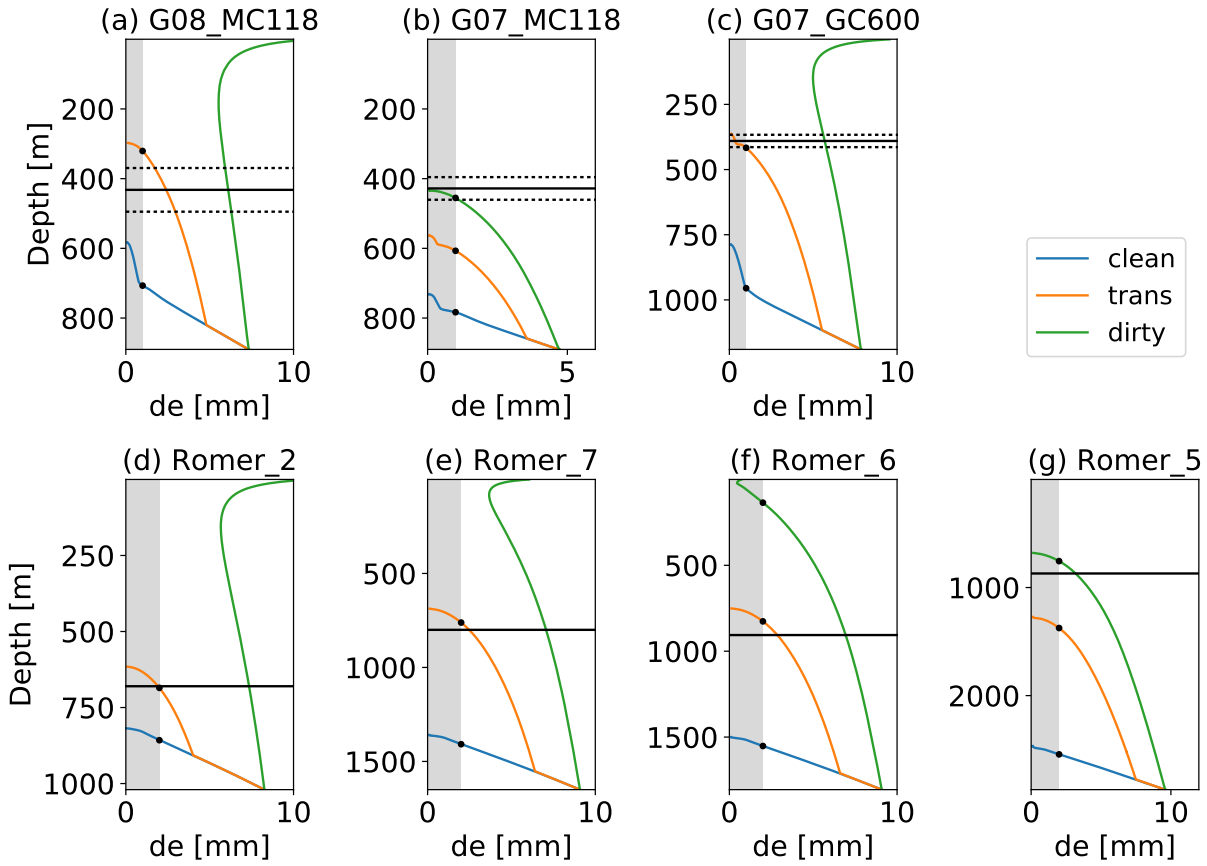

Figure 3.9: Optimal model prediction of the maximum flare height with three different mass transfer models: clean bubbles, dirty bubbles, and the transition timescale from clean to dirty used in TAMOC.

seeps, most models apply a clean bubble mass transfer rate without hydrate shells and various approaches to reducing the mass transfer rate after formation of the hydrate. On the other hand, most models in the literature for bubbles would predict that dirty bubble mass transfer rates should govern the bubble dynamics from the outset due to the presence of naturally occurring surfactants in the ocean water. Here, we apply our model using 1.) the optimal case of clean mass transfer rates transitioning to dirty rates after the hydrate transition time, 2.) clean mass transfer rates throughout the simulation, and 3.) dirty mass transfer rates throughout the simulation.

Fig 3.9 shows the the model results in each of these cases. The three lines in each figure give the fate for a bubble that has clean-bubble mass transfer rate (blue), dirty bubble mass transfer (green),

and our model that uses a transition time to switch from clean to dirty mass transfer (orange). If we assume a clean bubble for the simulation, then the dissolution rate is fast due to the internal convection that occurs in bubbles with a slipping bubble/water interface Clift et al. (1978). Using the clean bubble, the predicted bubble rise height is much lower than the observation. By contrast, if we use a dirty bubble dissolution rate, the bubble rises higher than the observed flare height because of the slow dissolution rate caused by the lack of internal convection within the bubble (Clift et al. 1978). These bubbles can reach the water surface for most cases. The model can predict an accurate flare height only when we consider the transition of dissolution rate by the hydrate formation in the simulation. This figure confirms that the mixed model with a transition time is the only approach that has a capability to predict each measurement in the GISR and Römer datasets using our SPM and our models of the acoustic behavior of these bubbles in the echosounder observations.

3.5.3 Estimation of Methane Flux from Seep to Ocean

Our main interest in predicting the methane dissolution in the water column is to predict the vertical distribution of dissolved methane, a key component of the global biogeochemical cycling of methane. Generally, methane is also of interest through its potential contribution to atmospheric methane since methane is a potent greenhouse gas (Judd et al. 2002, Judd 2004); however, it is becoming well recognized that little methane reaches the atmosphere from natural seeps in the ocean (Ruppel & Kessler 2017). To evaluate the vertical distribution of methane in the water column, we analyze the model predictions to compute the methane flux as a function of height. Figure 3.10 shows the mass flux of methane for all simulated seeps. The result shows that continuous gas exchange and gas stripping through the water column keeps most of the methane gas sequestered at depth instead of releasing into the atmosphere. Methane starts to dissolve relatively fast from the beginning, and most of the methane has been dissolved in the first 400 m of rising. From our simulations, at the acoustically detectable flare height, 99.9 % of methane has been dissolved into the water column.

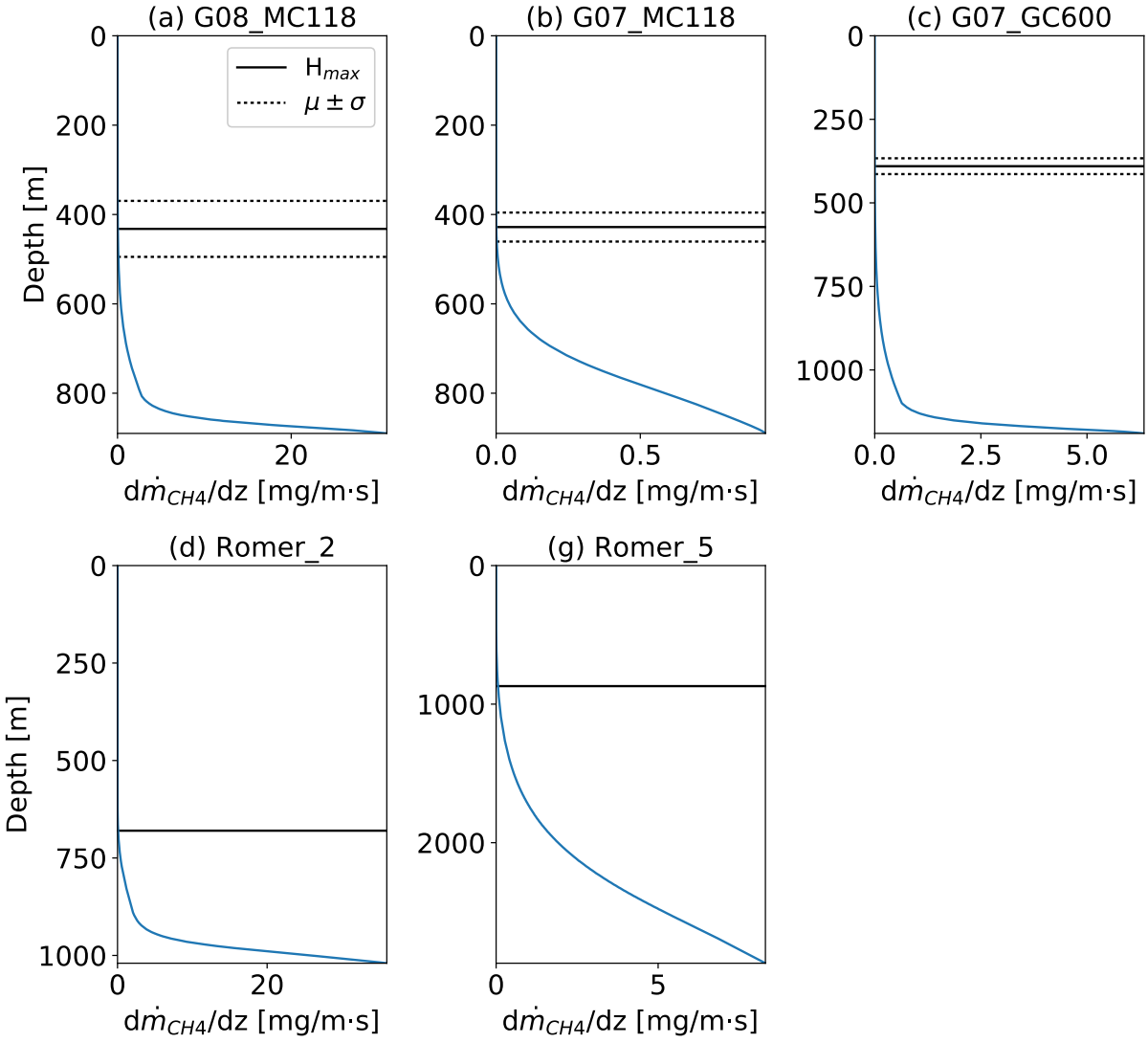

Figure 3.10: Estimation of dissolution of methane gas from bubbles to ocean.

3.6 Conclusions

This study provides model simulations for hydrocarbon bubbles in the ocean environment to study different natural seep sites with diverse conditions. The model in this section particularly dealt with predicting the maximum flare height observed by haul-mounted echosounds on oceanographic research vessels. We proposed three different methods to predict the maximum flare height, each method based on different criteria for the height at which a seep flare will become acoustically transparent in the simulation data, and we found that all of these methods work well compared with the field observations. The simulation result of the single bubble method shows that only large bubbles (in the range of $d97$ - $d99$) were visible to the acoustic measurements at the measured flare height. Thus, we recommend using the single bubble simulations for these large bubbles to predict the maximum flare height of natural seeps.

The application of the model improves the capability of bubble prediction models as well as increases our understanding of the mechanisms controlling the fate and transport of hydrocarbons released into the ocean environment. Since the rise heights of these plumes are matched well by the model, we assume the model also estimates the proper mass flux of hydrocarbon gases from the natural seeps in the ocean when we consider the change of dissolution rate by the hydrate formed on the bubble surface. The model with hydrate effects also can explain the impressive rise height of flares observed from natural seeps in the deep ocean.

Moreover, we use the model to estimate the vertical distribution of methane from these natural seeps to the ocean water column. The simulation result shows that methane is dissolved into the water column very fast and that most mass remains in the ocean, below the upper mixed layer (400 m depth); hence, it is not released to the atmosphere. This study is important to understand biogeochemical cycling of natural gases released from the natural seep and to confirm the hypothesis that natural seeps make a negligible contribution to the atmospheric greenhouse gas budget.

4. MODELING THE FATE OF HYDROCARBONS FROM NATURAL SEEPS

Overview In this study, we use the single bubble model in the Texas A&M Oil spill Calculator (TAMOC) to model the dissolved concentration field near bubbles from natural seeps. The bubble model in TAMOC can track the Lagrangian transport and coupled fate by dissolution of bubbles as they rise through the water column by solving the advection equation coupled with the mass transfer equation for chemical components in a bubble. This model also considers the presence of a hydrate skin on the dynamics of bubbles so that it is applicable to bubbles rising within the hydrate stability zone. Moreover, the bubble model can simulate bubbles from natural seeps since natural seeps are weak plumes and ambient crossflows strip all entrained water from the flares. To compute water column concentration, we treat each bubble as an infinite line source, and we apply superposition over all bubbles to an analytical solution of the advective diffusion equation. For model validation, we compare the modeled concentration fields to *in situ* measurements from two cruises to Mississippi Canyon lease block 118. The measured data include water column samples obtained by ROV. Based on the acoustic measurements (EM 302 and M3), we confirm our numerical model of transport of rising bubbles from the natural seep in both horizontal and vertical directions. The model for the dissolved gas phase is also verified using the *in situ* water samples for dissolved methane gas around the natural seep. The result shows that the main axis of the dissolved concentration distribution can be different from the long axis of the bubbles spreading in the plume. This explains why the maximum measured concentration is sometimes located at the edge of bubble distribution in the measurements and provides the need to revise sampling plans for the future field campaigns.

4.1 Introduction

After the methane are dissolved into water, biological degradation of methane mostly occurs in the dissolved phase (Richard et al. 2010, Valentine 2002). It is important to know how far and how much the dissolved methane will be distributed through the water column to understand biogeochemical pathways of methane in the ocean water column. The dissolved methane will spread out according to the ambient current and their diffusivity. In this paper, we present the results of a Lagrangian model for bubble fate coupled to an analytical solution for water column concentration to predict the dissolved methane concentration near a natural seep flare. The model is validated by comparison to *in situ* measurements obtained during to cruises to a natural seep on the continental slope of the Gulf of Mexico. This work is important to relate the mass flux of dissolving methane from natural seep bubbles to realistic water column concentration predictions.

The problem of converting Lagrangian particle concentration to water column concentration is a common problem in Lagrangian particle tracking models. Usually, the Lagrangian particles themselves represent dissolve mass, and the Lagrangian particle tracking approach is used to avoid excessive numerical dissipation for Eulerian transport solution in numerical models with coarse resolution relative to the size of the concentration distribution. Here, the Lagrangian particles represent individual dissolving bubbles, and the concentration in the water column results from the mass flux of methane from the bubble into the dissolved phase. While the single particle model predicts the dissolving mass flux as a function of height, it does not predict the resulting concentration in the water column. To bridge this gap, we will apply an analytical solution to the advection-diffusion equation subject to the source boundary conditions from each bubble.

This section is organized as follows. Section 4.2 explains the methodology for modeling the transport of bubbles from a natural seep. We upgrade the Texas A&M Oil spill Calculator to account for the bubble spreading by turbulent and the concentration distribution of dissolved gas. Section 4.3 describes data for a natural seepage in the Gulf of Mexico from GISR cruises. In Section 4.4, we report simulation results for the transport of bubbles and the concentration distribution and compare with the observed data. Lastly, Section 4.5 presents our conclusions.

4.2 Methodology

4.2.1 Random Walk Model for Bubble Spreading

The Single Particle Model (SPM) in TAMOC solves for the time-average trajectory of a single bubble, droplet, or particle in the ocean water column subject to a steady ambient current and set of temperature, salinity, and concentration profiles. To use this model to predict the behavior of a swarm of bubbles emitted from a natural seep, we should simulate many bubbles and account for their wandering paths due to ambient turbulent diffusion.

To do this, we apply the random walk method to simulate the horizontal migration of bubbles in the plume. For a Fickian diffusion process, the width of a concentration distribution σ is given by

$$\frac{d\sigma^2}{dt} = 2D \tag{4.1}$$

where D is the effective diffusion coefficient, which we take here as a uniform turbulent diffusivity. In the classical Euler's solution to the random-walk problem, Equation (4.1) is used to obtain the following update equation for particle position in one dimension

$$x_{i+1} = x_i + \xi\sqrt{2D\Delta t} \tag{4.2}$$

where the subscripts represent the present position x_i and the future position x_{i+1} and ξ is a random number generated from a normal (Gaussian) distribution. The SPM in TAMOC solves the advection equation using a high-order numerical method. We can write the random displacement due to diffusion as a random velocity by dividing Equation (4.2) by Δt, giving the following advection equation in differential form

$$\frac{d\vec{x}}{dt} = \vec{u}(t) + \xi\sqrt{\frac{2D}{\Delta t}} \tag{4.3}$$

where $\vec{x}$ is the three-dimensional vector position of the bubble, $\vec{u}(t)$ is the vector velocity of the bubble, which is a combination of the ambient current and the slip velocity of the bubbles in the vertical direction ($\vec{u} = \vec{u}_a + u_s\vec{k}$), as a function of time, D is the horizontal diffusion coefficients

(in the x- and y-direction) by turbulent diffusivity, and Δt is the time step size of the numerical calculation. We solve Equation (4.3) using the classic fourth-order Runge-Kutta method. The diffusion coefficient of the bubbles were measured for the field-scale plumes by the Gulf Integrated Spill Research (GISR) Consortium during GISR cruise G07 to Mississippi Canyon lease block 118, and the average value they obtained was 3×10^{-4} m^2/s.

4.2.2 Fate Model of Natural Seep Bubbles

The SPM couples the random-walk Equation (4.3) to the mass transfer equation for dissolution from each bubble. The composition of a given bubble is given by the mass m_i of each chemical component i in the bubble, and we apply the mass transfer equation

$$\frac{dm_i}{dt} = -A\beta_i(C_{s,i} - C_{a,i}) \tag{4.4}$$

where A is the surface area of the bubble, β_i is the mass transfer coefficient, $C_{s,i}$ is the solubility of component i at the bubble-water interface and $C_{a,i}$ is the ambient concentration of component i far away from the bubble. As described in Section 2, we apply clean bubble mass transfer coefficients initially after the bubble is released. After a transition time t_{trans} that depends on the initial bubble size and the hydrate sub-cooling, we switch the mass transfer rates to those of dirty bubbles to represent the effect of a hydrate skin on the bubble/water interface. The transition time was calibrated to measured data by Rehder et al. (2009) and validate to both laboratory and *in situ* measurements as reported in Section 2. We further validated this model by comparing model predictions for the bubble target strength in an acoustic field to the height of rise observed in haul-mounted echosounder data in Section 3. Together with Equation (4.3) this mass transfer model predicts the fate and transport of individual seep bubbles in the ocean water column.

4.2.3 Model of Dissolved Gas from Seeps

Equation (4.4) yields a solution for the rate of mass loss dm_i/dt from each bubble into the ocean water column due to dissolution as a function of time (which also relates to the height above the seafloor). To convert this result to dissolved concentration in the ocean water column, we apply

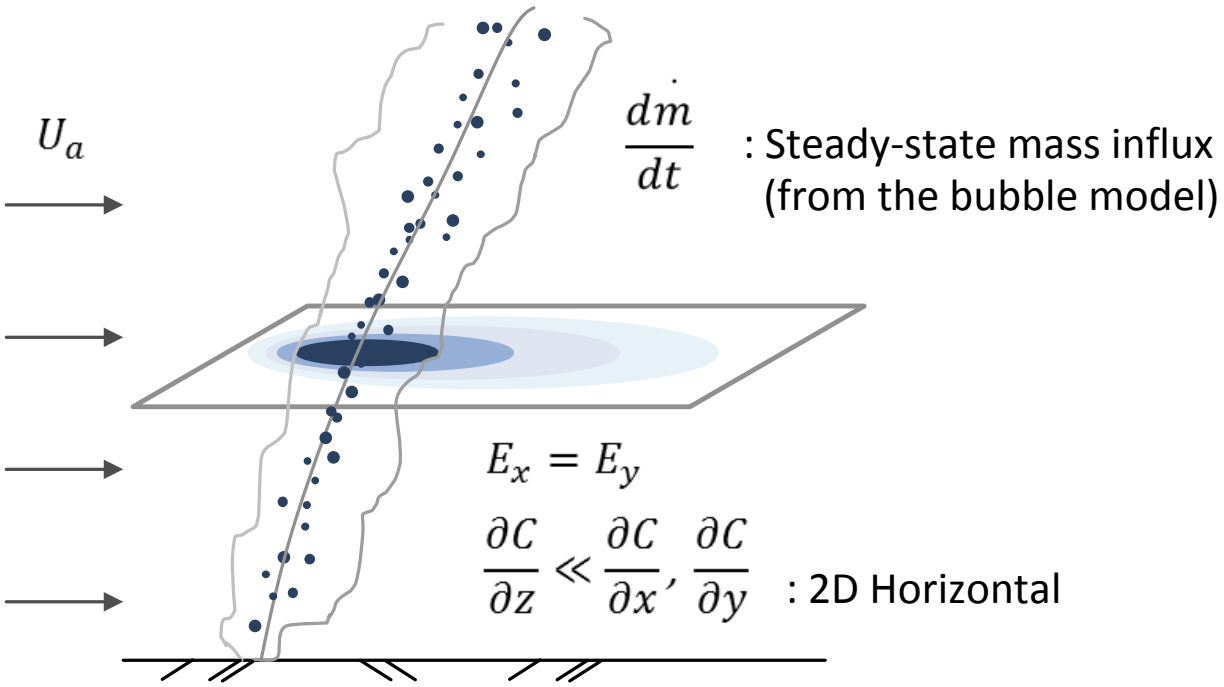

Figure 4.1: Schematic diagram of the model of dissolved gas from seeps

an analytical solution to the advective-diffusion equation. We obtain this analytical solution by assuming that locally at any given height, the mass flux dm_i/dt from the bubbles can be represented by an infinite, uniform line source, and we obtain a solution for all bubble by superposition of the solutions for each individual bubble. Figure 4.1 shows the schematic diagram of the model.

The steady state advective-diffusion equation for homogeneous, constant isotropic horizontal diffusion ($E_x = E_y = E$), negligible vertical diffusion ($E_z << E_x, E_y$) with the steady velocity field $\vec{u} = (U, 0, 0)$ is given by

$$U\frac{\partial C}{\partial x} = E\left(\frac{\partial^2 C}{\partial x^2} + \frac{\partial^2 C}{\partial y^2}\right) \tag{4.5}$$

where C is the concentration of dissolved gas. In this model, we neglect the influence of biodegradation on the dissolved hydrocarbons since the model focuses on the near-field concentration distribution of methane around the natural gas seep site, confined to a few 100 m from the seep flare, which represents a few minutes of transport by the ambient currents. By comparison, the half-life of methane biodegradation is of order one day.

The exact solution of Equation 4.5 for an infinite, continuous, and uniform line source injection along the z-axis is given by

$$C(x,y) = \frac{\dot{m}}{2\pi E} \exp\left(\frac{Ux}{2E}\right) K_0\left(\frac{Ur}{2E}\right) \tag{4.6}$$

where $\dot{m} = (1/u_s)dm_i/dt$ is the mass flow rate from the source per unit length along the z-axis, K_0 is the modified Bessel function of the second kind of order zero, and r is the distance from the source. In the model, we take E as a value between the molecular diffusion coefficient and the turbulent diffusion coefficient given by the oceanic diffusion diagram in Okubo (1971). By inspection, Equation 4.6 predicts an infinite concentration at the bubble center $r = 0$. This occurs as a result of assuming a line source. The mass transfer Equation (4.4) assumes that the highest concentration of dissolved gas in the water column is $C_{s,i}$, which occurs at the bubble-water interface. Here, we apply Equation (4.6) at distances a minimum of the bubble radius away from the bubble center, and we ignore all concentration predictions greater than $C_{s,i}$. Because the dissolution rate is slow and the turbulent diffusion is comparably fast, only a very small region near the bubble is neglected due to these approximations.

4.3 Data for Simulation

We apply the model developed above to a natural gas seep site in the northern Gulf of Mexico. The GISR Consortium conducted two research cruises to Woosley Mound, located in Mississippi Canyon Federal Lease Block 118 (MC 118) in July 2014 (cruise G07) and April 2015 (cruise G08). The Woosley Mound is located at 890 m of water depth, below the hydrate stability level. The GISR cruises collected physical and chemical data from water samples within and near the seep bubble flare and observed the characteristics of bubbles using acoustic and optical sensors. In this paper, we consider the data from the G08 cruise because during that cruise concentration data were collected along horizontal transects through the bubble flare that can be compared to the predictions of our concentration model of Section 4.2.3.

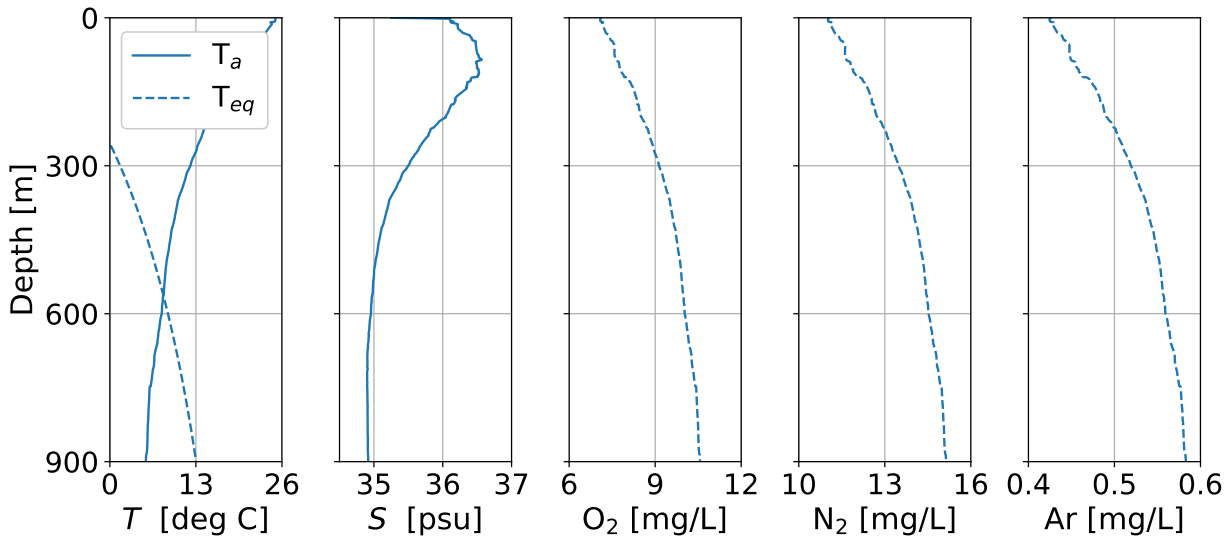

Figure 4.2: Vertical profiles of temperature (T), salinity (S), and dissolved gases (O_2, N_2, Ar) at MC 118 site during GISR cruise. The solid lines show the measured data, and the dashed lines indicate the calculated value from the TAMOC model.

4.3.1 Ambient Conditions

The ambient conductivity, temperature, and depth (CTD) data were obtained from a SeaBird (Sea-Bird SBE 49 FastCAT) CTD mounted on the frame of the ROV. The ambient water column profiles are shown in Figure 4.2. The temperature and conductivity profiles were measured with the CTD on the ROV, and the hydrate equilibrium temperature T_{eq} and the concentrations of dissolved gases (oxygen, nitrogen, and argon) are calculated by the model. Dissolved gas concentrations are estimated by computing the aqueous solubility of air at sea surface and then correcting for seawater compressibility and temperature through the water column. The estimated argon and nitrogen concentration are similar to the profiles in Pilson (2013), Hamme & R. Emerson (2004), and McGinnis et al. (2006). Biological processes may alter the oxygen profile, and the estimate computed here is used for lack of any observational data.

For the ambient current data, we use observations for local Acoustic Doppler current profilers (ADCP). We obtain the data from station 42883 from the National Data Buoy Center (NDBC) of the National Oceanic and Atmospheric Administration (NOAA). Station 42883 was operated at

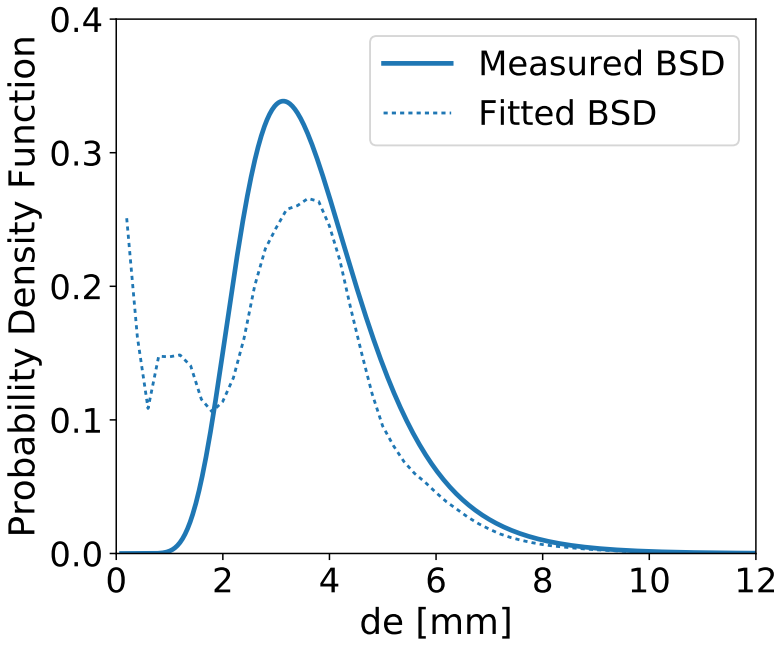

Figure 4.3: Measured bubble size distribution with the fitted log-normal distribution for Woosley Mound at MC 118 site during GISR cruise.

MC 118 during the G08 cruise, and it was the closest station, 2 km from Woolsey Mound seep, in the database. The main current oscillations on the Gulf of Mexico continental shelf are inertial, with periods of about 24 hours (DiMarco & Reid 1998); hence, for all numerical simulations, we use the 3-hourly averaged currents.

4.3.2 Characteristic of Bubbles

During the GISR cruises, the size distribution of seep bubbles at the source were measured using a high-speed stereoscopic camera system mounted on a Remotely Operated Vehicle (ROV). For the simulations, the data for the size distribution of bubbles is fitted with a log-normal distribution with a mean diameter $\mu = 1.267$ mm and standard deviation $\sigma = 0.3532$ mm, as shown in Figure 4.3; note that the arithmetic mean of a log-normal distribution is $\exp(\mu + \sigma^2/2)$. Figure 4.3 shows the measured bubble size distribution at the source point with the fitted log-normal distribution.

The flow rate of gas was also computed using the stereoscopic camera system by counting

bubble of observed volume as they passed a virtual horizontal plane. The methodology for bubble size distribution and volume flow rate for the G08 cruises was the same as that reported by Wang et al. (2016) for the G07 cruise. The averaged gas flow rate was 1 L/min.

In addition, the composition of the emitted bubbles was obtained from samples of gas collected at the seep source that were analyzed by Gas Chromatography (GC). The averaged gas composition in the bubbles during the G08 cruise was 68.73 % of methane, 2.46 % of ethane, 1.48 % of propane, 19.21 % of nitrogen, and 1.68 % of carbon dioxide.

4.3.3 Acoustic Investigation

Three different acoustic platforms were applied during the GISR G08 cruise to observe the signature of the bubble flares in the water column. Similarly to that reported in Section 3, a haul-mounted Kongsberg acoustic multibeam profiler (EM 302, 30 kHz) and an ROV-mounted Kongsberg multibeam echosounder (M3, 350 kHz) were used. The EM 302 was oriented normal to the ship beam and down-looking; the M3 was mounted in a forward-looking orientation with the acoustic beams spread in a horizontal plane ahead of the ROV. In addition to these acoustic systems, several split-beam narrow-band acoustic transducers were mounted on the rear of the ROV, with their pencil beam oriented in a down-looking path. This latter set of acoustic instruments allow for more detailed analysis of the spectral response of the bubble backscatter. Herein, we use the EM 302 data to observe the trajectory of the bubble flares throughout the water column and the M3 data to compare to the bubble spreading in the horizontal planes at several interrogation heights. Figure 4.4 shows the schematic diagram of acoustic investigations using EM 302 and M3 acoustic multibeam systems during GISR cruise. All data sets for the GISR cruise are available through the Gulf of Mexico Research Initiative Information and Data Cooperative (GRIIDC) (Socolofsky 2016*b*).

4.3.4 Water Column Concentration Data

Water samples for dissolved methane concentration and stable carbon isotopic ratio analysis were collected within the water column using the ROVs Hercules and Argus. The two ROVs were

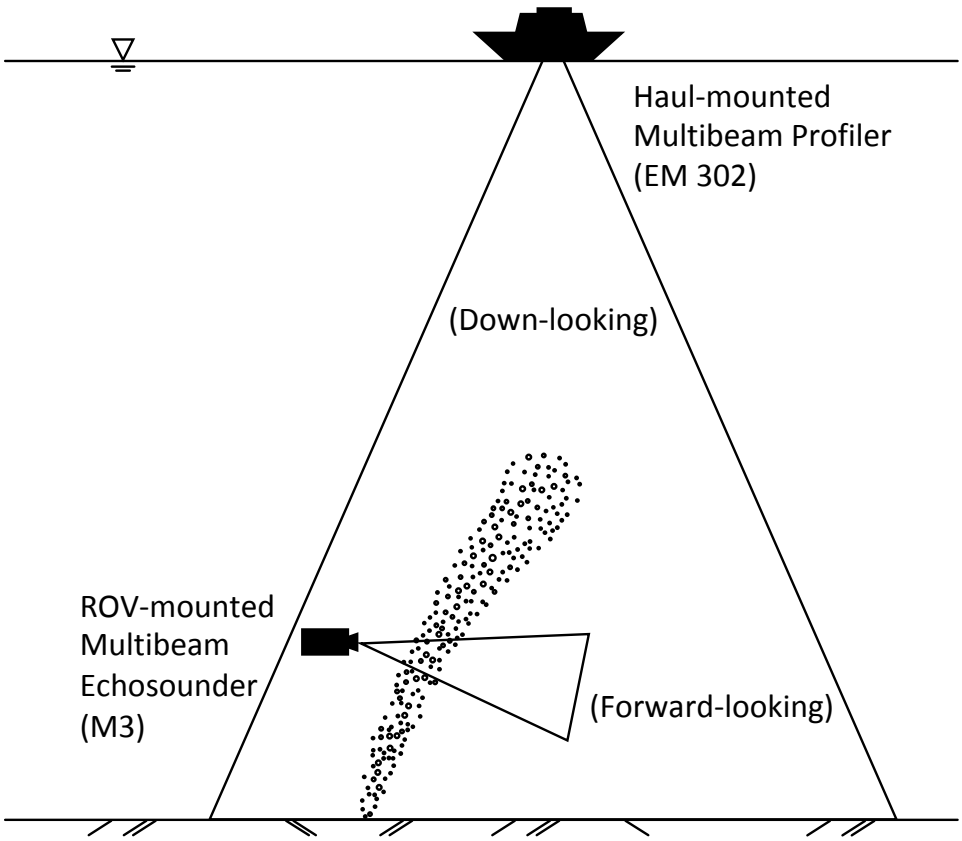

Figure 4.4: Schematic diagram of acoustic investigations in GISR cruises.

connected in tandem such that the Hercules, which carried acoustic instrumentation and water sampling equipment, was visible using the cameras mounted on the Argus. Precise positioning inside or outside the bubble flare was achieved using the HD camera and M3 sonar system mounted on ROV Hercules. Water was collected using a flexible tube attached to the starboard manipulator arm of the ROV which was directly visible on the ROV cameras, allowing the manipulator arm to position the intake port within centimeters of the desired sample site. Water was pumped through the flexible tube to one of 11 two-liter PerFluoroAlkoxy (PFA) plastic bottles using the Suspended Particulate Rosette (SUPR) sampler (Breier et al. 2014). The inlet tube was also outfitted with a deflector shield to eliminate ingestion of gas-phase bubbles during sampling. Sample bottles were filled with water onboard the ship before deployment to maintain pressure as the ROV descended through the water column. Thus, the bottles were flushed five times during sampling to prevent any contamination (Breier et al. 2014). Once the ROV was recovered on deck, water was carefully transferred from the sample bottles to glass vials to prevent any bubble formation or contamination. After vials were capped, a headspace was introduced into each vial, and then water samples were preserved using a supersaturated solution of mercuric chloride ($HgCl_2$). Analysis of dissolved methane, ethane, propane, and n-butane concentrations were performed on board using a gas chromatograph equipped with a flame ionization detector (Agilent). Water samples were analyzed for dissolved methane 13C isotopic ratios at the Woods Hole Isotope Laboratories, and more detailed methods can be found in Leonte et al. (2018). Data can be found on the Gulf of Mexico Research Initiative Information and Data Cooperative (GRIIDC) (Kessler & Leonte 2015).

4.4 Results

We use the complete model system to investigate the behavior and fate of bubbles from the natural seep through the water column. For the gas phase transport, we compare the simulation results with the acoustic measurements for the vertical trajectory of the seep flare (EM 302 data) and the horizontal spreading of the bubble cloud (M3 data). On the other hand, for the dissolved phase, we verify the model using the *in situ* water samples that were analyzed for dissolved methane gas from the natural seep.

4.4.1 Transport of Bubbles from Natural Seeps

4.4.1.1 Vertical Trajectories of Seep Bubbles

Using the measured boundary conditions of bubble size distribution, gas flow rate, and gas composition, we simulate bubbles released from the Woosley Mound vent at 890 m of water depth in the Gulf of Mexico. For the simulation, we randomly generate 500 bubbles based on the fitted log-normal distribution and match the volume flux of total bubbles with the measured gas flow rate by a scaling factor. We compare the trajectory of bubbles with the acoustic observations of water column anomalies of the seep from the EM 302 acoustic survey. GISR carried out 19 acoustic surveys for the MC 118 site during the G07 cruise and 61 acoustic surveys during the G08 cruise. We extract the water column backscatter data using the Water Column module of Fledermaus, the multibeam processing software package by Kongsberg. For the model-data comparison, we synthesized the multiple tracks of data into groups of two to three hours based on the measurement time and the shape of the acoustic anomalies. Details of the acoustic survey using the EM 302 and the data handling procedures are explained in Appendix A.

Figure 4.5 shows the comparison between the modeled bubble trajectories and the measured EM 302 water column backscatter in the G08 cruise. The light gray points are the measured position of bubbles in the water column from the acoustic surveys and show the observed trajectories of the natural seep. The colored lines show the centerline of the simulated bubble column; the width and color of the centerline trajectory both depict the ratio of the local bubble mass flux to the initial mass flux at the seep source. In several cases between April 10 and April 11, 2015, the simulated bubble trajectories do not agree with the measurements, especially in the North-South direction. However, in the rest of the cases, the modeled bubble trajectories are comparable with the measured acoustic anomalies. This comparison shows that for the most part the current data used in the simulations (obtained from a nearby ADCP in the G08 case) are representative of the currents near the seep. Also, since most of the other data, M3 images and water sampling, were measured between April 13 and April 18 in 2015, we could use this current data for the simulation.

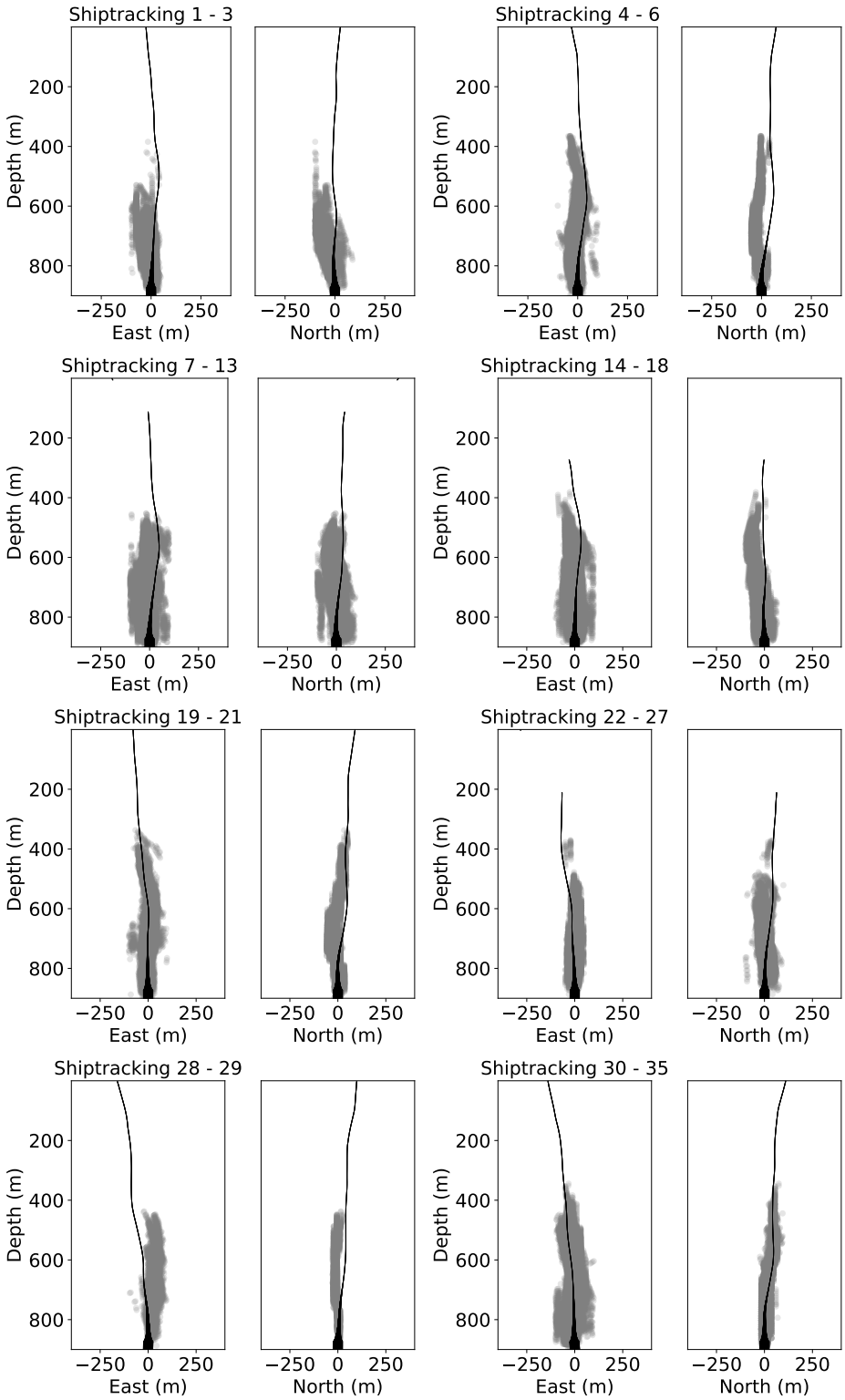

Figure 4.5: Comparison of the modeled bubble trajectory and mass flux (colored lines) to the measured EM 302 water column backscatter (gray data points) at MC 118 site during the G08 cruise.

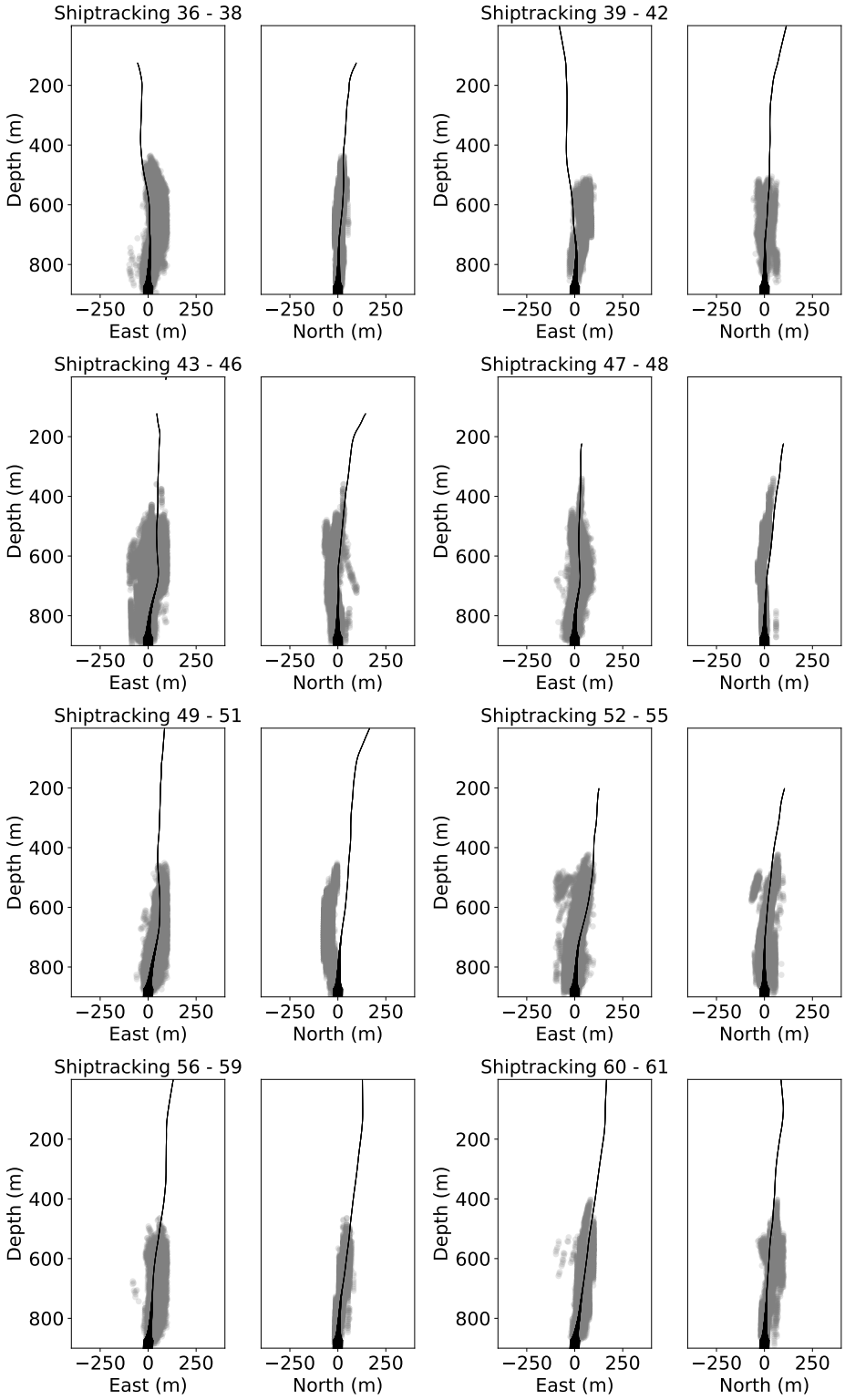

Figure 4.5: Continued

Table 4.1: The information of measurements of M3 data and the sampling of dissolved methane gas.

Case	Altitude	Dive	Date	Range of Concentration	No. of Samples
1	H = 90 m	H1402	April-13-2015	[0.498 - 95.712] μM	9
2	H = 200 m	H1407	April-18-2015	[0.258 - 1.675] μM	7
3	H = 300 m	H1404	April-15-2015	[0.801 - 85.923] μM	9
4	H = 300 m	H1407	April-18-2015	[0.064 - 1.782] μM	6
5	H = 400 m	H1406	April-18-2015	[0.133 - 2.209] μM	10

As seen in the figure, the bubble mass flow rate decreases quickly above the seafloor. This indicates that continuous dissolution of gas through the water column keeps most of the gas dissolved into the ocean before reaching the maximum flare height observed in the acoustic data. Also shown in the figure is that fact that small bubbles carrying less than 0.1 % of the initial mass flux continue above the acoustic anomaly, and this behavior was discussed in detail in Section 3.

4.4.1.2 Horizontal Spreading of Bubble Cloud

We simulate the horizontal spreading of bubbles from the natural seeps using the random walk model and qualitatively evaluate the transport characteristics of the simulated bubbles by comparing with the acoustic cross-section profiles observed by the M3 mounted on the ROV. The M3 data were collected at discrete heights, and here to compare to measurements at altitudes above the seafloor of 90 m, 200 m, 300 m, and 400 m, each height observed during different or multiple dives during the G08 cruise. Table 4.1 reports the detailed information of the acoustic surveys by the M3 sonar imaging.

In Figure 4.6, we compare acoustic images of the M3 (from dives H1402 to H1407) with model simulation results of the bubble flares at the same times and heights (Modeling result). The red square panels in the modeling results correspond to the field of view in the associated M3 acoustic image. In the M3 acoustic images, the color indicates the measured sound intensity in M3 images. Because the M3 is an uncalibrated instrument, these sound intensity values are with respect to an unknown reference; hence, no numerical scale for the color bar is given in the figure. For the modeling results, the color in the plot represents the simulated bubble size; each bubble

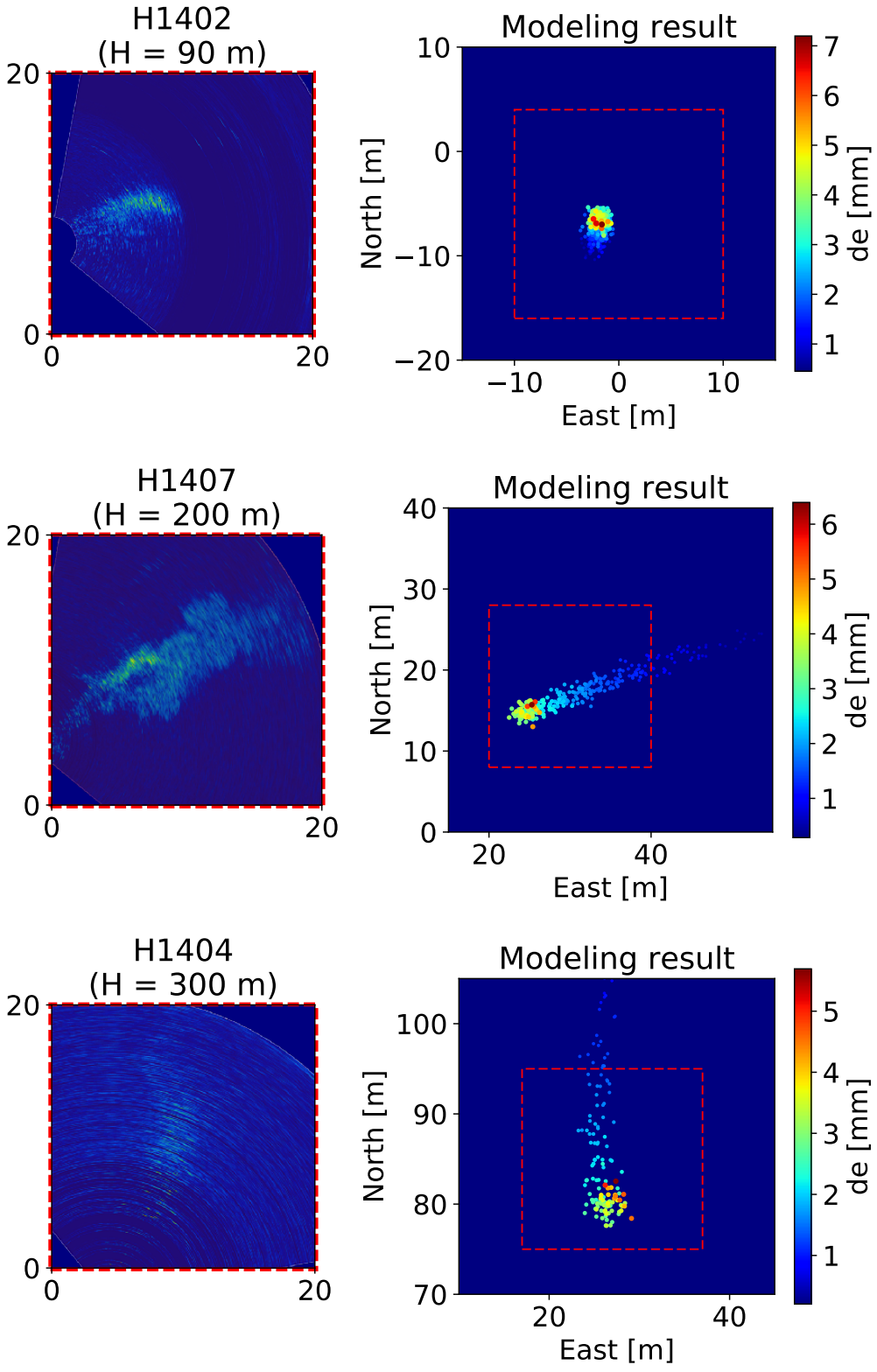

Figure 4.6: Comparison of the M3 acoustic images (H1402 - H1407) to the predicted bubble spreading (Modeling results) at different water depth during the G08 cruise.

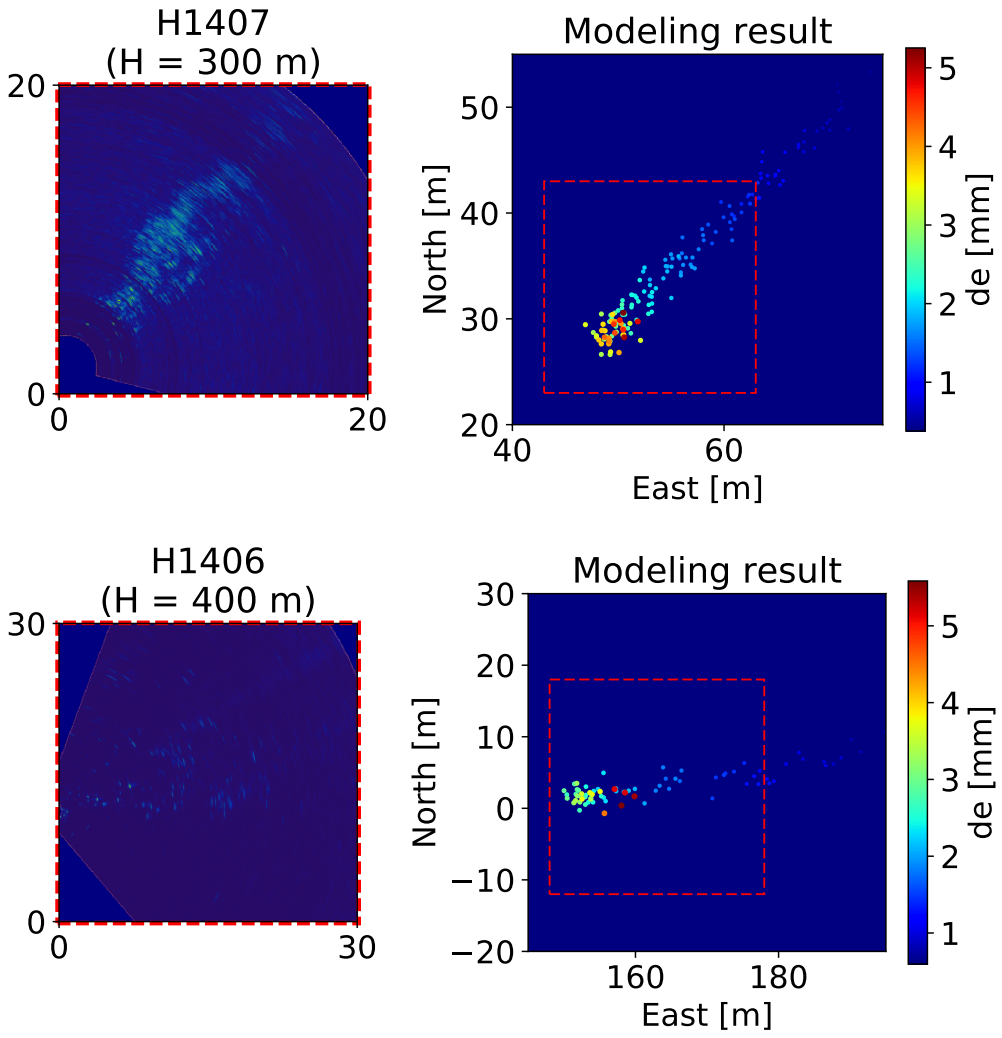

Figure 4.6: Continued

is represented by a single dot, and all dots are of the same diameter. The resonance frequency of a bubble depends on the frequency of insonification, the depth of water (hence, gas density), and the size of the bubble. Since the frequency of the M3 and the water depth remain the same for each pair of plots, the color intensity of acoustic data correlates to the bubble size. Hence, from this figure, we may evaluate the horizontal spreading of the bubbles qualitatively by comparing the color map of the bubble size distribution with the M3 acoustic images. Likewise, the ROV orientation and position in the water column is known at all times, and the model is driven by the measured currents so that we report in the figure the known orientation of the M3 image and the modeled distribution of the bubbles in the same coordinate system.

In each case, the shape of the bubble cloud, the size, and the direction of the bubble spreading from the simulation results are consistent with the observed M3 images. This indicates that the bubbles rise in the simulations at a similar rate and along similar trajectories to those in the field. However, it is difficult to compare the simulation results with the measurement for the lowest and the highest cases. For the lowest case (H = 90 m, H1402), the shape of the plume in the M3 image still depends on the shape of the distributed source. During the G08 cruise, the gas bubbles exited the seafloor behind the mouth of Wooley Mound, and the origin of individual gas streams was highly unsteady. Here, we initialize the model over a similar area to that observed in the field, but an instantaneous model-data comparison at this elevation is not strictly feasibly. At the same time, the signature of the bubbles near the top of the bubble flare is weak (H = 400 m, H1406) since bubbles are more scattered horizontally by the combination of the diffusion and advection as rising from the source. Also, the maximum flare height of the Woosley Mound flare during the G08 cruise was about 430$\pm$60 m from the bottom. Hence, only a few bubbles exist to pass through the measurement plane at the highest measurement point (H = 400 m).

Overall, the agreement between the M3 measurements and the simulations is good. The model captures the rising rate of the bubbles as witnessed by the similar lateral displacement of the larger bubbles in the M3 images and the model simulations. Likewise, the spread of the bubble flare in the downstream direction integrates all of the currents encountered below each measurement

height, giving further validation that the model predicts an accurate rise time and that the measured currents are representative of the field conditions at the seep site. Finally, the lateral spreading of the bubbles is similar to the measurements, supporting the fact that our random walk model with a constant diffusivity reasonably captures the behavior of bubble wobbling and turbulent diffusion responsible for the flare spreading. Hence, based on all of the acoustic data, we conclude that the bubble transport model in the SPM of TAMOC yields results consistent with the field observations.

4.4.2 Concentration Distribution of Dissolved Methane from Seeps

During the G08 cruise, the GISR consortium focused on the spatial distribution of dissolved seep gases on horizontal slices through the bubble flare. Table 4.1 reports the number of water column samples collected at each height for each dive and the range of the measured concentration. Figure 4.7 shows contour maps of the water column sampling results for dissolved methane for each of the surveys identified in Table 4.1. The general sampling plane was to collect the majority of samples along the long-axis of the bubble flare signatures in the M3 acoustic images, which were observed in real-time in the ROV control booth. Usually, two additional samples were taken along a transect perpendicular to the long axis of the bubble flare and through the region where the M3 reported the highest acoustic backscatter. In the figures, the long-axis of the bubble column is plotted along the x-axis; distances shown by the axis labels are approximate as the ROV was navigating a dynamic bubble flare field and correspond to M3 images captured at the start of sampling. Between 6 and 10 water samples were collected at each selected depth, with each survey taking on the order of one hour.

In this survey plan, no attempt was made to assess the local currents at each measurement plane. Instead, it was assumed that the long axis of the bubble flare in the M3 image would correspond with the downstream trajectory of dissolved methane. The range of measured concentration values is between 0.064 and 95.712 μM, and the GC used on the cruise had a detection limit of 1 nM with less than 5 % of measurement error. As seen in these raw data plots, in several cases, the location of the highest concentration of dissolved methane occurred in one of the samples from the transect perpendicular to the long axis of the bubble column—in other words, the maximum

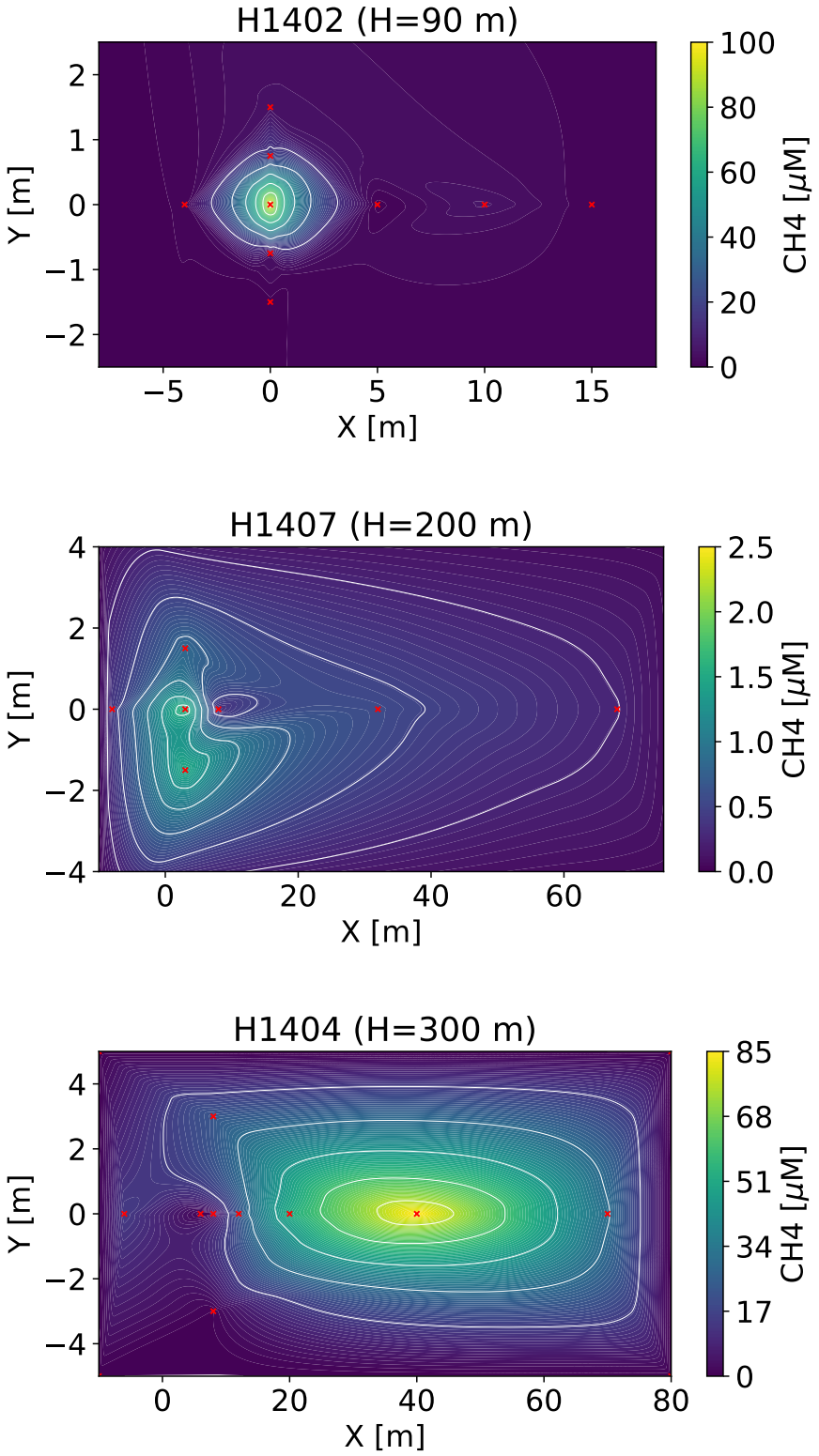

Figure 4.7: Measured horizontal concentration distribution of dissolved phase of methane from a natural seep for each case: (a) H1402 (H = 90 m), (b) H1407 (H = 200 m), (c) H1404 (H = 300 m), (d) H1407 ((H = 200 m), and (e) H1406 (H = 400 m)

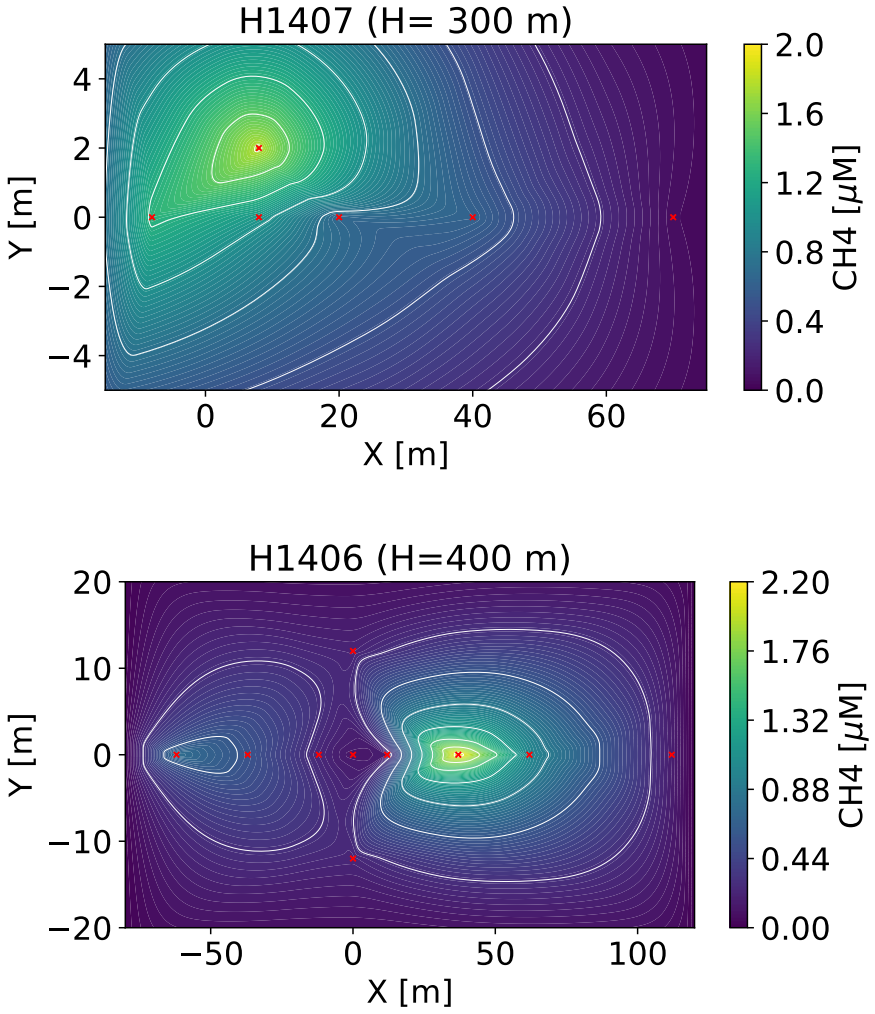

Figure 4.7: Continued

concentration was sometimes observed to the side of the bubble column and not in-line with the axis of the longitudinal bubble spreading.

Figure 4.8 shows the model simulation results for the concentration distribution of dissolved methane gas for each case using a different coordinate system from that in Figure 4.6. The x-axis in the figure subplots corresponds to the local current direction at each respective measurement depth. From these plots, it is immediately apparent that the bubble flares and dissolved-phase plume spread in different directions, with the highest concentration often not tracking the long-axis of the bubble signature.

This can be explained as follows. The locations of bubbles are given by their random spreading and the integration of the lateral currents from their release to the measurement location. In the rotating ocean, the Eckman boundary layer results in turning of the currents with height; moreover, there is no expectation that currents would follow a single direction throughout the water column. Hence, bubbles may be stretched in one direction at one height and another direction at another height. The direction is given by the long axis of the bubbles; therefore, is not expected to coincide with the local current direction at a given height. On the other hand, our analytical solution uses the local ambient currents to predict the dissolved phase transport and spreading. The fact that these two directions may be different (the long-axis of the bubble signature and the long-axis of the dissolved concentration distribution) is supported by our *in-situ* dissolved concentration measurements that often report the highest concentration on the side of the bubble column.

However, the direction of the concentration plume is not always captured in the measured data. This results from the course sampling scheme and the very low amount of diffusion occurring over the up to order 100 m of sample space of the measurements. Generally speaking, though, the measurements corroborate the model prediction that the bubble flare and dissolved concentration plume may not be aligned and likely will not be aligned when the currents turn with height. This fact can be used to design future sampling schemes that should take the local horizontal current direction into account at each measurement height.

Finally, we can compare the model predicted concentrations to the measured concentrations.

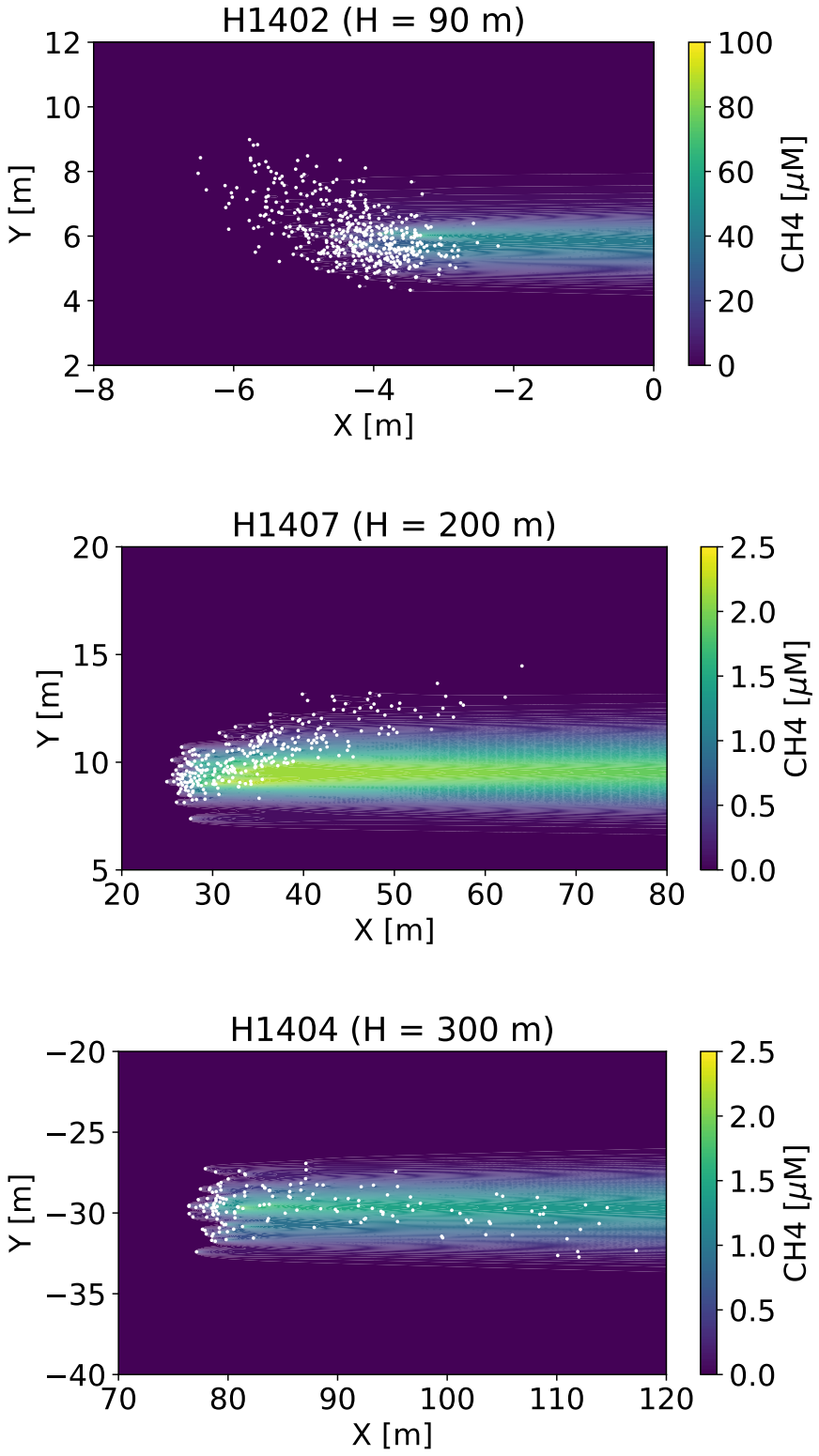

Figure 4.8: Simulation results of horizontal concentration distribution of dissolved phase of methane from a natural seep for each case: (a) H1402 (H = 90 m), (b) H1407 (H = 200 m), (c) H1404 (H = 300 m), (d) H1407 (H = 200 m), and (e) H1406 (H = 400 m).

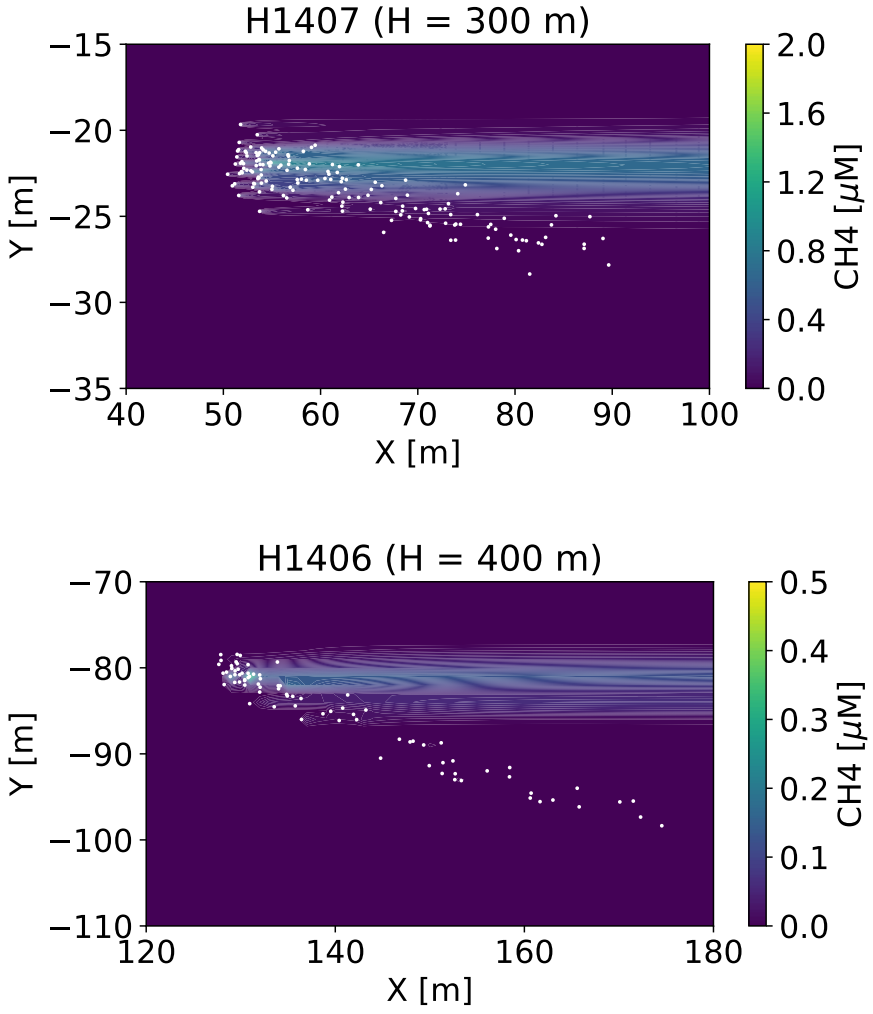

Figure 4.8: Continued

Again, due to the course sampling scheme and the very low opportunity for diffusion within this small area, the water column samples represent discrete points in a highly non-uniform concentration field. At all heights except $H = 300$ m on dive H1404, the model predicted the range of concentrations agrees well with the concentration range found in the sampling. For dive H1404, one sample peaked at near 85 μM; whereas, the model predicts concentrations of 2.5 μM and lower. This discrepancy could be partly related to the way the model limits the maximum concentrations near bubbles. Despite this single measurement, the model-data comparison for the remaining concentration measurements is good and has revealed an important element of the physics and chemistry of these seep flares: the bubbles and their dissolved concentration fields may not align due to the different way that the bubbles and dissolved concentration are advected vertically.

4.5 Conclusions

We validate the model performance for the transport of bubbles from the natural seep based on the acoustic measurements for the vertical trajectory of seep flares and the horizontal spreading of the bubble cloud. The results for the vertical transport of bubbles show that the bubble mass flow rate decreases quickly above the seafloor due to the continuous dissolution of gas through the water column. Most of the methane is dissolved into the water before reaching the maximum observed flare height in acoustic data. In addition, the results for the horizontal bubble cloud spreading agree with the observed M3 images at the different altitudes above the seafloor. Hence, based on all of the acoustic data, we confirm that the bubble transport model yields results consistent with the observations.

The results show that the bubbles and dissolved-phase plume spread differently. The locations of bubbles are given by their random spreading and the integration of the currents from their release to the measurement location. The dissolved concentration distribution follows the axis of the currents at the measurement height. These effects explain how the maximum measured concentration sometimes located at the edge of the bubble clouds. This is different from what was expected during the GISR cruises (the bubble and dissolved concentration distribution would be aligned) and provides the need to revise sampling plans for the future field campaigns.

5. MODEL APPLICATION FOR GAS SEEP BUBBLES ON CONTINENTAL SLOPE WITHIN HSZ

Overview The mechanisms controlling the fate of natural gas bubbles released from natural seeps on the continental margins remain an open question. The situation is complicated by the formation of clathrate hydrate skins that form on natural gas bubbles when they are released below the hydrate stability zone for the gas composition of the release. Increasingly, hydroacoustic measurements from haul-mounted split- or multi-beam echosounders are used to find new seep sites, and these observations consistently report the maximum height of rising of these bubble flares to coincide close to the top of the gas Hydrate Stability Level (HSL) whether bubbles are release close to or over a 1,000 m below the HSL. Previously, we have validated a new model for the effect of a hydrate skin that assumes that bubbles behave as clean bubbles after release until a characteristic transition time after which they behave as dirty. Clean and dirty bubble behavior follow classical empirical relationships in the literature; the transition time depends on the initial bubble size and the hydrate sub-cooling. In this paper, we show that no other mechanics are required for a model to agree with hydroacoustic measurements for bubbles released from arbitrary depths along the continental slope. The impressive height of rising observed for deep seep sites occurs because a large mass of gas is contained in the more dense bubbles and the transition to dirty behavior, with its associated slower mass transfer rates predict a long trajectory. These results can be used to develop new models of biogeochemical cycling of natural seep gases that are consistent with the qualitative behavior of most field observations.

5.1 Introduction

When a hydrocarbon bubble is naturally released from the seafloor, the bubble dissolves into seawater as it rises and expands as the pressure decrease through the water column (Brewer et al. n.d., Leifer & Patro 2002, MacDonald et al. 2002). The bubble tends to become smaller due to the dissolution and tends to become larger due to the expansion. The combination of dissolution and expansion determine the shrinkage rate of a rising bubble in the ocean. Additionally, if a hydrocarbon bubble is released from the deep ocean (below 400 m of depth), a thin hydrate shell may form on the surface of the bubble. The formation of the hydrate shell on the bubble slows down the dissolution of gas from the bubble to the ambient water compared to the dissolution rate of the bubble before hydrate forms. Hence, a bubble released below the Hydrate Stability Level (HSL) could be able to survive longer and rise higher because of the reduced dissolution rate by the hydrate shell. Indeed, submarine gas seeps located in the deep ocean are often observed to rise to the HSL independent of the source depth based on acoustic measurements for water column anomalies of seeps. It remains a challenge, however, for existing models to explain the significant flare heights within the Hydrate Stability Zone (HSZ) for a wide range of seep sites (McGinnis et al. 2006, Römer et al. 2012).

In this study, we apply the complete bubble model developed in the preceding sections of this thesis, which includes the hydrate effects on the dissolution and criteria for when the bubbles will become acoustically transparent, to predict the fate of gas bubbles from theoretical seeps on the continental shelf below the HSL. The model handles the change of dissolution rate due to the hydrate formation on the bubble surface and simulates different types of dissolution rates for a clean bubble, a dirty bubble, and a transition bubble due to the hydrate skin formation. We simulate several sizes of bubbles released at the different water depths and estimate the final rise height of bubbles within the HSZ. Figure 5.1 shows the characteristic behavior of natural seeps as observed in acoustic multibeam data.

In this section, we show that no additional mechanisms beyond those already implemented in our model are needed to reproduce these qualitative results. Notably, the bubbles do not cease to

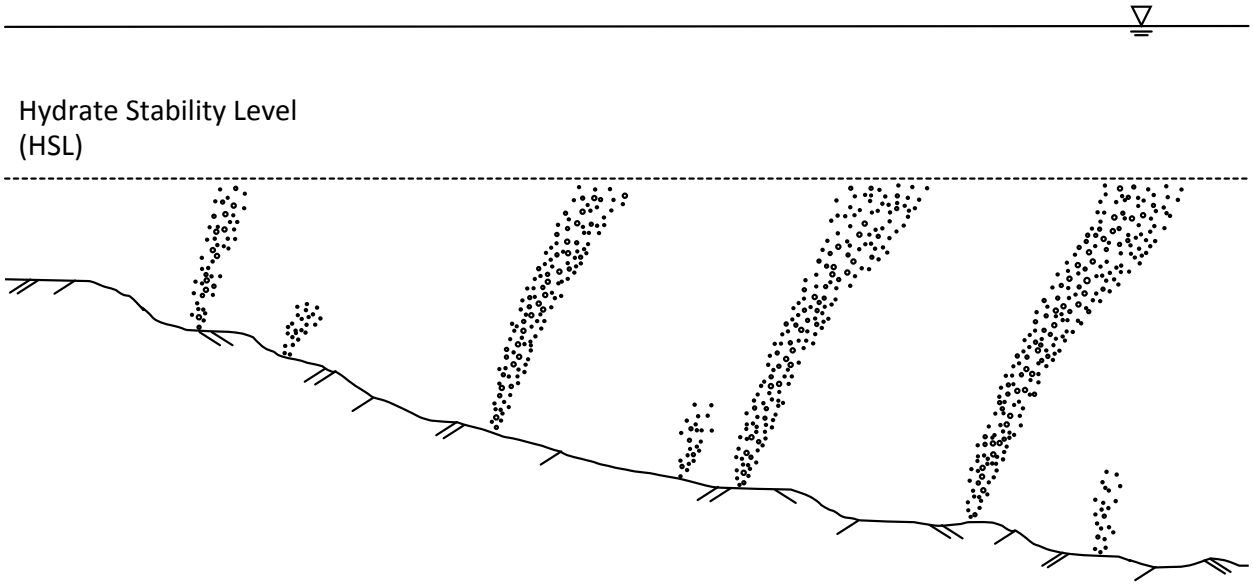

Figure 5.1: Schematic diagram of the simulation plan for the gas seeps on continental shelf below the HSL.

dissolve after formation of the hydrate shell and then suddenly rapidly dissolve after dissociation at the HSL. Instead, bubbles are continually dissolving and it is the fact that bubble size distributions are relatively similar from seep to seep and that deeper sites release more gas per bubble due to the compressibility resulting from the higher pressure that explains the data.

This section is organized as follows. In Section 5.2 we define a set of initial conditions for hypothetical *standard* seeps along the continental slope and a procedure to simulate them. The model results are presented in Section 5.3, including predictions for the height of rising and the vertical distribution of methane in the ocean water column originating from natural seep sources. Through these simulations, we show that dissolution is fast near the source so that most seep gases are sequestered below the ventilated upper mixed layer of the ocean. We end this section with a summary of the major conclusions in Section 5.4.

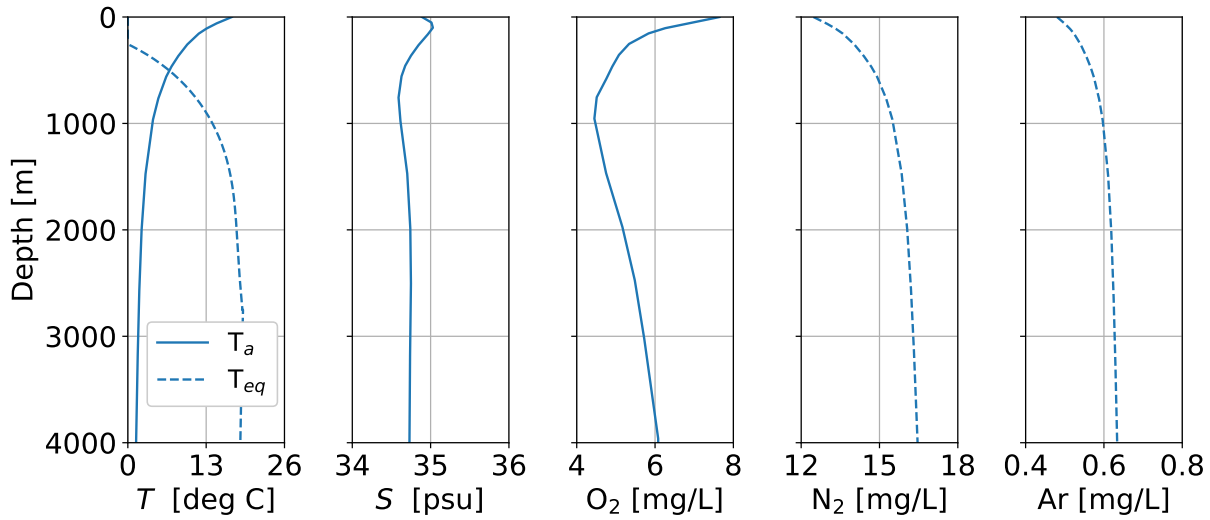

Figure 5.2: Vertical ambient profiles of temperature (T), salinity (S), and dissolved oxygen, argon, and nitrogen (O_2, Ar, N_2). The solid lines indicate the global averaged data from Sarmiento & Gruber (2006), and the dashed lines indicate the calculated value from TAMOC. T_a is the ambient temperature, and T_{eq} is the hydrate stability curve for methane gas.

5.2 Methodology

5.2.1 Ambient Conditions

The Hydrate Stability Zone (HSZ) and the Hydrate Stability Level (HSL) refer to a zone and a depth of the marine environment at which methane clathrates naturally exist in the Earth's crust (Sloan & Koh 2008). Garg et al. (2008) reported the HSL for pure methane gas exists from around 530 m depth at low latitudes, and around 250 m at high latitudes based on the vertical ocean profiles of temperature. Gas hydrate is a crystalline solid formed of hydrocarbon gas and water, which looks and acts like ice, and it remains stable within HSZ. About 95 % of hydrate deposits are found in the sediments of deep sea continental margins at depths of 500 to 3,000 m (Ruppel 2011). Thus, herein we simulate seep bubble flares released between 500 and 3,000 m of water depth.

The ambient water column profiles assumed in our simulations are shown in Figure 5.2. The global horizontal mean hydrographic and nutrient properties are obtained from Sarmiento & Gru-

ber (2006). Sarmiento & Gruber (2006) reported the temperature, salinity, oxygen (O_2) , phosphate (PO_4^{-3}), silicate (SiO_4^{-4}), and nitrate (NO_3^{-1}) profiles through the water column from the sea surface to 3,950 m of depth. The profiles for the other ambient dissolved gases, including nitrogen (N_2), and argon (Ar), are computed. To do that, we compute the aqueous solubility of air at the air-water interface, then correct for seawater compressibility and temperature through the water column.

5.2.2 Bubble Size Distribution

In Section 3, we investigated several methods to predict the maximum height of rising that would be observed in natural seep hydroacoustic data. The method with the lowest error only requires an estimate of the bubble size distribution as the top of the plume is defined as the point where bubbles of the size $d97$ to $d99$ become acoustically transparent, with target strength below the combination of the ambient noise and the noise of the instrument. Other methods also considered the mass flux of gas emitted at each site. Since we are considering hypothetical seep sources here, we will define the maximum rise height based on the bubble size distribution, especially the large bubbles (in the range of $d97$ - $d99$); hence, we do not need to define a mass flux.

5.2.3 Characteristic of Bubble: Thermogenic and Biogenic Methane

Typically, there are two types of gas seeps in the ocean: biogenic seeps and thermogenic seeps. The gas released is primarily methane of both biogenic and thermogenic origin (Schoell 1980). The biogenic hydrocarbon gases are overwhelmingly composed of methane gases, and they result from the productivity of natural bacterial activity which exists in sediment at and below the seabed (Parkes et al. 1990). In contrast, the thermogenic hydrocarbon gases usually occur at sub-bottom depths exceeding 1,000 m (Floodgate & Judd 1992) and are normally associated with petroleum reservoirs. The isotopic properties of methane and associated C2–C4 hydrocarbons indicate a thermogenic origin for such sites (Sassen & Macdonald 1997). We simulate both types of seep gas, and Table 5.1 shows the composition of gases we assumed for each type of hydrocarbon seeps.

Table 5.1: Molecular compositions of gases in a bubble for each type of hydrocarbon seeps.

	C1	C2	C3	N2	CO2
Biogenic gas (Methane gas)	100 %	0 %	0 %	0 %	0 %
Thermogenic gas (Natural gas)	95 %	3.2 %	0.2 %	1 %	0.5 %

5.3 Results

5.3.1 Final Rise Height of Seeps

We simulate bubbles originating as seep sites between 500 m and 3000 m depth with increments of 500 m. At each release depth, we simulate the dynamic trajectories of several different bubbles, each with a different initial bubble size. For each location and size, we run the model three ways: with bubble behavior given by clean bubble, with bubble behavior transitioning to dirty behavior after our validated transition time, and with bubble behavior matching dirty bubble throughout the simulation. Figures 5.3 and 5.4 show the bubble shrinkage as they rise through the water column for the typical bubble size for biogenic and thermogenic gas, respectively. Each line in each subplot represents a release from a different seep site; each subplot also reports the results for a different bubble size. The gray region at small bubble sizes (left-hand-side of each subplot) shows bubble sizes that would be acoustically transparent to a 30 kHz transducer; the intersection of each line in these subplots with this region gives the maximum height of rising that would be observed by such an instrument.

For all simulations using only clean bubble behavior, the bubbles rise at most 750 m above the source, and the deeper seeps never reach the HSL. This has been noted previously and is the reason that most models adapt the mass transfer rate to account for hydrates. At the same time, bubbles that are simulated as dirty bubbles throughout their trajectory consistently predict bubbles to rise much higher than the HSL, with 10 mm diameter bubbles reaching the surface for releases at 2,500 m or less for both biogenic and thermogenic methane. This observation is also contrary to multibeam data that show high rise heights, but few flares penetrating the HSL. Because neither of

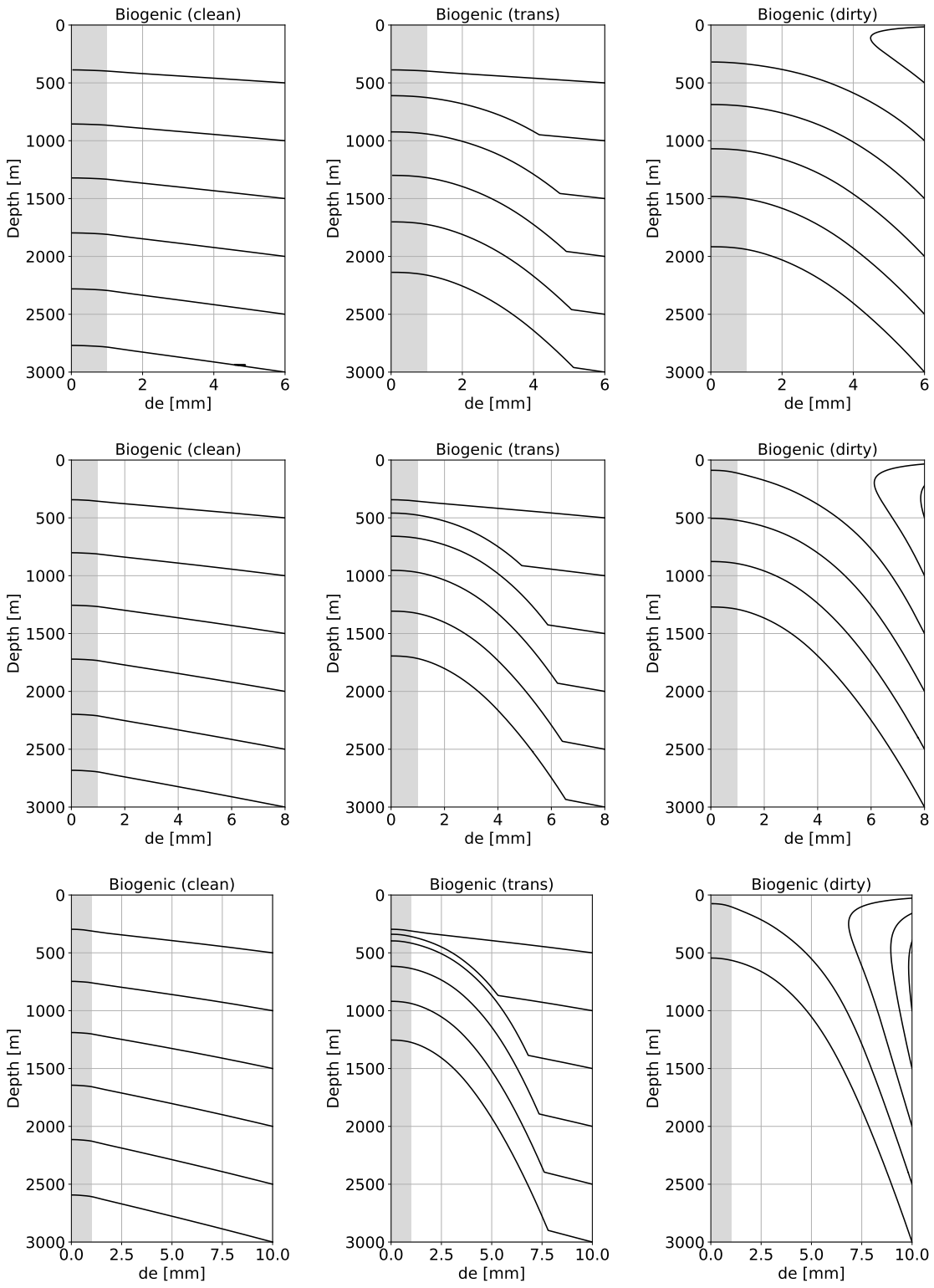

Figure 5.3: Shrinkage of bubble size during a bubble ascending for 6 mm, 8 mm, and 10 mm diameter of bubbles from the different water depth from the biogenic seep with three different mass transfer models: clean bubbles, dirty bubbles, and the transition time scale from clean to dirty used in TAMOC.

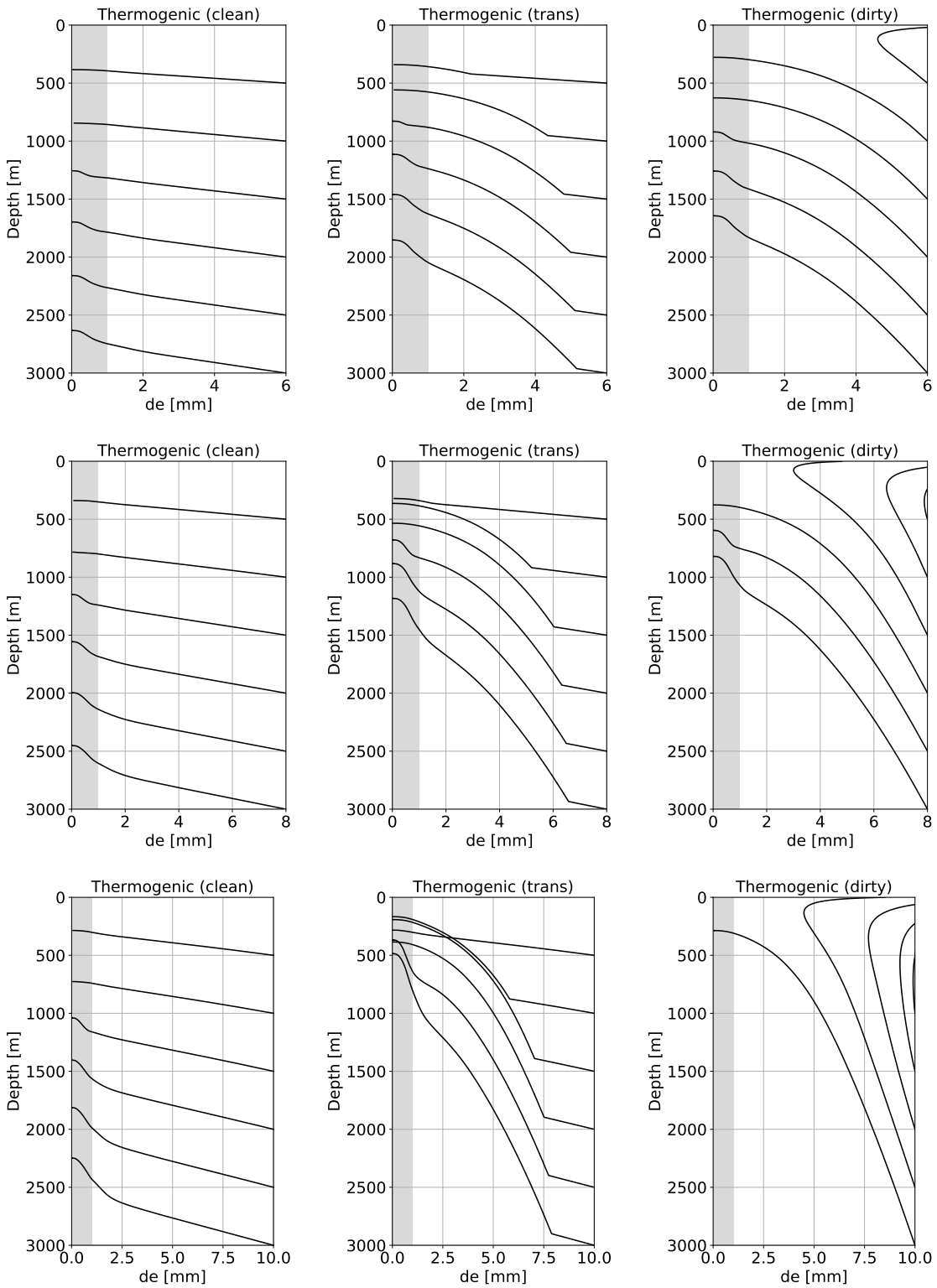

Figure 5.4: Shrinkage of bubble size during a bubble ascending for 6 mm, 8 mm, and 10 mm diameter of bubbles from the different water depth from the thermogenic seep with three different mass transfer models: clean bubbles, dirty bubbles, and the transition timescale from clean to dirty used in TAMOC.

these bubble models match the observations, hybrid approaches are needed to account for changes results from hydrate skin formation.

Our approach is plotted as the transition (trans) model in each of these figures. We allow bubbles to dissolve at clean rates immediately after release, and transition the bubble behavior to slower, dirty mass transfer rates after the transition time. Larger bubbles have longer transition times because it takes longer to populate their large surface area with hydrates or contaminants. Bubbles released deeper in the water column have shorter transition times because the greater hydrate sub-cooling accelerates the hydrate formation, reducing the transition time. Our model for the transition time was validated in Section 2.

The trajectory plots for the transition (trans) model generally show good agreement with the hydroacoustic data. Smaller bubbles, less than 8 mm rise significant distances, but those released from the deepest seeps do not rise all the way to the HSL of 300 to 500 m depth. This is true also for biogenic methane for the 10 mm diameter bubbles: there is a lot a convergence near 300 m depth for bubbles released at 1,500 m or shallower, but deeper releases do not rise all the way to the HSL. For thermogenic gas releases, the situation is different. This arises due to the small amount of ethane, propane released with these bubbles that have lower solubilities than methane. For the thermogenic case, the 10 mm bubble consistently rises near to the 300 m to 500 m depth.

From these results, we can state the reasons our model suggests that natural seep flares are observed to rise to heights near the HSL. First, mass transfer rates are fast initially after release and before the bubble-water interface becomes contaminated or covered with a hydrate skin. Second, the bubble sizes observed at natural seeps at various depths are very similar, with 10 mm bubbles being very common. Coupled with the gas compressibility with depth, 10 mm bubbles released at 3,000 m depth will contain about five times more gas than the same sized bubbles released at 500 m water depth. Third, bubble released deeper in the water column with the transition to dirty bubble (slower mass transfer) behavior faster owning to the higher hydrate sub-cooling, which results in more rapid hydrate skin formation on the bubbles. Fourth, bubble dissolves throughout their trajectories, and we do not change the mass transfer rates when bubbles cross the HSL. We continue

with dirty bubble rates since the bubbles will have aged and would very likely be contaminated by naturally occurring surfactants and particles in the oceans. Hence, it is the stable bubble size distribution and the compressibility that are the dominant reasons bubbles rise to the HSL with the mass transfer reduction after hydrate formation playing an important, but secondary role.

5.3.2 Hydrocarbon Gas Flux from Seeps

We can also plot the fraction of the initial hydrocarbon mass flux that has dissolved as a function of depth for each of the bubbles simulated above. These results are shown in Figures 5.5 and 5.6.

In these figures, only the results of the transition (trans) model are shown since these are the simulations with the best correspondence with the qualitative results of hydroacoustic observations. Each row of the figure is for a different initial bubble size (6 mm, 8 mm, and 10 mm diameter), and each column is for a different release depth. The gray region in the figures shows the region for which more than 99.9 % of the released gas is dissolved.

For the biogenic sources, the methane dissolves rapidly. Bubbles continue to rise through the water column, but quickly the methane is replaced by atmospheric gases stripped from the water column. In all cases, 99.9 % of the initial mass of methane is dissolved at or below 400 m water depth. Hence, these results suggest little methane reaches the atmosphere for biogenic seep sites.

For the thermogenic sources, the situation is somewhat more complicated. Methane is depicted by the solid line, and because it has the highest solubility of among the released hydrocarbon gases, it dissolves the most rapidly. In fact, 99.9 % of the released methane is dissolved in all cases at or below 300 m water depth. Ethane and propane start with much lower mass fractions than methane, and their curves cross the 99.9 % dissolved line higher in the water column. Because of their low initial mass fluxes, negligible amounts of these gases rise above 200 m water depth, the height was 99.9 % of their initial masses is dissolved.

Since the solubility of methane gas in the water increases with water depth and increasing pressure and decreasing temperature, the dissolution rate of methane gas increase as it goes deeper. Also, as the dissolution rate of methane gas is faster than other hydrocarbon gases, ethane and propane, methane dissolves preferentially first, and total methane dissolution occurs well below

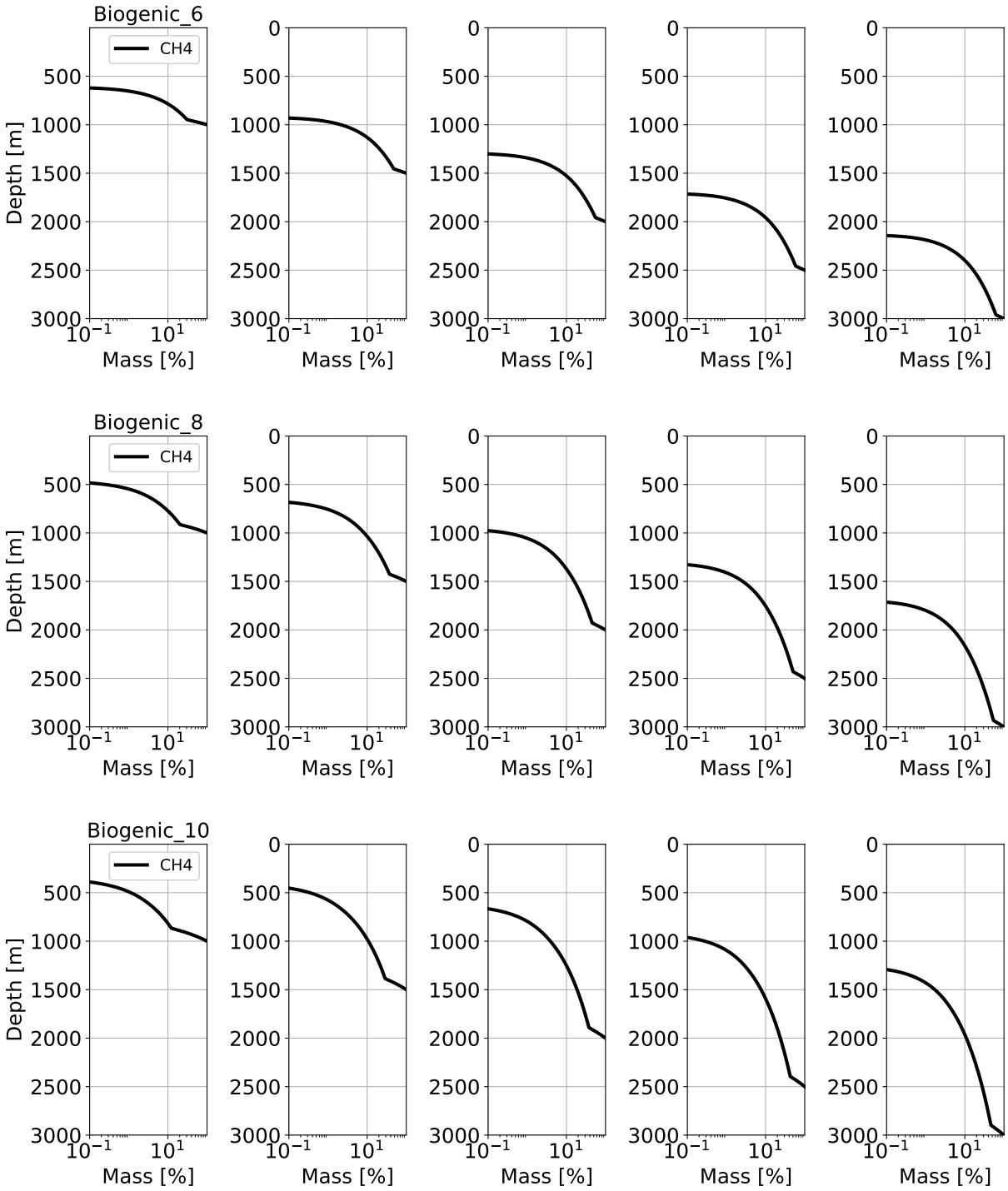

Figure 5.5: Mass remaining of hydrocarbons in a bubble for 6 mm, 8 mm, and 10 mm diameter of bubbles from the biogenic seep.

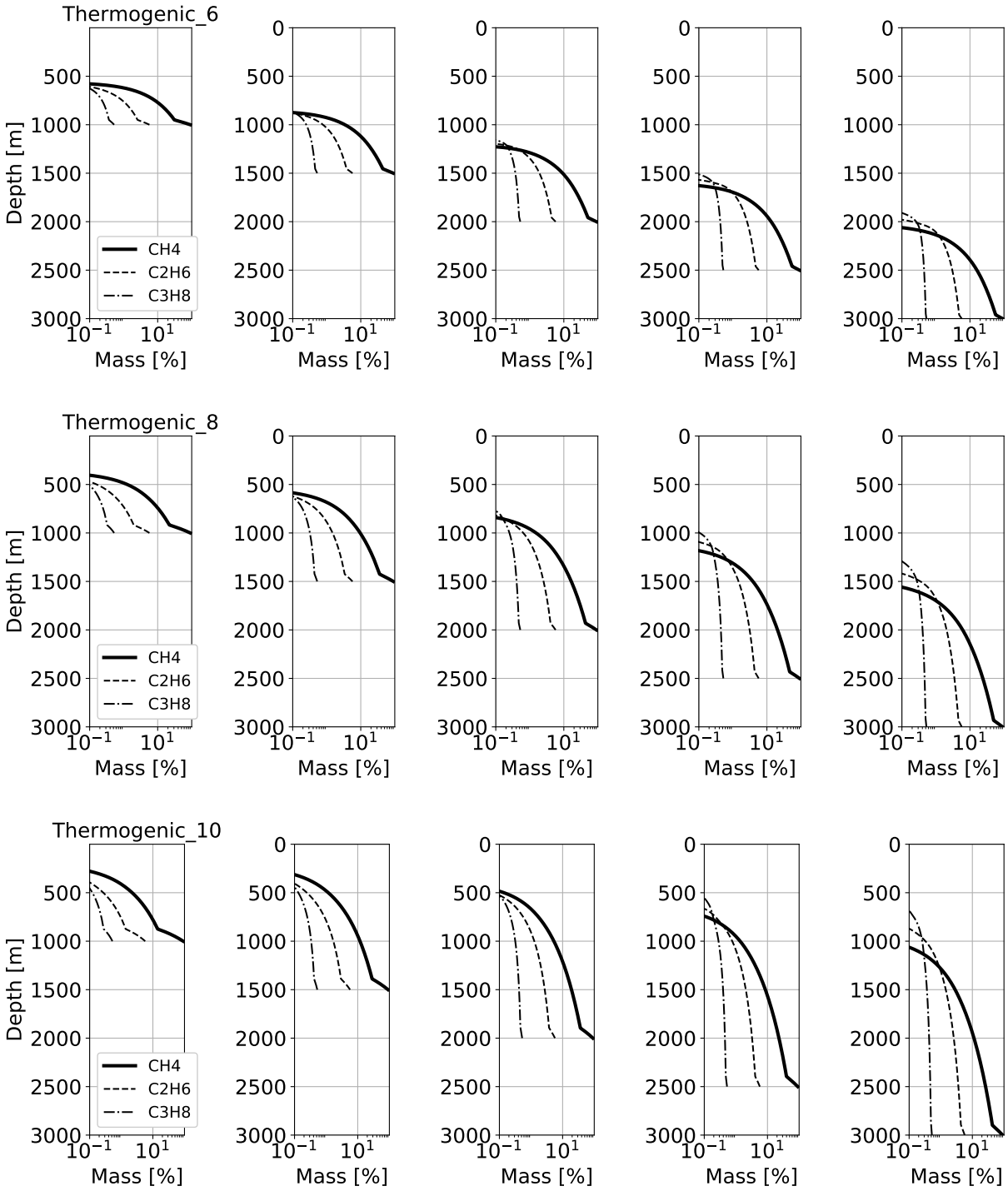

Figure 5.6: Mass remaining of hydrocarbons in a bubble for 6 mm, 8 mm, and 10 mm diameter of bubbles from the thermogenic seep.

the maximum height of rising of each bubble in most cases. Indeed, the bubbles that reach the maximum height of rising as observed in the hydroacoustic data mostly contain stripped atmospheric gases and small amounts of other gases besides methane that was released at the seep source.

5.4 Conclusions

The results of this study explain the fact that the final rise height of seep bubbles are usually located around the HSL with the acoustic measurements, even though bubbles are released at the different depth on the continental shelf. Also, the results show that if the initial bubble size is larger than 8 mm of diameter, then the bubble would be able to survive from any depth to HSL.

The developed model can handle the change of dissolution rate due to the hydrate formation on the bubble surface, and the model can simulate different types of dissolution rates for a clean bubble, a dirty bubble, and a transition bubble by the hydrate skin formation. The model could explain the observed extreme bubble rise height up to HSL only when we consider the transition of dissolution rate by the hydrate in the simulation. Hence, we confirm that the model with a transition time has the capability to make correct predictions of the fate of bubbles within the HSZ.

The model also predicts that the methane released from natural seeps on the continental slope is nearly completely dissolved low in the bubble flare, well below the height of maximum rise observed in hydroacoustic data and well below the upper ventilated layers of the ocean mixed layer. Hence, we conclude that natural seeps are likely a negligible source of methane to the atmospheric methane budget.

6. CONCLUSIONS

6.1 Summary of Present Findings

The overarching goal of this study is to develop a numerical model to predict the trajectory and dissolution of hydrocarbon bubbles emitted in deep oceans water column. At the same time, these findings enhance our fundamental understanding of the vertical oceanic transport of hydrocarbon gases escaping from the ocean to the atmosphere. In particular, this dissertation introduces a new numerical model for hydrocarbons bubbles within the HSZ of the ocean water column, which can account for the effect of hydrates on the bubble dynamics. The model is essential to predict the distribution of methane in the ocean water column from natural seeps or accidental blowouts.

- In Section 2, we developed a new model for hydrate skin formation on natural gas bubbles to predict the fate and transport of hydrocarbons within the HSZ. We found the correlation between the dissolution transition by hydrate formation and the initial bubble size and the degree of hydrate sub-cooling through the model calibration with *in-situ* measurements of pure methane. The developed model was confirmed by the direct observation of hydrate formation on bubbles with high-speed cameras.

- In Section 3, we used the complete model for predicting the rise heights for flares from natural gas seeps. We compared the simulation results with observed maximum flare rise height and explained where a natural seep would disappear in acoustic data. The outcome of this study is the optimal model for predicting the flare height and the estimation of methane flux from the seep site and its impact on the anthropogenic methane budget.

- In Section 4, we applied our model to simulate and explain the transport of bubbles from the natural seeps through the water column. We proved that the current data used in the simulations, which is obtained from a nearby ADCP in the G08 case, are representative of the currents near the seep. Also, by comparing results with the acoustic observation of

horizontal spreading of the bubble clouds, the model with the measured diffusion coefficient of bubbles for the field-scale plumes by GISR is validated. In addition, the simulation results for the prediction the dissolved hydrocarbon concentration around natural seeps explain the why the maximum measured concentration sometimes located at the edge of the distribution of bubbles.

- In Section 5, we applied our model to study the fate of methane released from two types of gas seeps, the biogenic seep and the thermogenic seep, along with the continental slope in the ocean. Overall, simulation results explain the fact that the final rise height of seep bubbles are usually located around the HSL even though bubbles are released at the different depth on the continental shelf.

In conclusion, the model developed in this study is important for understanding biogeochemical cycling of natural gas released from natural seeps as well as for predicting hydrate behavior in blowout plumes, where data are currently lacking.

6.2 Recommendations for Future Research

- The developed model can be coupled with other far-field models, such as GNOME and HYCOME. The model is a near-field model of the plume, and we focus on the transport of oil and gas around the plume. However, we need to understand the transport of hydrocarbon for the broader range of area in the ocean. Also, our model can provide accurate input data to the far-field models.

- The model can be used to simulate the Arctic gas hydrate in the future research. As the climate warms, it is important to understand the behavior of marine gas hydrate and the Arctic permafrost. In the Arctic (icy regions), gas hydrates even occur on the shallow water depth or on the land in permafrost. Pioneering researchers on gas hydrates expect that the frozen methane exists particularly abundant under Arctic ocean.

- The model can play a key role in an accidental blowout for both response-level models

and after-the-fact impact assessment in the future research. It is critical to understand the dynamic influence of hydrates on the transport of oil and gas. In the event of an accident, the model can predict where oil and gas will go and how much it will reach the surface then determine the protection strategy. After an accident, the model can be used to fill observation gaps and estimate the damage on the ocean environment.

REFERENCES

Adisasmito, S., Frank, R. J. & Sloan, E. D. (1991), 'Hydrates of carbon dioxide and methane mixtures', *Journal of Chemical & Engineering Data* **36**(1), 68–71.

Aiba, S. & Toda, K. (1964), 'Effect of surface active agent on oxygen absorption in bubble aeration II', *The Journal of General and Applied Microbiology* **10**(2), 157–162.

Anderson, K., Bhatnagar, G., Crosby, D., Hatton, G., Manfield, P., Kuzmicki, A., Fenwick, N., Pontaza, J., Wicks, M., Socolofsky, S., Brady, C., Svedeman, S., Sum, A. K., Koh, C., Levine, J., Warzinski, R. P. & Shaffer, F. (2012), 'Hydrates in the Ocean beneath, around, and above Production Equipment', *Energy & Fuels* **26**(7), 4167–4176.

Baird, M. H. I. & Davidson, J. F. (1962), 'Gas absorption by large rising bubbles', *Chemical Engineering Science* **17**(2), 87–93.

Ben-Naim, A. & Yaacobi, M. (1974), 'Effects of solutes on the strength of hydrophobic interaction and its temperature dependence', *Journal of Physical Chemistry* **78**(2), 170–175.

Bigalke, N., Enstad, L., Rehder, G. & Alendal, G. (2010), 'Terminal velocities of pure and hydrate coated CO_2 droplets and CH_4 bubbles rising in a simulated oceanic environment', *Deep Sea Research Part I: Oceanographic Research Papers* **57**(9), 1102 – 1110.

Bigalke, N. K., Rehder, G. & Gust, G. (2008), 'Experimental investigation of the rising behavior of CO_2 droplets in seawater under hydrate-forming conditions', *Environmental Science & Technology* **42**(14), 5241–5246.

Bozzano, G. & Dente, M. (2014), 'Dissolution of CO_2 and CH_4 bubbles and drops rising from the deep ocean', *Industrial & Engineering Chemistry Research* **53**(22), 9272 – 9281.

Breier, J. A. (2016), 'GISR: G07 Field Survey: Methane concentrations in gas plumes from Mississippi and Green Canyon Seeps in July 2014. distributed by: Gulf of Mexico Research Initiative Information and Data Cooperative (GRIIDC), Harte Research Institute, Texas A&M University, Corpus Christi'.

Breier, J. A., Sheik, C. S., Gomez-Ibanez, D., Sayre-McCord, R. T., Sanger, R., Rauch, C., Cole-

man, M., Bennett, S. A., Cron, B. R., Li, M., German, C. R., Toner, B. M. & Dick, G. J. (2014), 'A large volume particulate and water multi-sampler with in situ preservation for microbial and biogeochemical studies', *Deep Sea Research Part I: Oceanographic Research Papers* **94**, 195 – 206.

Brewer, P. G., Friederich, G., Peltzer, E. T. & Orr, F. M. (1999), 'Direct experiments on the ocean disposal of fossil fuel CO_2', *Science* **284**(5416), 943–945.

Brewer, P. G., Orr, F. M., Friederich, G., Kvenvolden, K. A. & Orange, D. L. (1998), 'Gas hydrate formation in the deep sea:âĂL' in situ experiments with controlled release of methane, natural gas, and carbon dioxide', *Energy & Fuels* **12**(1), 183–188.

Brewer, P. G., Paull, C., Peltzer, E. T., Ussler, W., Rehder, G. & Friederich, G. (n.d.), 'Measurements of the fate of gas hydrates during transit through the ocean water column', *Geophysical Research Letters* **29**(22), 38–1– 38–4.

Brewer, P. G., Peltzer, E. T., Friederich, G. & Rehder, G. (2002), 'Experimental determination of the fate of rising CO_2 droplets in seawater', *Environmental Science & Technology* **36**(24), 5441–5446.

Bryant, L. D., Gantzer, P. A. & Little, J. C. (2011), 'Increased sediment oxygen uptake caused by oxygenation-induced hypolimnetic mixing', *Water Research* **45**, 3692–3703.

Calderbank, P. H. & Lochiel, A. C. (1964), 'Mass transfer coefficients, velocities and shapes of carbon dioxide bubbles in free rise through distilled water', *Chemical Engineering Science* **19**(7), 485–503.

Chapoy, A., Mohammadi, A. H., Richon, D. & Tohidi, B. (2004), 'Gas solubility measurement and modeling for methane-water and methane-ethane-*n*-butane-water systems at low temperature conditions', *Fluid Phase Equilibria* **220**, 113–121.

Chen, F. & Yapa, P. D. (2001), 'Estimating hydrate formation and decomposition of gases released in a deepwater ocean plume.', *Journal of Marine Systems* **30**, 21–32.

Chen, F. & Yapa, P. D. (2004), 'Modeling gas separation from a bent deepwater oil and gas jet/plume.', *Journal of Marine Systems* **45**, 189–203.

Claussen, W. F. & Polglase, M. F. (1952), 'Solubilities and structures in aqueous aliphatic hydrocarbon solutions', *Journal of the American Chemical Society* **74**, 4817–4819.

Clift, R., Grace, J. R. & Weber, M. E. (1978), *Bubbles, Drops, and Particles*, Academic Press, New York, NY.

company, K. (2018), 'Multiflash software program', https://www.kbc.global/software/simulation-and-optimization/advanced-thermodynamics. Accessed: 2018-10-05.

Coppock, P. D. & Meiklejohn, G. T. (1951), 'The behaviour of gas bubbles in relation to mass transfer', *Transactions of the Institution of Chemical Engineers* **29**, 75–86.

Cosgrove, B. A. & Walkley, J. (1981), 'Solubilities of gases in H_2O and ^2H_2O', *Journal of Chromatography A* **216**, 161–167.

Culbersion, O. L. & McKetta, J. J. (1951), 'Phase equilibria in hydrocarbon-water systems III - the solubility of methane in water at pressures to 10,000 psia', *Petroleum Transactions* **192**, 223–226.

Danesh, A. (1998), *PVT and Phase Behavior of Petroleum Reservoir Fluids*, Elsevier, Amsterdam, the Netherlands.

Davenport, W. G., Richardson, F. D. & Bradshaw, A. V. (1967), 'Spherical cap bubbles in low density liquids', *Chemical Engineering Science* **22**(9), 1221–1235.

Davies, R. M. & Taylor, G. (1950), 'The mechanics of large bubbles rising through extended liquids and through liquids in tubes', *Proceedings of the Royal Society of London. Series A, Mathematical and Physical Sciences* **200**(1062), 375–390.

Denison, D. G., Holmes, C. C., Mallick, B. K. & Smith, A. F. M. (2002), *Bayesian Methods for Nonlinear Classification and Regression.*, Wiley series in probability and statistics, Chichester : Wiley.

DiMarco, S. F. & Reid, R. O. (1998), 'Characterization of the principal tidal current constituents on the texas-louisiana shelf', *Journal of Geophysical Research: Oceans* **103**(C2), 3093–3109.

Dissanayake, L. A., Gros, J. & Socolofsky, S. A. (2018), 'Integral models for bubble, droplet, and multiphase plume dynamics in stratification and crossflow', *Environmental Fluid Mechanics*

pp. 1–36.

Dissanayake, L. A., Jun, I. & Socolofsky, S. A. (2015), 'Numerical models to simulate oil and gas blowout plumes and associated chemical and physical processes of hydrocarbons', *E-proceedings of the 36th IAHR world congress* **28**.

Duffy, J. R., Smith, N. O. & Nagy, B. (1961), 'Solubility of natural gases in aqueous salt solutions I. liquidus surfaces in the system CH_4-H_2O-$NaCl_2$-$CaCl_2$ at room temperatures and at pressures below 1,000 psia', *Geochimica et Cosmochimica Acta* **24**, 23–31.

Exline, J. D., Levine, A. S. & Levine, J. S. (2006), *Meteorology: An Educator's Resource for Inquiry-Based Learning for Grades 5-9*, National Aeronautics and Space Administration (NASA), Hampton, VA: Langley Research Center.

Fan, L.-S. & Tsuchiya, K. (1990), *Bubble wake dynamics in liquids and liquid-solid suspensions*, Butterworth-Heinemann series in chemical engineering, Butterworth-Heinemann.

Fan, L.-S., Yang, G., Lee, D., Tsuchiya, K. & Luo, X. (1999), 'Some aspects of high-pressure phenomena of bubbles in liquids and liquid-solid suspensions', *Chemical Engineering Science* **54**(21), 4681–4709.

Floodgate, G. & Judd, A. (1992), 'The origins of shallow gas', *Continental Shelf Research* **12**(10), 1145 – 1156. Methane in Marine Sediments.

Garg, S., Pritchett, J., Katoh, A., Baba, K. & Fujii, T. (2008), 'A mathematical model for the formation and dissociation of methane hydrates in the marine environment', *Journal of Geophysical Research-Solid Earth* **113**(B1).

Gros, J., Arey, J. S., Socolofsky, S. A., Dissanayake, A. L., Jun, I., Zhao, L., Boufadel, M. C. & Reddy, C. M. (2017), 'Petroleum dynamics in the sea and influence of subsea dispersant injection during deepwater horizon', *Proceedings of The National Academy of Sciences of The United States of America* **114**(38), 10065 – 10070.

Gros, J., Reddy, C. M., Nelson, R. K., Socolofsky, S. A. & Arey, J. S. (2016), 'Simulating gas-liquid-water partitioning and fluid properties of petroleum under pressure: Implications for deep-sea blowouts', *Environmental Science & Technology* **50**(14), 7397 – 7408.

Guthrie, R. I. L. & Bradshaw, A. V. (1973), 'Spherical capped gas bubbles rising in aqueous media', *Chemical Engineering Science* **28**(1), 191–203.

Guyer, A. & Pfister, X. (1946), 'Über die Absorption von Gasblasen I', *Helvetica Chimica Acta* **29**(5), 1173–1183.

Haberman, W. L. & Morton, R. K. (1953), *An experimental investigation of the drag and shape of air bubbles rising in various liquids*, Navy Department, Washington, D. C.

Hamme, R. & R. Emerson, S. (2004), 'The solubility of neon, nitrogen and argon in distilled water and seawater', *Deep Sea Research Part I: Oceanographic Research Papers* **51**, 1517–1528.

Hammerton, D. & Garner, F. H. (1954), 'Gas absorption from single bubbles', *Transactions of the Institution of Chemical Engineers* **32**, S18–S24.

Hayduk, W. & Laudie, H. (1974), 'Prediction of diffusion coefficients for nonelectrolytes in dilute aqueous solutions', *American Institute of Chemical Engineers Journal* **20**(3), 611–615.

Houghton, G., Ritchie, P. D. & Thomson, J. A. (1957), 'Velocity of rise of air bubbles in sea-water, and their types of motion', *Chemical Engineering Science* **7**(1-2), 111–112.

Jähne, B., Heinz, G. & Dietrich, W. (1987), 'Measurement of the diffusion coefficients of sparingly soluble gases in water', *Journal of Geophysical Research: Oceans* **92**(C10), 10767–10776.

Johansen, Ø. (2000), 'Deepblow-a lagrangian plume model for deep water blowouts.', *Spill Science and Technology Bulletin* **6**(2), 103–111.

Johansen, Ø. (2003), 'Development and verification of deep-water blowout models.', *Marine Pollution Bulletin* **47**(9), 360–368.

Johansen, Ø., Rye, H. & Cooper, C. (2003), 'Deepspill-field study of a simulated oil and gas blowout in deep water.', *Spill Science and Technology Bulletin* **8**(5-6), 433–443.

Johnson, A. I., Besik, F. & Hamielec, A. E. (1969), 'Mass transfer from a single rising bubble', *Canadian Journal of Chemical Engineering* **47**(6), 559–564.

Judd, A. G. (2004), 'Natural seabed gas seeps as sources of atmospheric methane', *Environmental Geology* **46**(8), 988–996.

Judd, A., Hovland, M., Dimitrov, L., Gil, S. G. & Jukes, V. (2002), 'The geological methane budget

at continental margins and its influence on climate change', *Geofluids* **2**(2), 109–126.

Kessler, J. D. & Leonte, M. (2015), 'Concentrations of gas dissolved in seawater and in gas bubbles collected in the northern gulf of mexico, april 12-20, 2015. distributed by Gulf of Mexico Research Initiative Information and Data Cooperative (GRIIDC), Harte Research Institute, Texas A&M University, Corpus Christi'.

Kessler, J. D., Valentine, D. L., Redmond, M. C., Du, M., Chan, E. W., Mendes, S. D., Quiroz, E. W., Villanueva, C. J., Shusta, S. S., Werra, L. M., Yvon-Lewis, S. A. & Weber, T. C. (2011), 'A persistent oxygen anomaly reveals the fate of spilled methane in the deep Gulf of Mexico', *Science* **331**(6015), 312–315.

King, M. B. (1969), *Phase Equilibrium in Mixtures*, International Series of Monographs in Chemical Engineering, Oxford, New York, Pergamon Press.

Larson, S. D. (1955), *Phase Studies of the Two Component Carbon Dioxide-Water System Involving the Carbon Dioxide Hydrate*, University of Illinois, Urbana.

Leifer, I. & Patro, R. K. (2002), 'The bubble mechanism for methane transport from the shallow sea bed to the surface: A review and sensitivity study', *Continental Shelf Research* **22**(16), 2409–2428.

Leonard, J. H. & Houghton, G. (1961), 'Effect of mass transfer on the velocity of rise of bubbles in water', *Nature* **190**, 687–688.

Leonte, M., Wang, B., Socolofsky, S. A., Mau, S., Breier, J. A. & Kessler, J. D. (2018), 'Using carbon isotope fractionation to constrain the extent of methane dissolution into the water column surrounding a natural hydrocarbon gas seep in the northern gulf of mexico.', *Geochemistry, Geophysics, Geosystems. (In review).* .

Little, J. C. & McGinnis, D. F. (2001), 'Hypolimnetic oxygenation: Predicting performance using a discrete-bubble model', *Water Science and Technology : Water Supply* **1**(4), 185–191.

MacDonald, I. R., Leifer, I., Sassen, R., Stine, P., Mitchell, R. & Guinasso, N. (2002), 'Transfer of hydrocarbons from natural seeps to the water column and atmosphere', *Geofluids* **2**(2), 95–107.

Maini, B. & Bishnoi, P. (1981), 'Experimental investigation of hydrate formation behaviour of

a natural gas bubble in a simulated deep sea environment', *Chemical Engineering Science* **36**(1), 183–189.

Maps, G. (2018), 'Gisr cruise map', https://www.google.com/maps. Accessed: 2018-10-05.

McCain, W. D. (1990), *The Properties of Petroleum Fluids*, PennWell Books, Tulsa, OK.

McGinnis, D. F., Lorke, A., Wuest, A., Stockli, A. & Little, J. C. (2004), 'Interaction between a bubble plume and the near field in a stratified lake', *Water Resources Research* **40**(10), W10206.

McGinnis, D. F., Wüest, D. F., Greinert, D. F., Artemov, D. F. & Beaubien, D. F. (2006), 'Fate of rising methane bubbles in stratified waters: How much methane reaches the atmosphere?', *Journal of Geophysical Research: Oceans* **111**(9), C09007–C09017.

Medwin, H. & Clay, C. S. (1998), *Fundamentals of acoustical oceanography*, Applications of modern acoustics, San Diego, CA : Academic Press.

Michelsen, M. L. & Mollerup, J. (1986), 'Partial derivatives of thermodynamic properties', *AIChE Journal* **32**(8), 1389–1392.

Milkov, A., Sassen, R., Novikova, I. & Mikhailov, E. (2000), 'Gas hydrates at minimum stability water depths in the gulf of mexico: Significance to geohazard assessment', *Transactions of the Gulf Coast Association of Geological Societies* **50**, 217–224.

Millero, F. J. & Poisson, A. (1981), 'International one-atmosphere equation of state of seawater', *Deep Sea Research Part A. Oceanographic Research Papers* **28**(6), 625–629.

Mohammadi, A. H., Anderson, R. & Tohidi, B. (2005), 'Carbon monoxide clathrate hydrates: Equilibrium data and thermodynamic modeling', *AIChE Journal* **51**(10), 2825–2833.

Mooijer-van den Heuvel, M., Witteman, R. & Peters, C. (2001), 'Phase behaviour of gas hydrates of carbon dioxide in the presence of tetrahydropyran, cyclobutanone, cyclohexane and methylcyclohexane', *Fluid Phase Equilibria* **182**, 97–110.

Morrison, T. J. & Billett, F. (1952), 'The salting-out of non-electrolytes. part II. the effect of variation in non-electrolyte', *Journal of the Chemical Society* pp. 3819–3822.

Motarjemi, M. & Jameson, G. J. (1978), 'Mass transfer from very small bubbles-the optimum bubble size for aeration', *Chemical Engineering Science* **33**(11), 1415–1423.

Natarajan, V., Bishnoi, P. R. & Kalogerakis, N. (1994), 'Induction phenomena in gas hydrate nucleation', *Chemical Engineering Science* **49**(13), 2075 – 2087.

Ng, H.-J. & Robinson, D. B. (1985), 'Hydrate formation in systems containing methane, ethane, propane, carbon dioxide or hydrogen sulfide in the presence of methanol', *Fluid Phase Equilibria* **21**(1), 145–155.

Ohgaki, K., Makihara, Y. & Takano, K. (1993), 'Formation of CO_2 hydrate in pure and sea waters', *Journal of Chemical Engineering of Japan* **26**, 558–564.

Okubo, A. (1971), 'Oceanic diffusion diagrams', *Deep Sea Research and Oceanographic Abstracts* **18**(8), 789 – 802.

Parkes, R. J., Cragg, B. A., Fry, J. C., Herbert, R. A., Wimpenny, J. W. T., Allen, J. A. & Whitfield, M. (1990), 'Bacterial biomass and activity in deep sediment layers from the peru margin.', *Philosophical Transactions of the Royal Society of London. Series A, Mathematical and Physical Sciences* **A331**(1616), 139–153.

Pedersen, K. S., Christensen, P. L. & Shaikh, J. A. (2015), *Phase Behavior of Petroleum Reservoir Fluids*, 2nd edition edn, CRC Press, Taylor & Francis Group, New York.

Peebles, F. N. & Garber, H. J. (1953), 'Studies on the motion of gas bubbles in liquids', *Chemical Engineering Progress* **49**, 88–97.

Peng, D.-Y. & Robinson, D. B. (1976), 'A new two-constant equation of state', *Industrial & Engineering Chemistry Fundamentals* **15**(1), 59–64.

Pilson, M. E. Q. (2013), *Introduction to the Chemistry of the Sea*, 2nd edn, Cambridge University Press.

Poling, B. E., Prausnitz, J. M. & O'Connell, J. P. (2001), *The Properties of Gases and Liquids*, McGraw-Hill, New York, NY.

Reddy, C. M., Arey, J. S., Seewald, J. S., Sylva, S. P., Lemkau, K. L., Nelson, R. K., Carmichael, C. A., McIntyre, C. P., Fenwick, J., Ventura, G. T., Van Mooy, B. A. S. & Camilli, R. (2012), 'Composition and fate of gas and oil released to the water column during the deepwater horizon oil spill', *Proceedings of the National Academy of Sciences* **109**(50), 20229–20234.

Rehder, G., Brewer, P. W., Peltzer, E. T. & Friederich, G. (2002), 'Enhanced lifetime of methane bubble streams within the deep ocean', *Geophysical Research Letters* **29**(15), 21–1–21–4.

Rehder, G., Leifer, I., Brewer, P. G., Friederich, G. & Peltzer, E. T. (2009), 'Controls on methane bubble dissolution inside and outside the hydrate stability field from open ocean field experiments and numerical modeling', *Marine Chemistry* **114**(1-2), 19–30.

Rettich, T. R., Handa, Y. P., Battino, R. & Wilhelm, E. (1981), 'Solubility of gases in liquids. 13. High-precision determination of Henry's constants for methane and ethane in liquid water at 275 to 328 k', *Journal of Physical Chemistry* **85**(22), 3230–3237.

Richard, C., Christopher M., R., Dana R., Y., Benjamin A. S. Van, M., Michael V., J., James C., K., Cameron P., M., Sean P., S. & James V., M. (2010), 'Tracking hydrocarbon plume transport and biodegradation at deepwater horizon', *Science* **330**, 201–204.

Robinson, D. B. & Peng, D. Y. (1978), *The Characterization of the Heptanes and Heavier Fractions for the GPA Peng-Robinson Programs*, Research report (Gas Processors Association), Gas Processors Association.

Römer, M., Sahling, H., Pape, T., Bohrmann, G. & Spieß, V. (2012), 'Quantification of gas bubble emissions from submarine hydrocarbon seeps at the Makran continental margin (offshore Pakistan)', *Journal of Geophysical Research: Oceans* **117**(C10), C10015.

Ruppel, C. D. (2011), 'Methane hydrates and contemporary climate change', *Nature Education Knowledge* **3**(10).

Ruppel, C. D. & Kessler, J. D. (2017), 'The interaction of climate change and methane hydrates', *Reviews of Geophysics* **55**(1), 126–168.

Ryerson, T. B., Aikin, K. C., Angevine, W. M., Atlas, E. L., Blake, D. R., Brock, C. A., Fehsenfeld, F. C., Gao, R.-S., Gouw, J. A. d., Fahey, D. W., Holloway, J. S., Lack, D. A., Lueb, R. A., Meinardi, S., Middlebrook, A. M., Murphy, D. M., Neuman, J. A., Nowak, J. B., Parrish, D. D., Peischl, J., Perring, A. E., Pollack, I. B., Ravishankara, A. R., Roberts, J. M., Schwarz, J. P., Spackman, J. R., Stark, H., Warneke, C. & Watts, L. A. (2011), 'Atmospheric emissions from the Deepwater Horizon spill constrain air-water partitioning, hydrocarbon fate, and leak rate',

Geophysical Research Letters **38**, L07803.

Ryerson, T. B., Camilli, R., Kessler, J. D., Kujawinski, E. B., Reddy, C. M., Valentine, D. L., Atlas, E., Blake, D. R., de Gouw, J., Meinardi, S., Parrish, D. D., Peischl, J., Seewald, J. S. & Warneke, C. (2012), 'Chemical data quantify Deepwater Horizon hydrocarbon flow rate and environmental distribution', *Proceedings of the National Academy of Sciences* .

Sarmiento, J. L. & Gruber, N. (2006), *Ocean biogeochemical dynamics.*, Princeton, New Jersey : Princeton University Press.

Sassen, R. & Macdonald, I. R. (1997), 'Hydrocarbons of experimental and natural gas hydrates, gulf of mexico continental slope', *Organic Geochemistry* **26**(3), 289 – 293.

Schoell, M. (1980), 'The hydrogen and carbon isotopic composition of methane from natural gases of various origins', **44**, 649–661.

Schwarzenbach, R., Gschwend, P. M. & Imboden, D. M. (2003), *Environmental Organic Chemistry*, Hoboken, NJ: Wiley.

Sharqawy, M. H., V., J. H. L. & Zubair, S. M. (2010), 'Thermophysical properties of seawater: a review of existing correlations and data', *Desalination and Water Treatment* **16**, 354–380.

Singleton, V. L. & Little, J. C. (2006), 'Designing hypolimnetic aeration and oxygenation systems - a review', *Environmental Science & Technology* **40**(24), 7512–7520.

Sloan, E. D. & Koh, C. (2008), *Clathrate Hydrates of Natural Gases*, CRC Press, Boca Raton, FL.

Socolofsky, S. A. (2015*a*), 'High-definition videos of natural gas seeps observed at the seafloor and in the water column on GISR Cruise G07 at GC 600 and MC 118 in July 2014. distributed by: Gulf of Mexico Research Initiative Information and Data Cooperative (GRIIDC), Harte Research Institute, Texas A&M University, Corpus Christi'.

Socolofsky, S. A. (2015*b*), 'Stereoscopic high-speed high-resolution camera images of natural gas seeps observed at the seafloor and in the water column on GISR Cruise G07 at GC 600 and MC 118 in July 2014. distributed by: Gulf of Mexico Research Initiative Information and Data Cooperative (GRIIDC), Harte Research Institute, Texas A&M University, Corpus Christi'.

Socolofsky, S. A. (2016*a*), 'Underway data from the E/V Nautilus Cruise NA046 Conducted 16-

26 July 2014 in the Northern Gulf of Mexico. distributed by Gulf of Mexico Research Initiative Information and Data Cooperative (GRIIDC), Harte Research Institute, Texas A&M University, Corpus Christi'.

Socolofsky, S. A. (2016*b*), 'Underway data from the EV Nautilus Cruise NA056 Conducted 09-21 April 2015 in the Northern Gulf of Mexico. distributed by Gulf of Mexico Research Initiative Information and Data Cooperative (GRIIDC), Harte Research Institute, Texas A&M University, Corpus Christi'.

Socolofsky, S. A., Adams, E. E. & Sherwood, C. R. (2011), 'Formation dynamics of subsurface hydrocarbon intrusions following the Deepwater Horizon blowout', *Geophysical Research Letters* **38**, L09602.

Socolofsky, S. A., Dissanayake, A. L., Jun, I., Gros, J., Arey, S. & Reddy, C. M. (2015), 'Texas a&m oilspill calculator (TAMOC): Modeling suite for subsea spills', *the 38th Arctic and Marine Oilspill Program (AMOP) Technical Seminar on Environmental Contamination and Response* .

Spier, C., Stringfellow, W. T., Hazen, T. C. & Conrad, M. (2013), 'Distribution of hydrocarbons released during the 2010 MC 252 oil spill in deep offshore waters', *Environmental Pollution* **173**, 224–230.

Sun, X., Sun, B., Wang, Z., Chen, L. & Gao, Y. (2017), 'A new model for hydrodynamics and mass transfer of hydrated bubble rising in deep water', *Chemical Engineering Science* **173**, 168 – 178.

Topham, D. (1984), 'Formation of gas hydrates on bubbles of hydrocarbon gases rising in seawater', *Chemical Engineering Science* **39**(5), 821–828.

Valentine, D. L. (2002), 'Biogeochemistry and microbial ecology of methane oxidation in anoxic environments: a review.', *Antonie van Leeuwenhoek: International journal of general and molecular microbiology* **81**(1-4), 271 – 282.

Vasconcelos, J. M. T., Orvalho, S. P. & Alves, S. S. (2002), 'Gas-liquid mass transfer to single bubbles: Effect of surface contamination', *AIChE Journal* **48**(6), 1145–1154.

Von Bogdandy, L., Rutsch, W. & Stranski, I. N. (1959), 'Gasaustausch zwischen blasen und

gaslösenden flüssigkeiten', *Chemie Ingenieur Technik (CIT)* **31**(9), 580.

Wang, B. & Socolofsky, S. A. (2015), 'A deep-sea, high-speed, stereoscopic imaging system for in situ measurement of natural seep bubble and droplet characteristics', *Deep-Sea Research Part I: Oceanographic Research Papers* **104**, 134–148.

Wang, B., Socolofsky, S. A., Breier, J. A. & Seewald, J. (2016), 'Observations of bubbles in natural seep flares at MC 118 and GC 600 using *in situ* quantitative imaging', *Journal of Geophysical Research: Oceans* **121**(4), 2203–2230.

Warzinski, R. P., Lynn, R., Haljasmaa, I., Leifer, I., Shaffer, F., Anderson, B. J. & Levine, J. S. (2014), 'Dynamic morphology of gas hydrate on a methane bubble in water: Observations and new insights for hydrate film models', *Geophysical Research Letters* **41**(19), 6841–6847.

Weber, T., Mayer, L., Jerram, K., Beaudoin, J., Rzhanov, Y. & Lovalvo, D. (2014), 'Acoustic estimates of methane gas flux from the seabed in a 6000 km^2 region in the northern gulf of mexico', *Geochemistry, Geophysics, Geosystems* **15**(5), 1911–1925.

Wüest, A., Brooks, N. H. & Imboden, D. M. (1992), 'Bubble plume modeling for lake restoration', *Water Resources Research* **28**(12), 3235–3250.

Yamamoto, S., Alcauskas, J. B. & Crozier, T. E. (1976), 'Solubility of methane in distilled water and seawater', *Journal of Chemical and Engineering Data* **21**(1), 78–80.

Yapa, P. D. & Fanghui, C. (2004), 'Behavior of oil and gas from deepwater blowouts.', *Journal of Hydraulic Engineering* **130**(6), 540 – 553.

Yapa, P. D., Zheng, L. & Nakata, K. (1999), 'Modeling underwater oil/gas jets and plumes.', *Journal of Hydraulic Engineering* **125**(5), 481 – 491.

Yapa, P. & Zheng, L. (1997), 'Simulation of oil spills from underwater accidents .1. model development.', *Journal of Hydraulic Research* **35**(5), 673 – 687.

Yarym-Agaev, N. L., Sinyavskaya, R. P., Koliushko, I. I. & Levinton, L. Y. (1985), 'Phase equilibria in the water-methane and methanol-methane binary systems under high pressures', *Journal of applied chemistry of the USSR* **58**(1), 154–157.

Zhang, Y. (2003), 'Methane escape from gas hydrate systems in marine environment, and methane-

driven oceanic eruptions', *Geophysical Research Letters* **30**(7), 51–1–51–4.

Zhao, L., Boufadel, M. C., Adams, E., Socolofsky, S. A., King, T., Lee, K. & NedwedâĂŃ, T. (2016), 'Simulation of scenarios of oil droplet formation from the Deepwater Horizon blowout', *Marine Pollution Bulletin* **101**, 304–319.

Zheng, L. & Yapa, P. D. (2000), 'Buoyant velocity of spherical and nonspherical bubbles/droplets', *Journal of Hydraulic Engineering* **126**(11), 852–854.

Zheng, L. & Yapa, P. D. (2002), 'Modeling gas dissolution in deepwater oil/gas spills.', *Journal of Marine Systems* **31**, 299 – 309.

APPENDIX A

ACOUSTIC MEASUREMENTS OF TRAJECTORY OF BUBBLES FROM GISR CRUISE

A.1 Trajectory of Bubbles in G08 Cruise

Table A.1 shows the measurement time information of acoustic surveys using the Kongsberg EM 302 in G08 cruise. GISR carried out 61 acoustic surveys at the Sleeping Dragon vent site between April 10 and April 19 in 2015 during the G08 cruise, and the average measurement time is about 30 minutes for each survey.

Table A.1: The measurement time information of acoustic surveys in G08 cruise.

Shiptracking	Beginning of Measurement		End of Measurement	
	Date	Time	Date	Time
1	20150410	16:27:57	20150410	16:55:54
2	20150410	16:59:51	20150410	17:24:21
3	20150410	17:34:32	20150410	18:03:28
4	20150411	06:40:39	20150411	07:17:17
5	20150411	07:25:42	20150411	07:58:19
6	20150411	08:08:04	20150411	08:37:57
7	20150411	08:46:39	20150411	09:05:12
8	20150411	09:10:55	20150411	09:23:48
9	20150411	09:31:15	20150411	09:46:34
10	20150411	09:51:45	20150411	10:07:26
11	20150411	10:13:32	20150411	10:30:41
12	20150411	10:34:39	20150411	11:30:21
13	20150411	11:36:54	20150411	11:56:25
14	20150411	13:30:01	20150411	13:51:09
15	20150411	13:55:24	20150411	14:19:04
16	20150411	14:21:04	20150411	14:47:48
17	20150411	14:53:32	20150411	15:02:49
18	20150411	15:19:22	20150411	15:48:39
19	20150413	05:59:46	20150413	06:30:41
20	20150413	06:41:29	20150413	07:14:08
21	20150413	07:25:36	20150413	07:58:21
22	20150413	08:08:11	20150413	08:34:30
23	20150413	08:42:38	20150413	09:05:38
24	20150413	09:12:43	20150413	09:38:01
25	20150413	09:41:55	20150413	10:02:48
26	20150413	10:10:30	20150413	10:35:27
27	20150413	10:46:39	20150413	11:03:22

Continued on next page

Table A.1: Continued

Shiptracking	Beginning of Measurement		End of Measurement	
	Date	Time	Date	Time
28	20150413	11:10:11	20150413	11:35:37
29	20150413	11:47:18	20150413	12:22:56
30	20150414	01:30:01	20150414	01:52:59
31	20150414	02:00:26	20150414	02:22:19
32	20150414	02:25:05	20150414	02:48:26
33	20150414	02:51:12	20150414	03:23:19
34	20150414	03:24:23	20150414	03:52:35
35	20150414	03:59:09	20150414	04:55:28
36	20150414	08:03:54	20150414	08:36:15
37	20150414	08:47:55	20150414	09:17:51
38	20150414	09:27:34	20150414	09:53:23
39	20150414	10:08:49	20150414	10:33:03
40	20150414	10:43:06	20150414	11:07:56
41	20150414	11:18:10	20150414	11:43:16
42	20150414	11:53:31	20150414	12:34:58
43	20150415	11:57:49	20150416	02:44:54
44	20150416	02:49:36	20150416	03:25:59
45	20150416	03:32:16	20150416	03:56:34
46	20150416	04:01:02	20150416	04:46:11
47	20150416	05:54:38	20150416	06:21:29
48	20150416	06:26:53	20150416	06:50:41
49	20150416	10:36:05	20150416	12:05:41
50	20150416	12:19:57	20150416	13:00:58
51	20150416	13:13:58	20150416	13:43:33
52	20150418	05:06:31	20150418	05:36:08
53	20150418	05:47:26	20150418	06:09:18
54	20150418	06:19:25	20150418	06:41:17
55	20150418	06:51:56	20150418	08:35:18
56	20150419	01:38:07	20150419	02:53:28
57	20150419	03:04:49	20150419	04:06:42
58	20150419	04:15:53	20150419	05:20:31
59	20150419	05:29:18	20150419	06:37:11
60	20150419	06:40:42	20150419	10:43:51
61	20150419	11:17:48	20150419	12:27:53

The data handling procedures for acoustic anomalies are listed below.

- Plot the processed acoustic anomalies from EM 302 (Total 61 Cases).
- Extract the main trajectory of bubbles from the source point ($|x_0|$ < 100 m and $|y_0|$ < 100 m).
- Categorize all cases based on the measurement time and the shape of trajectory (16 cases).

A.1.1 Processed Acoustic Anomalies

Figure A.1 shows the measured acoustic anomalies at the MC 118 site during the G08 cruise. We extract the water column backscatter data using the Fledermaus, the multi-beam processing software package by Kongsberg. In the raw data file, the coordinate of the position of bubbles is latitude, longitude, and elevation. These data include bubble streams emanating from the other seafloor seeps nearby the Sleeping Dragon vent at the MC 118 site.

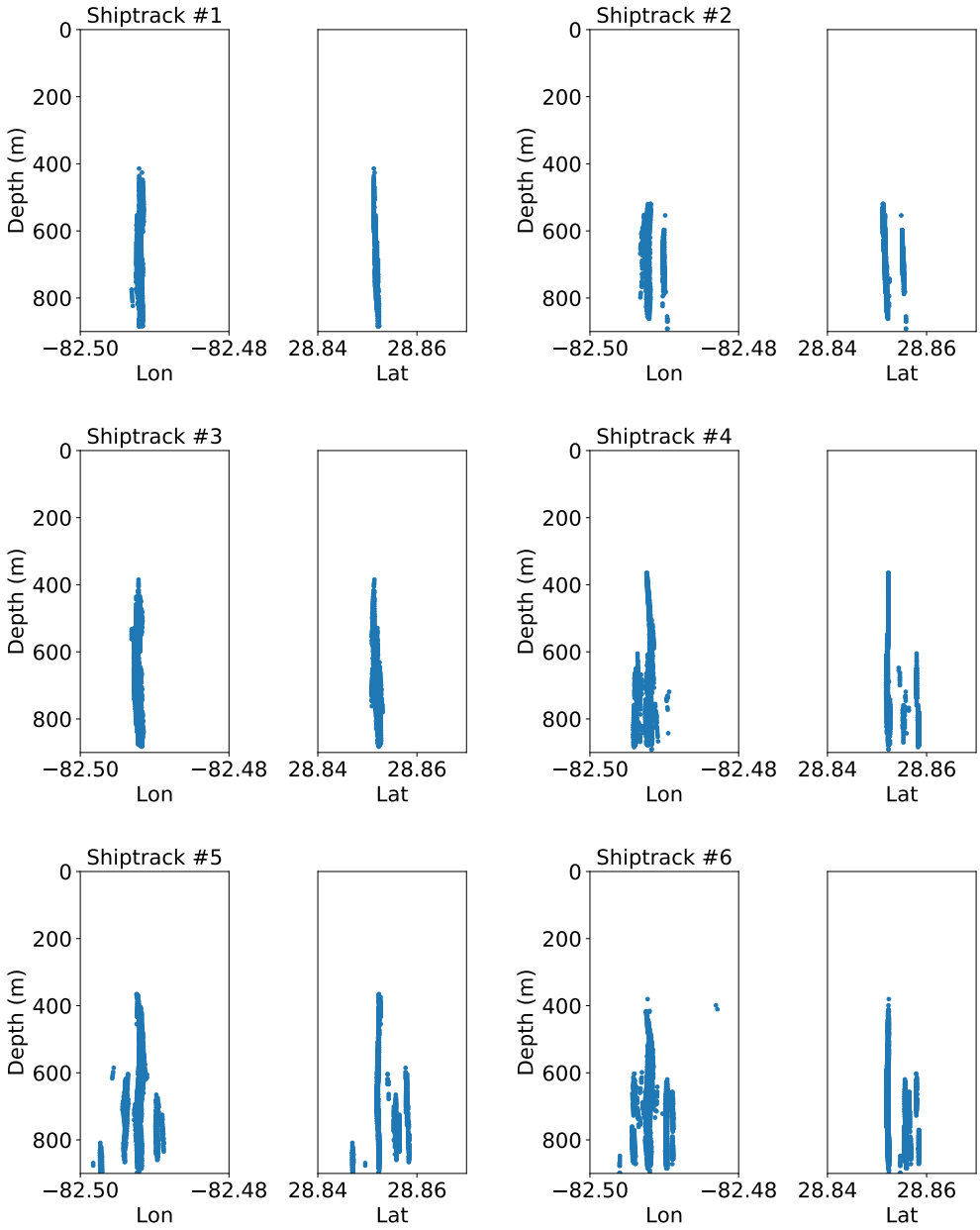

Figure A.1: Acoustic anomalies measured by EM 302 at MC 118 site during G08 cruise.

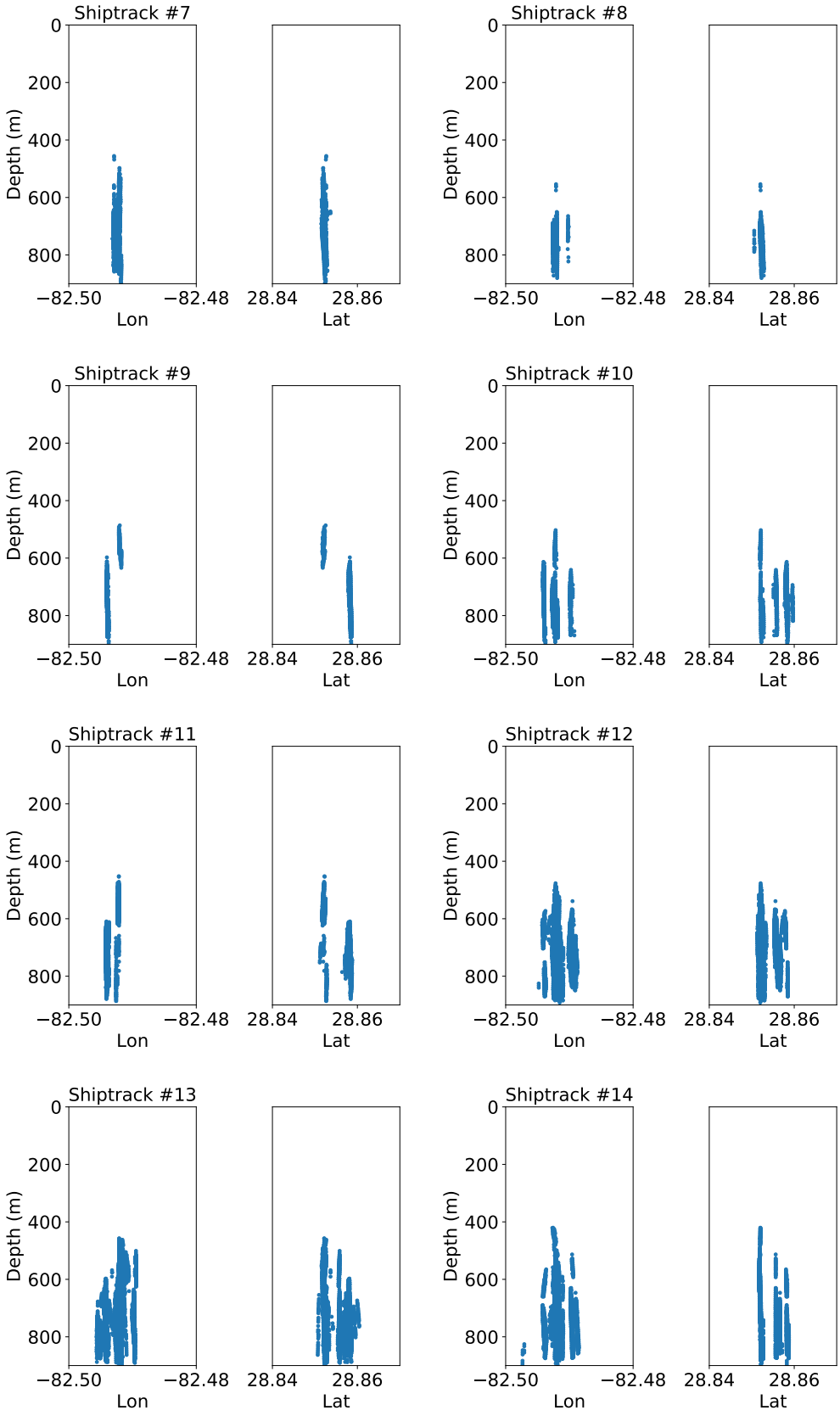

Figure A.1: Continued

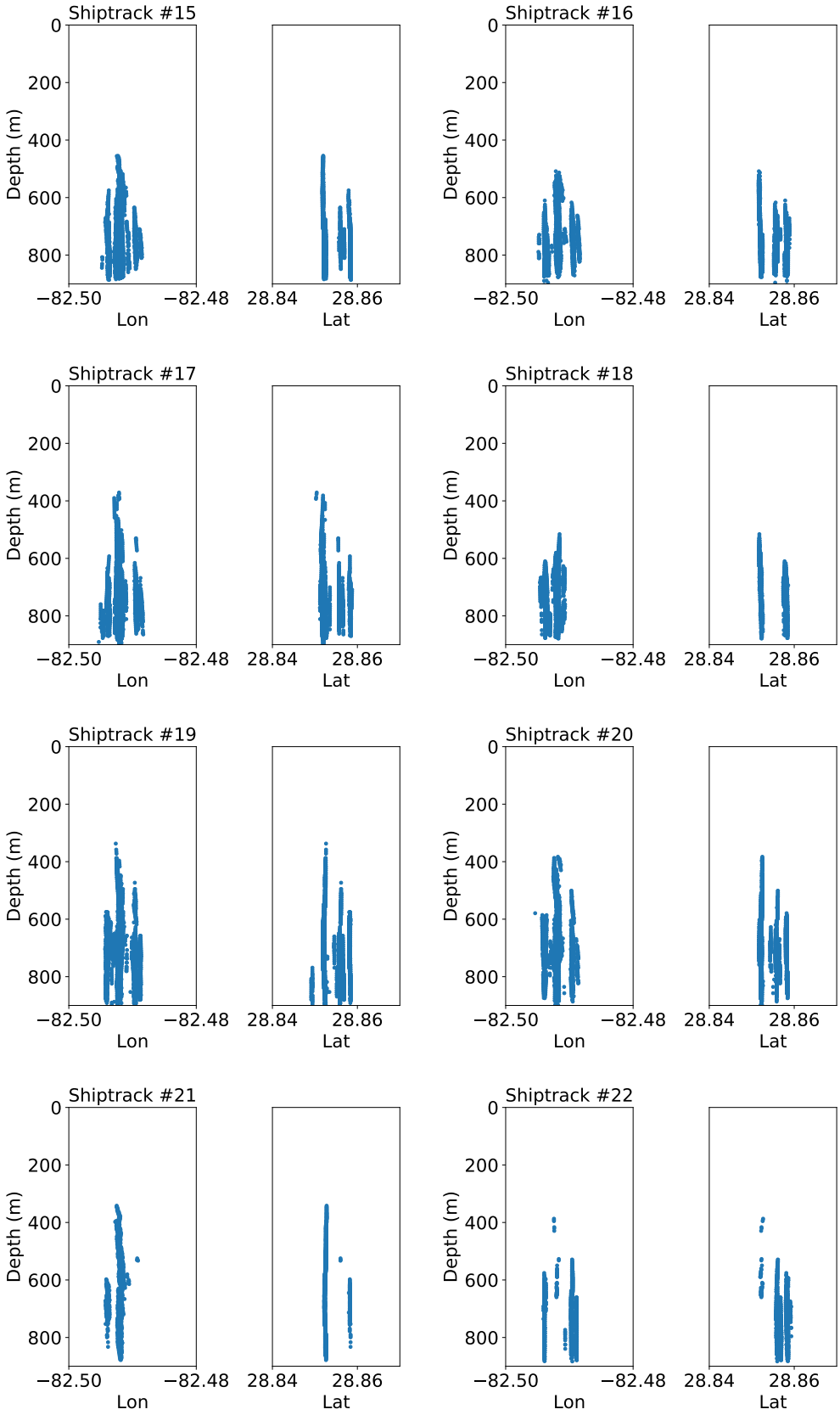

Figure A.1: Continued

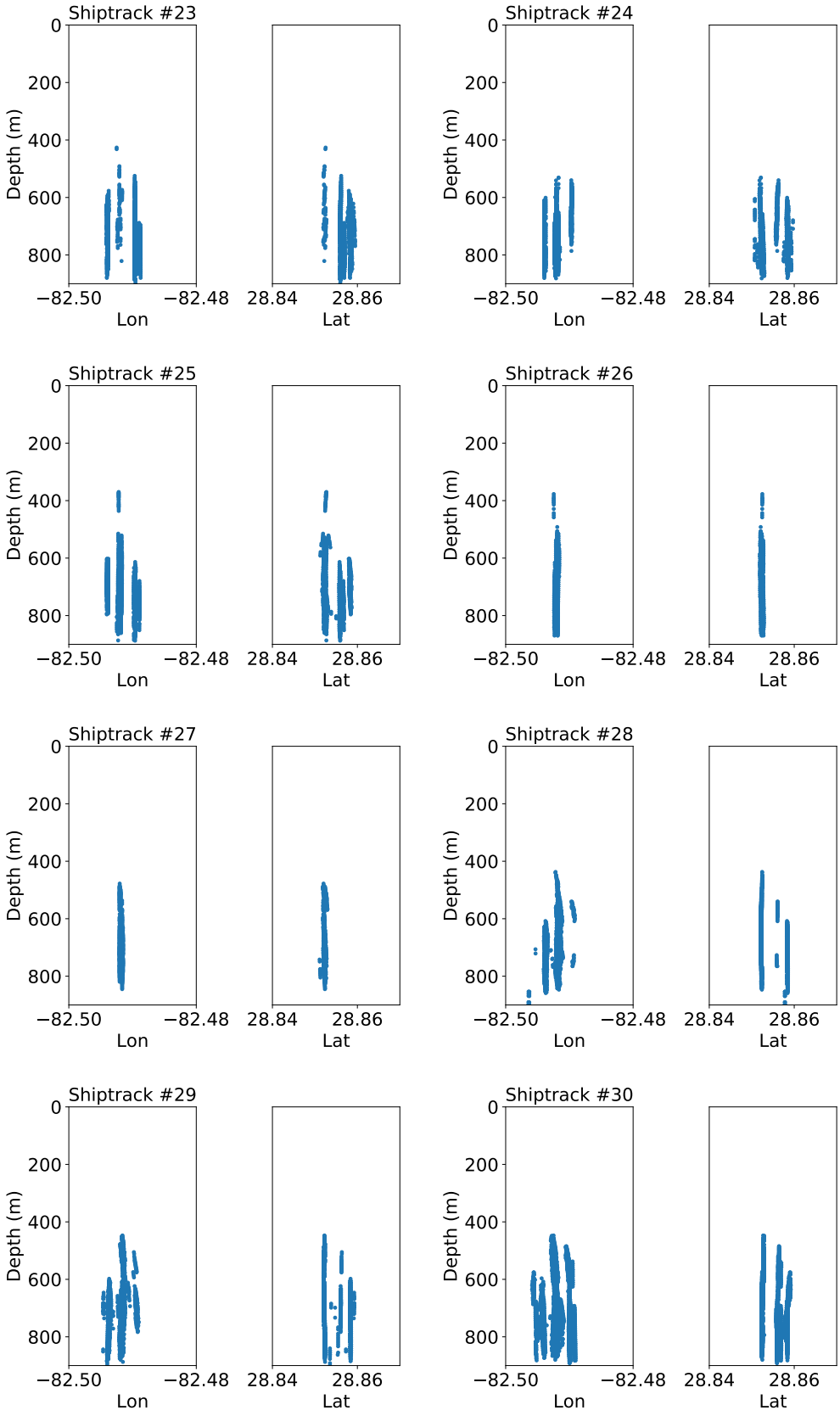

Figure A.1: Continued

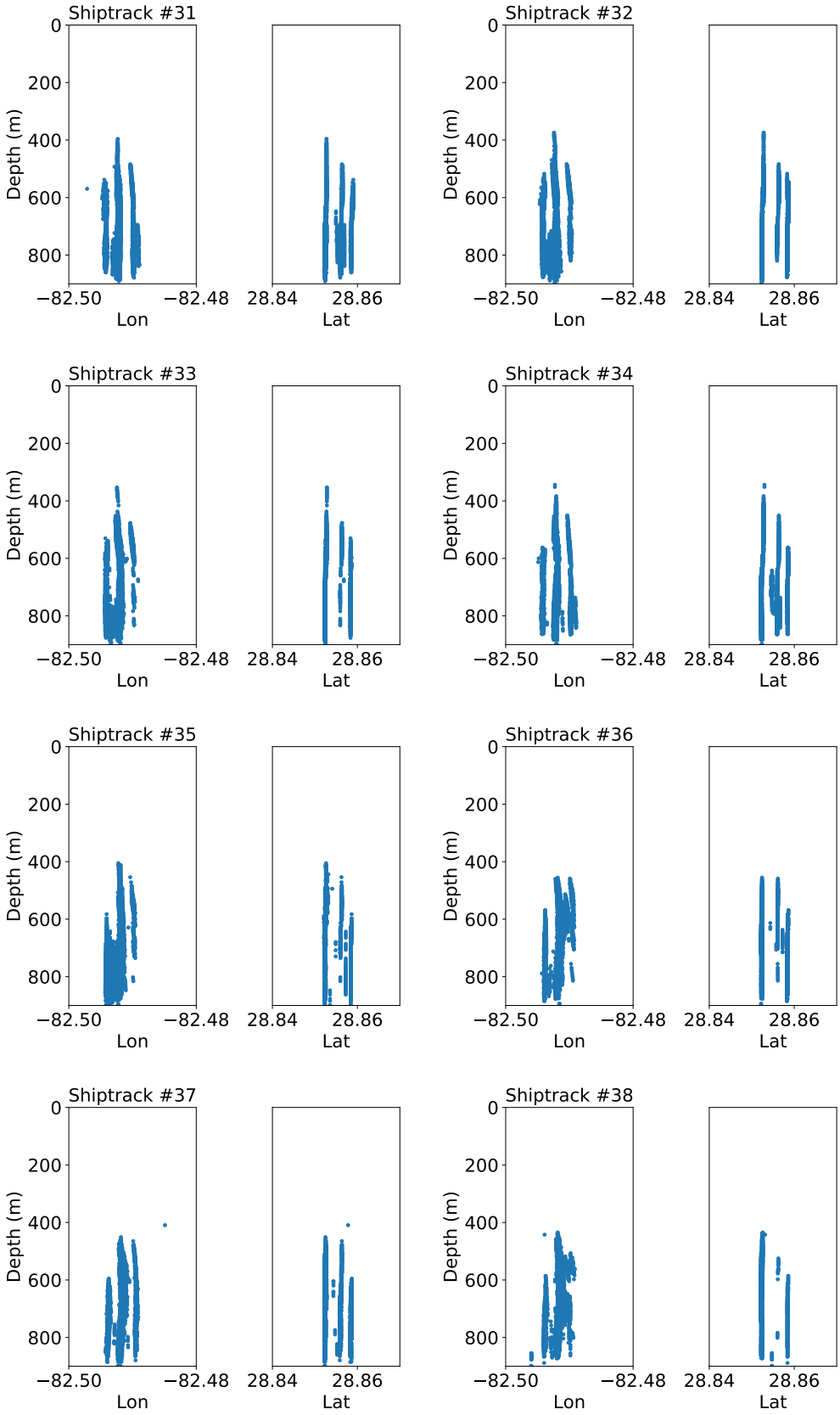

Figure A.1: Continued

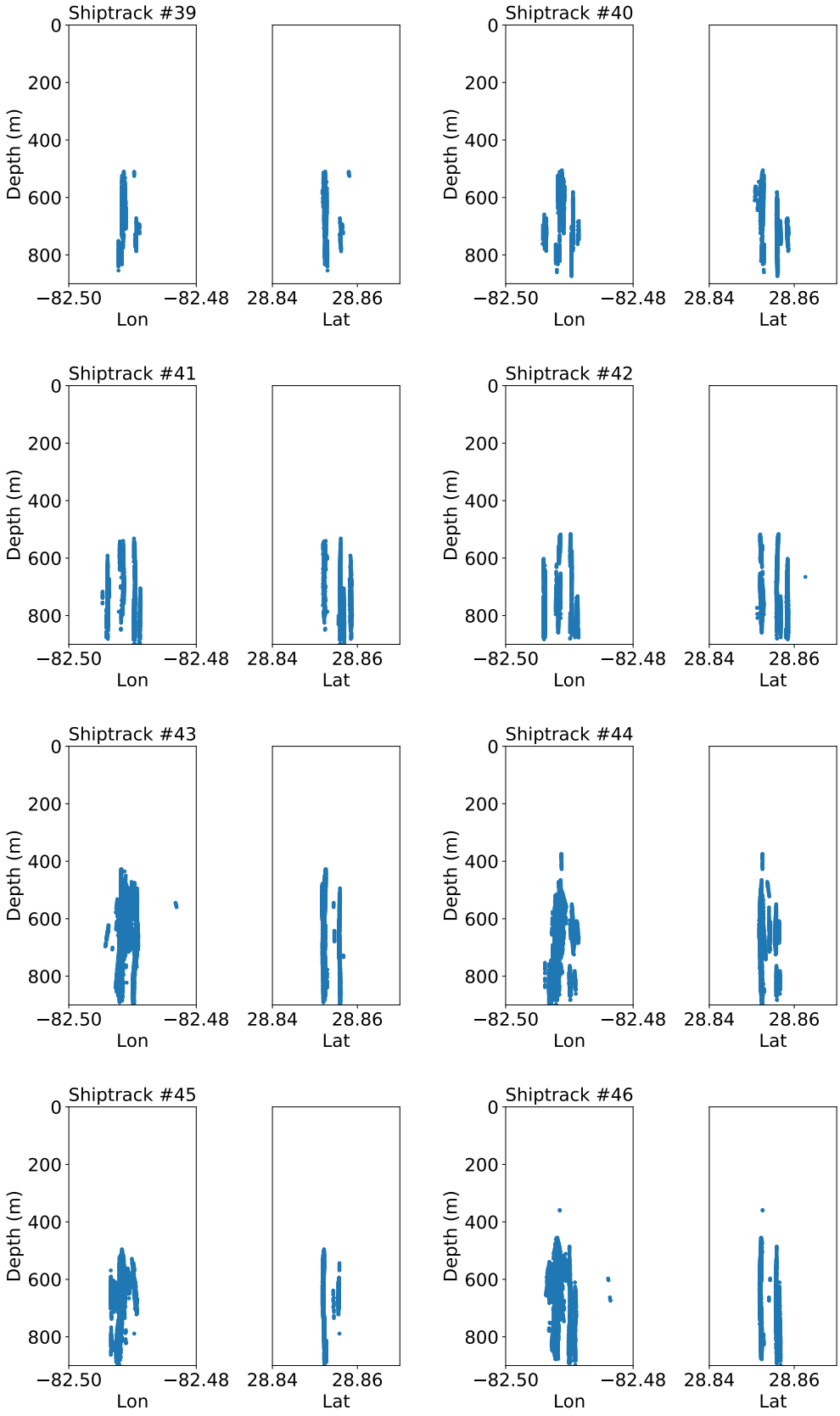

Figure A.1: Continued

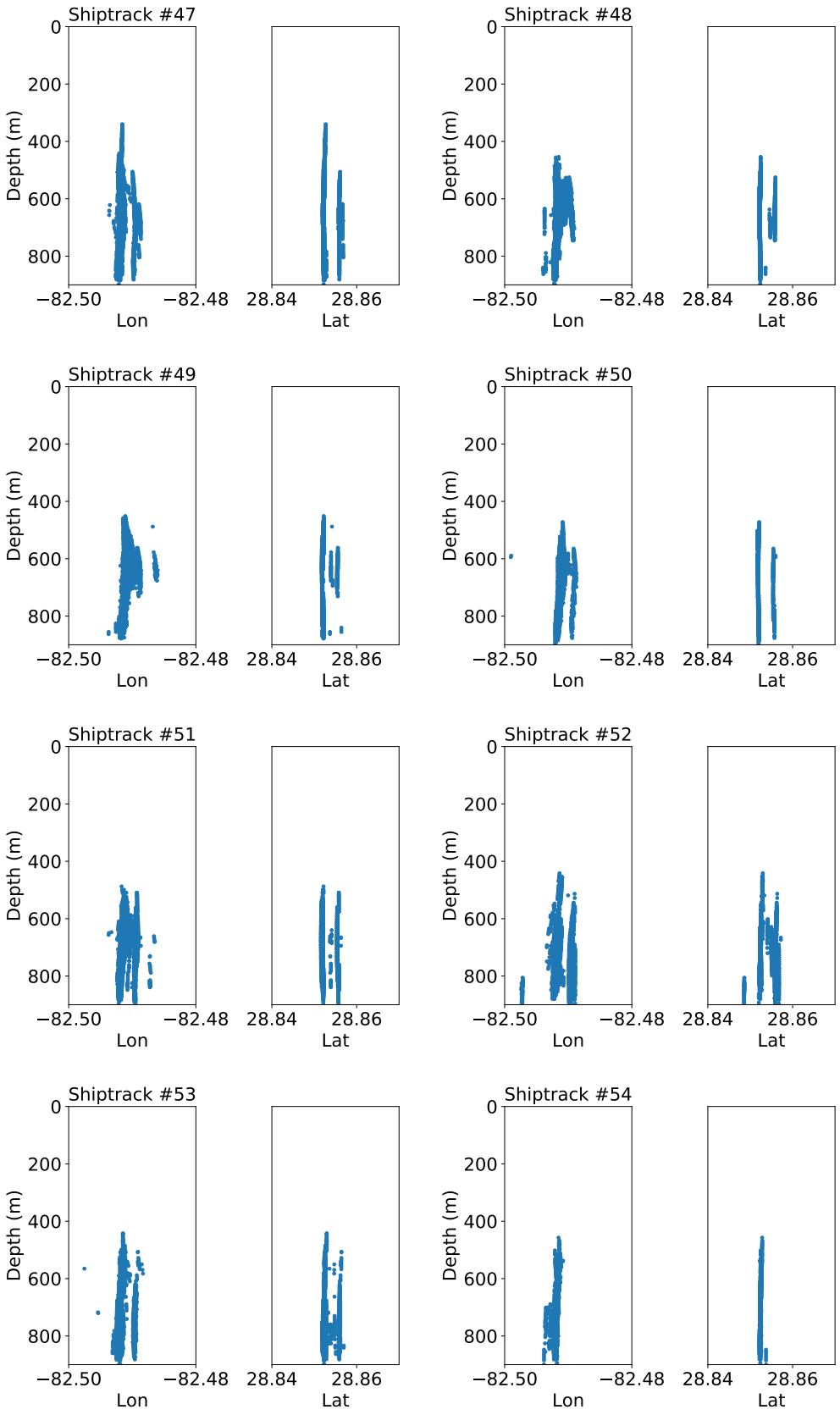

Figure A.1: Continued

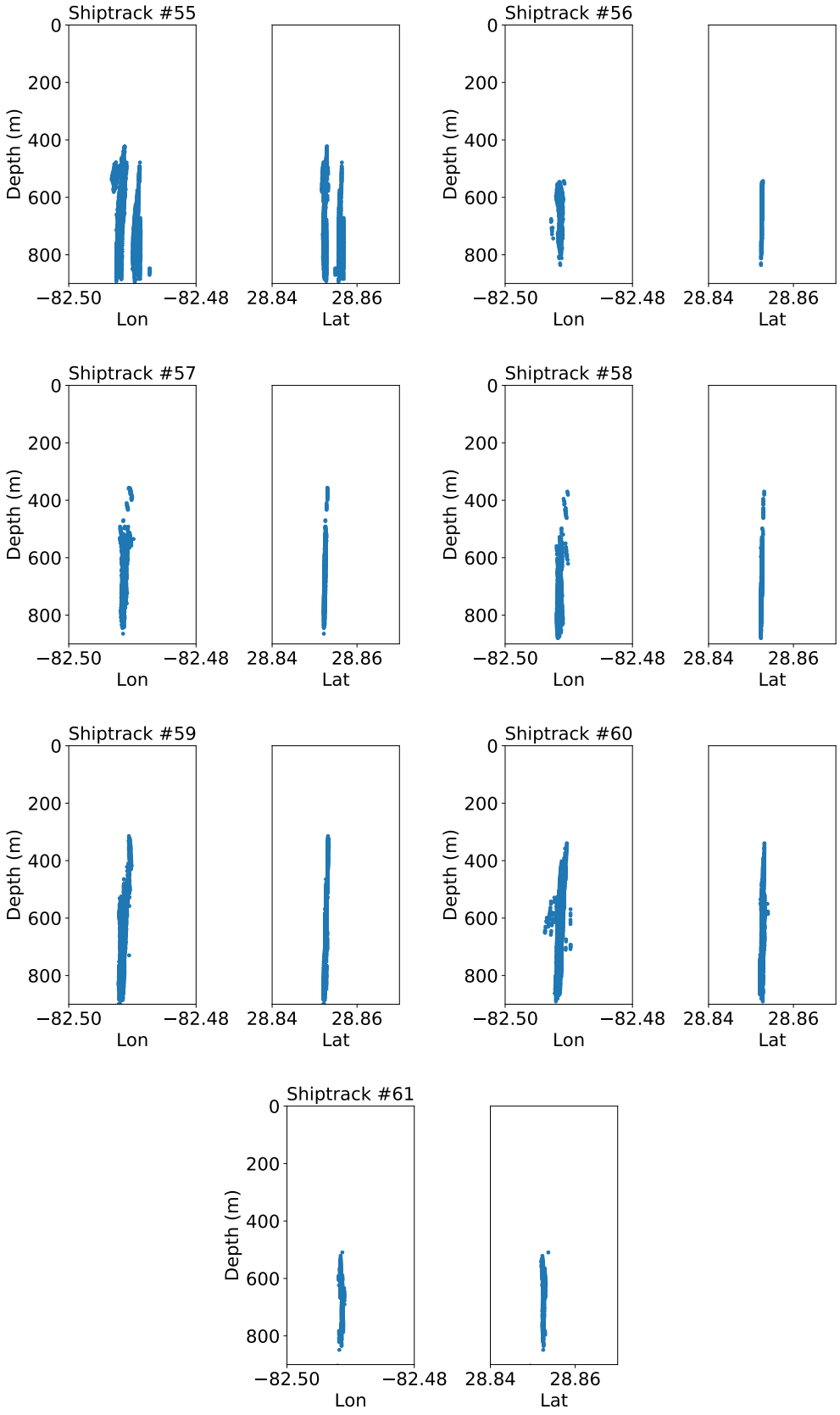

Figure A.1: Continued

A.1.2 Main Trajectories of Seep Bubbles

We convert the coordinate system of bubble position from the longitude/latitude to the x/y. Then, we extract the main bubble streams from the Sleeping Dragon vents based on the position of bubbles. If the bubbles apart from the source points (x_0 and y_0) more than 100 m of distance, then we remove the data points from the figure. Figure A.2 shows the main trajectories of bubbles from the Sleeping Dragon vent in the x-y coordinate system during the G08 cruise.

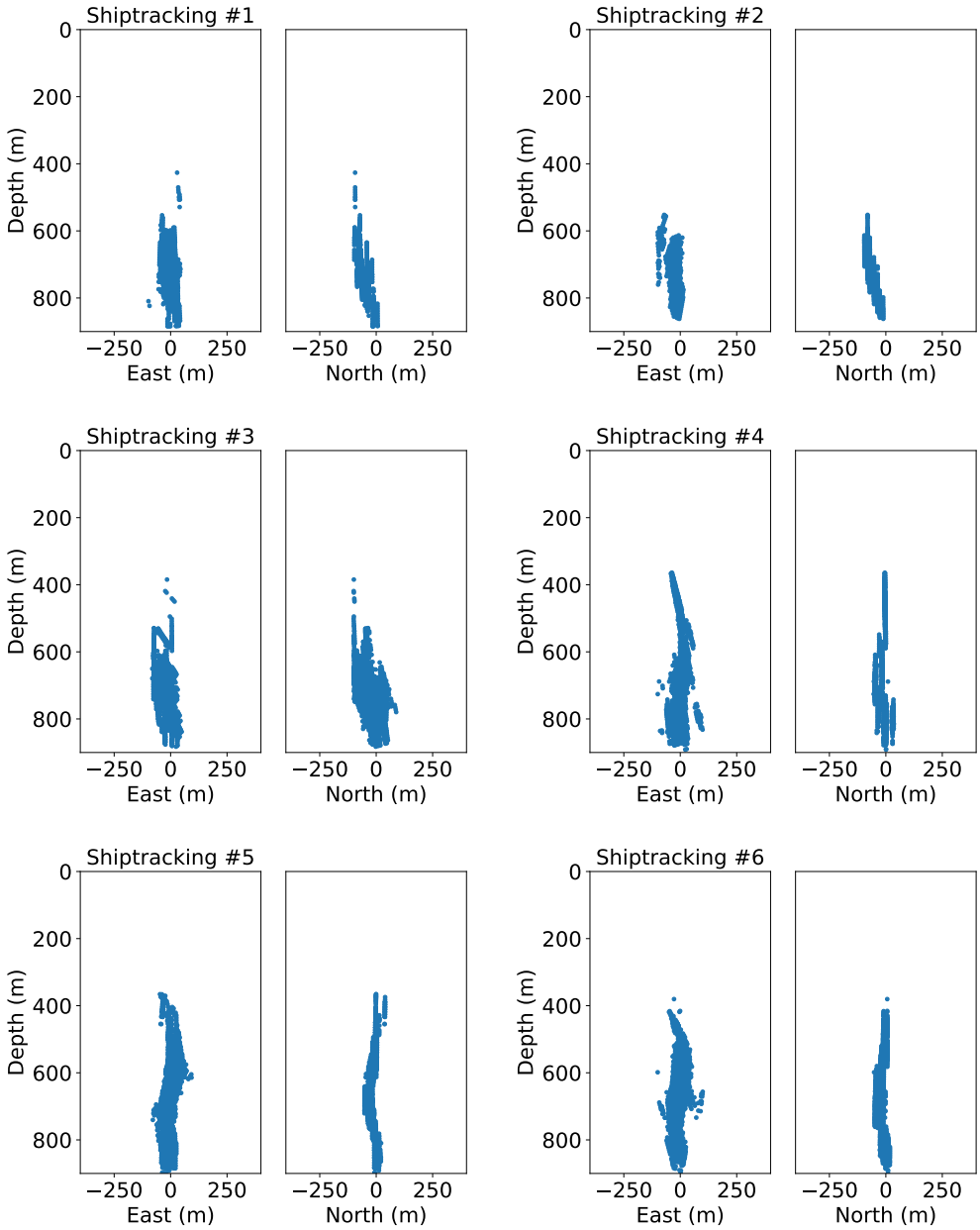

Figure A.2: Main trajectories of bubbles emanating from the Sleeping Dragon vent during G08 cruise.

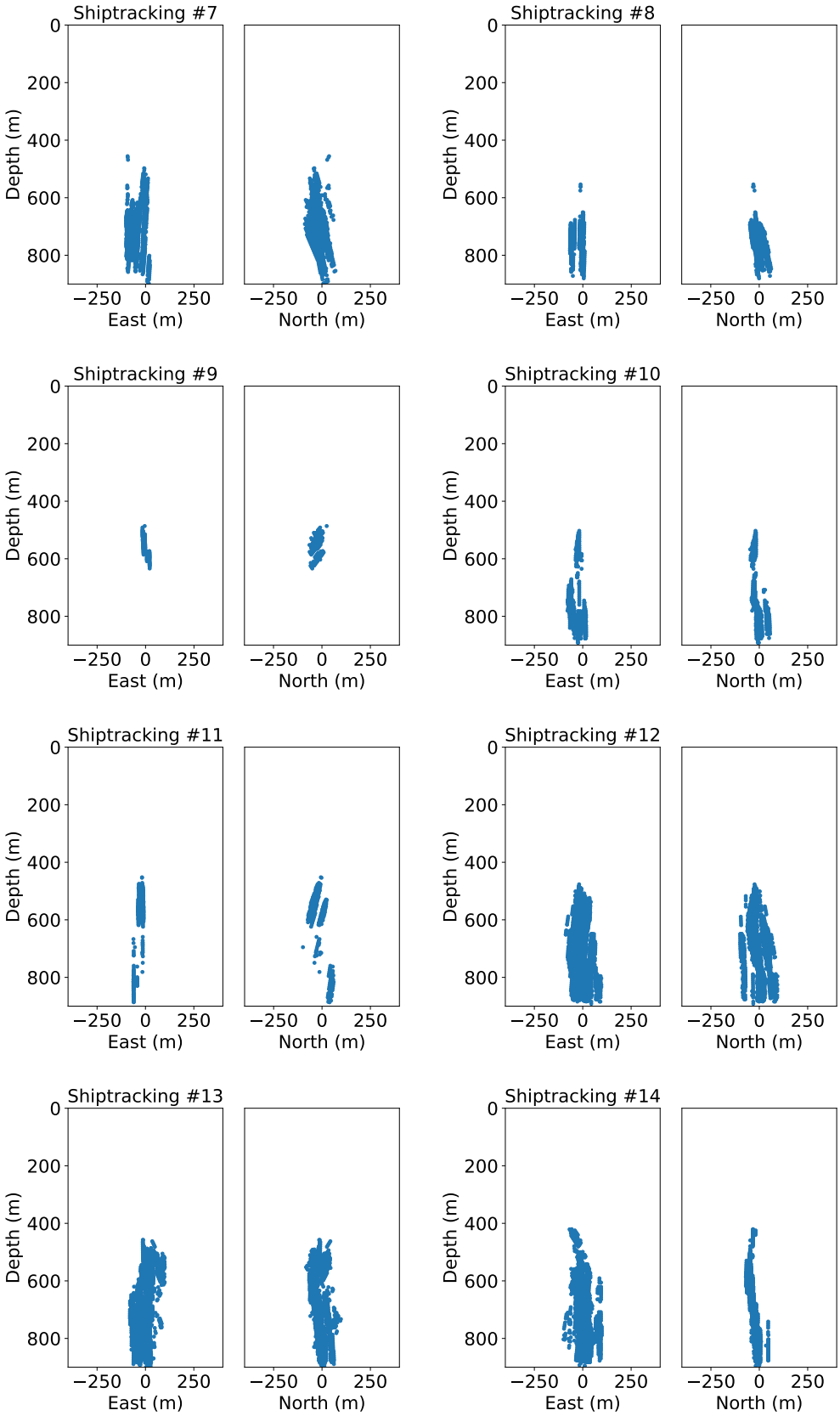

Figure A.2: Continued

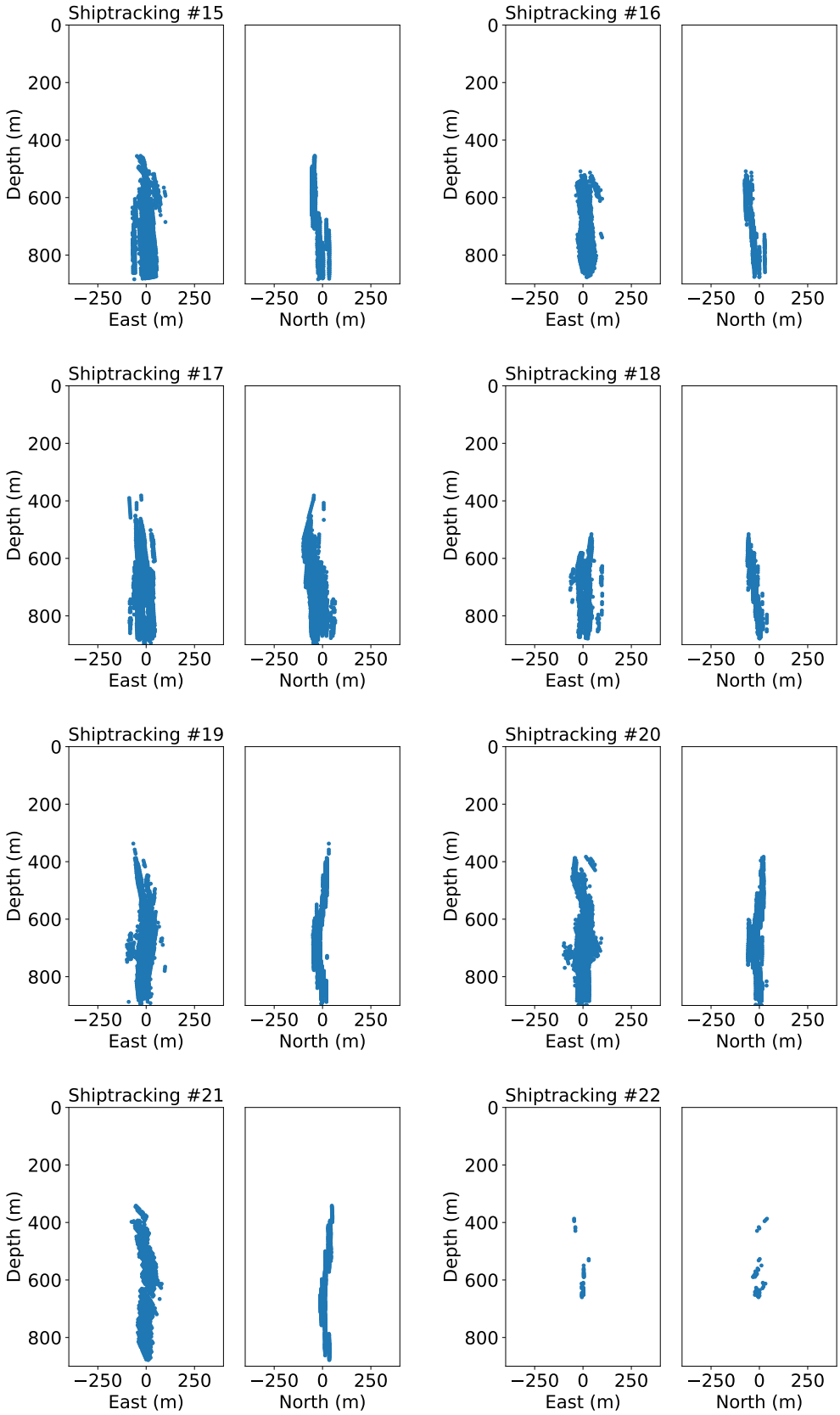

Figure A.2: Continued

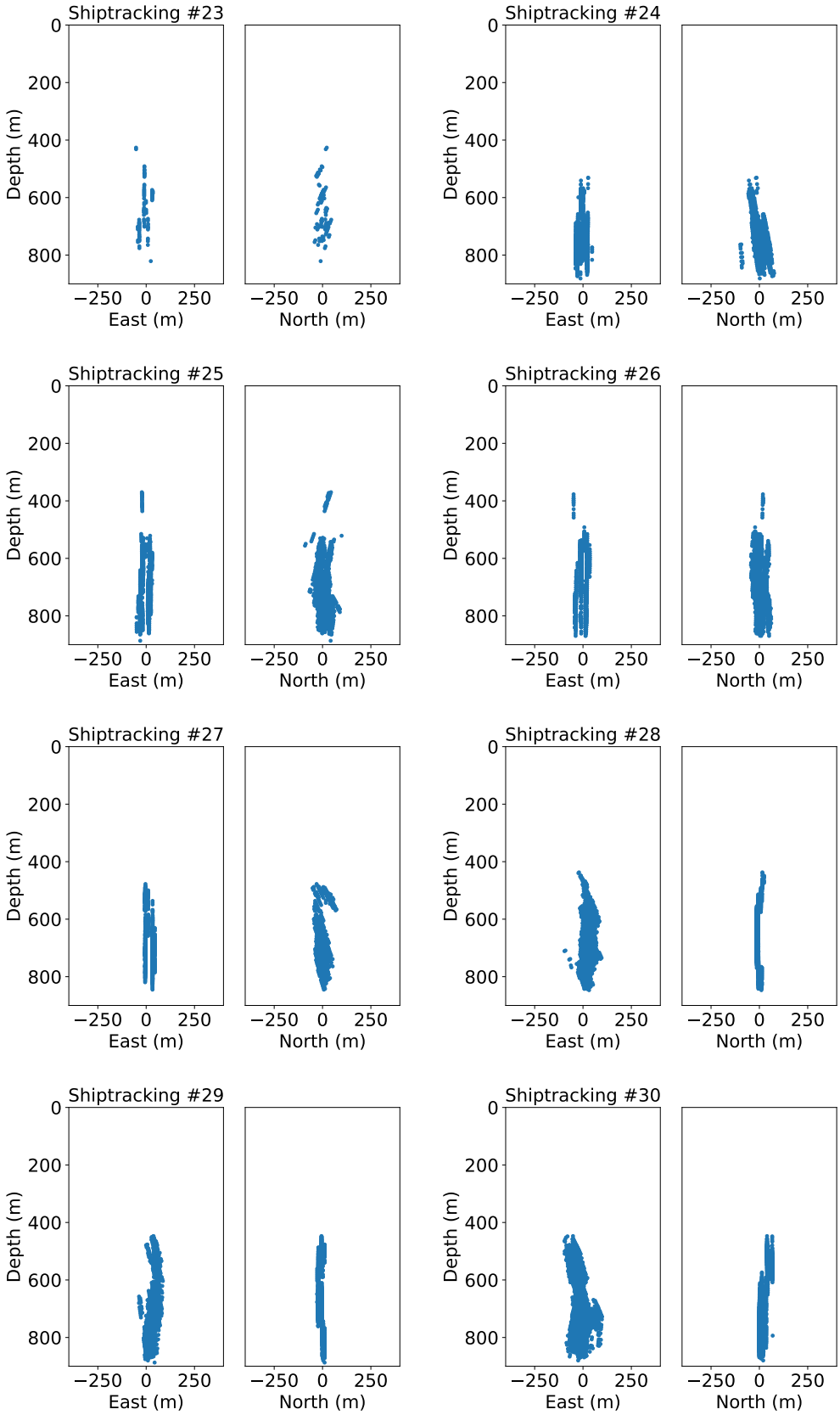

Figure A.2: Continued

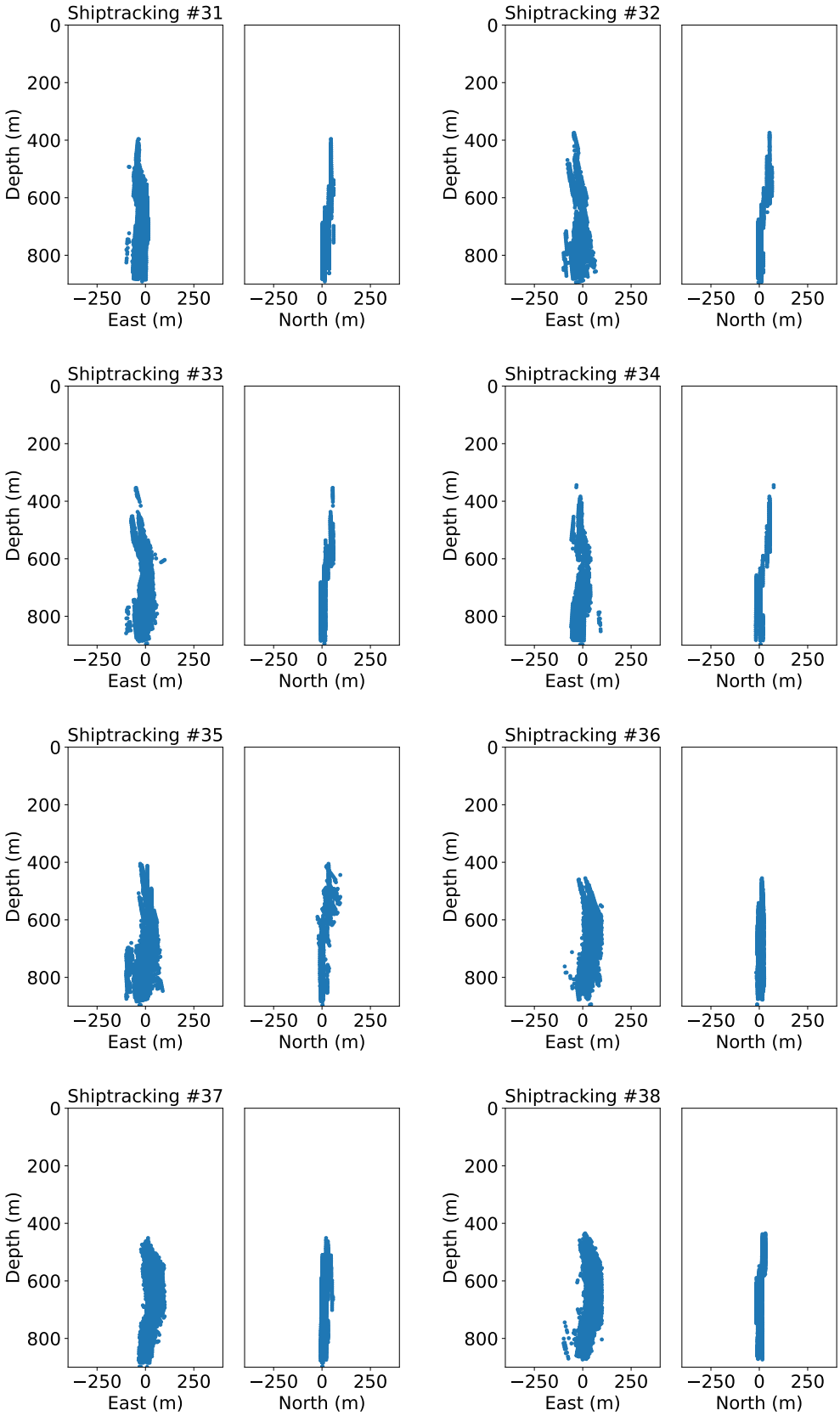

Figure A.2: Continued

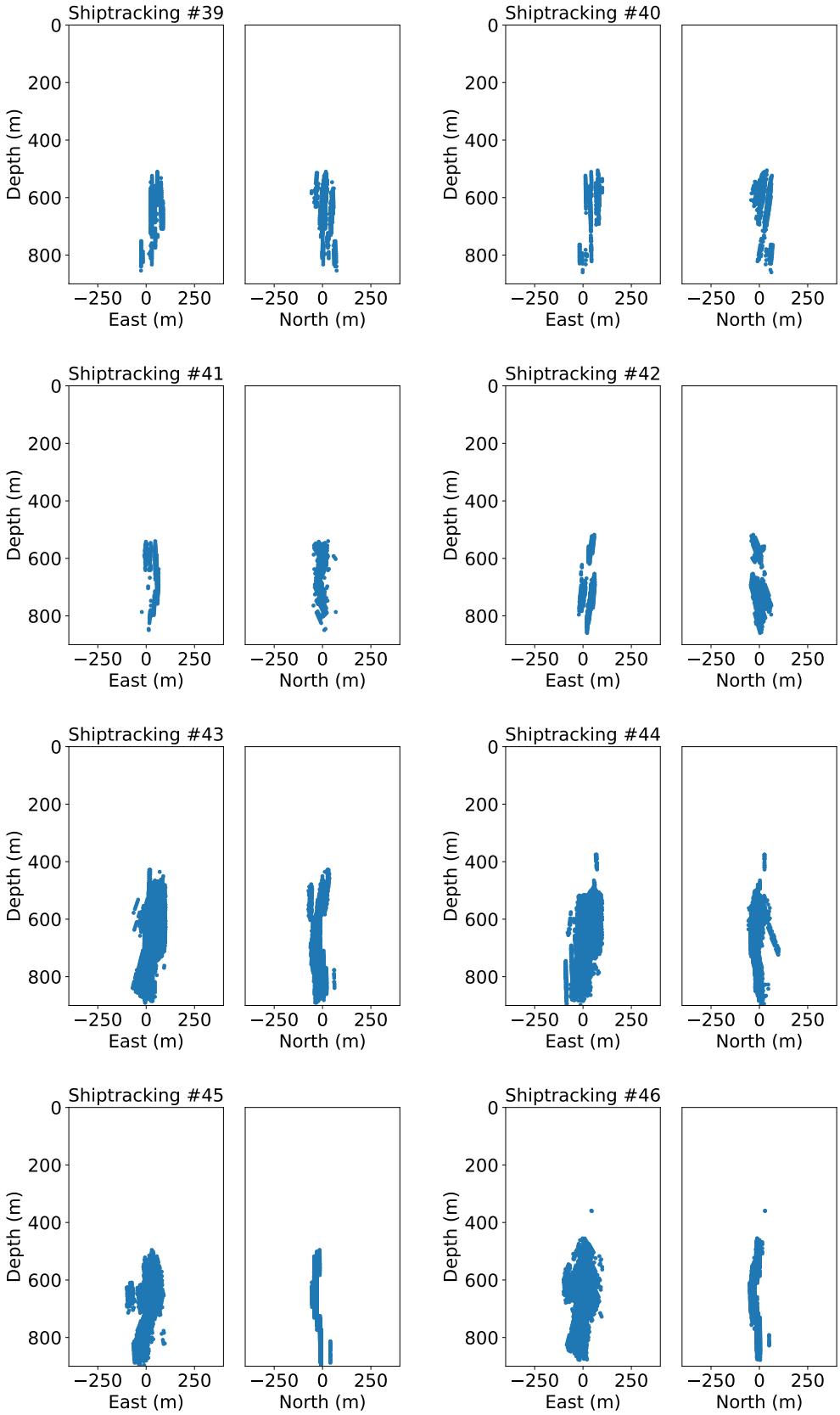

Figure A.2: Continued

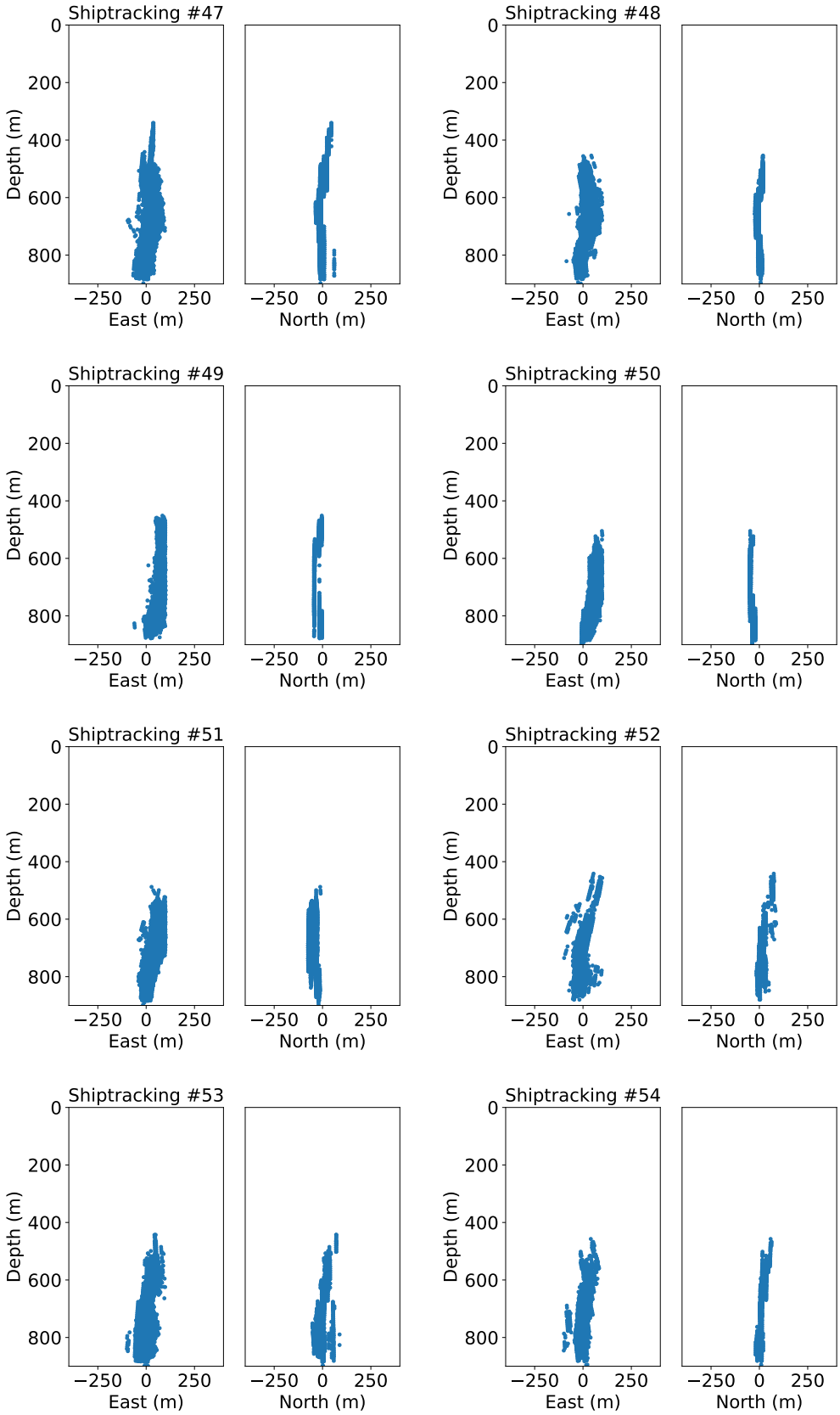

Figure A.2: Continued

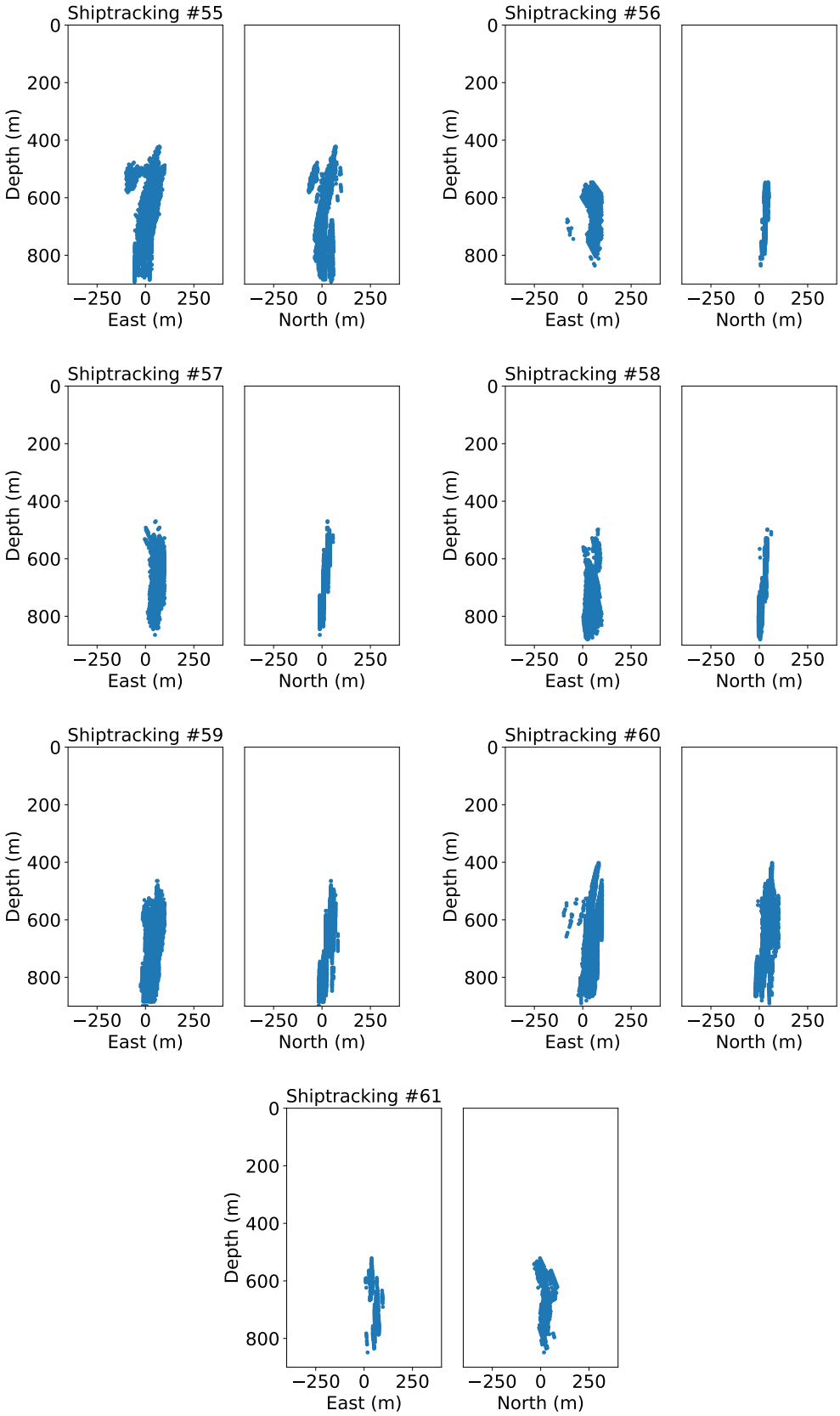

Figure A.2: Continued

A.1.3 Categorized Trajectories of Seep Bubbles

We categorize the trajectory of seep bubbles based on the measurement time and the shape of acoustic anomalies. The trajectories of bubbles are categorized within 2 –3 hours of a period. Table A.2 explains the information of the defined categories in this study, and Figure A.3 shows the categorized trajectories of bubbles from the Sleeping Dragon vent during the G08 cruise.

Table A.2: The defined categories for acoustic surveys in G08 cruise.

Category	Shiptracking	Date	Time
1	1 – 3	20150410	16:27:57 – 18:03:28
2	4 – 6	20150411	06:40:39 – 08:37:57
3	7 – 13	20150411	08:46:39 – 11:56:25
4	14 – 18	20150411	13:30:01 – 15:48:39
5	19 – 21	20150413	05:59:46 – 07:58:21
6	22 – 27	20150413	08:08:11 – 11:03:22
7	28 – 29	20150413	11:10:11 – 12:22:56
8	30 – 35	20150414	01:30:01 – 04:55:28
9	36 – 38	20150414	08:03:54 – 09:53:23
10	39 – 42	20150414	10:08:49 – 12:34:58
11	43 – 46	20150416	02:44:54 – 04:46:11
12	47 – 48	20150416	05:54:38 – 06:50:41
13	49 – 51	20150416	10:36:05 – 13:43:33
14	52 – 55	20150418	05:06:31 – 08:35:18
15	56 – 59	20150419	01:38:07 – 06:37:11
16	60 – 61	20150419	10:43:51 – 12:27:53

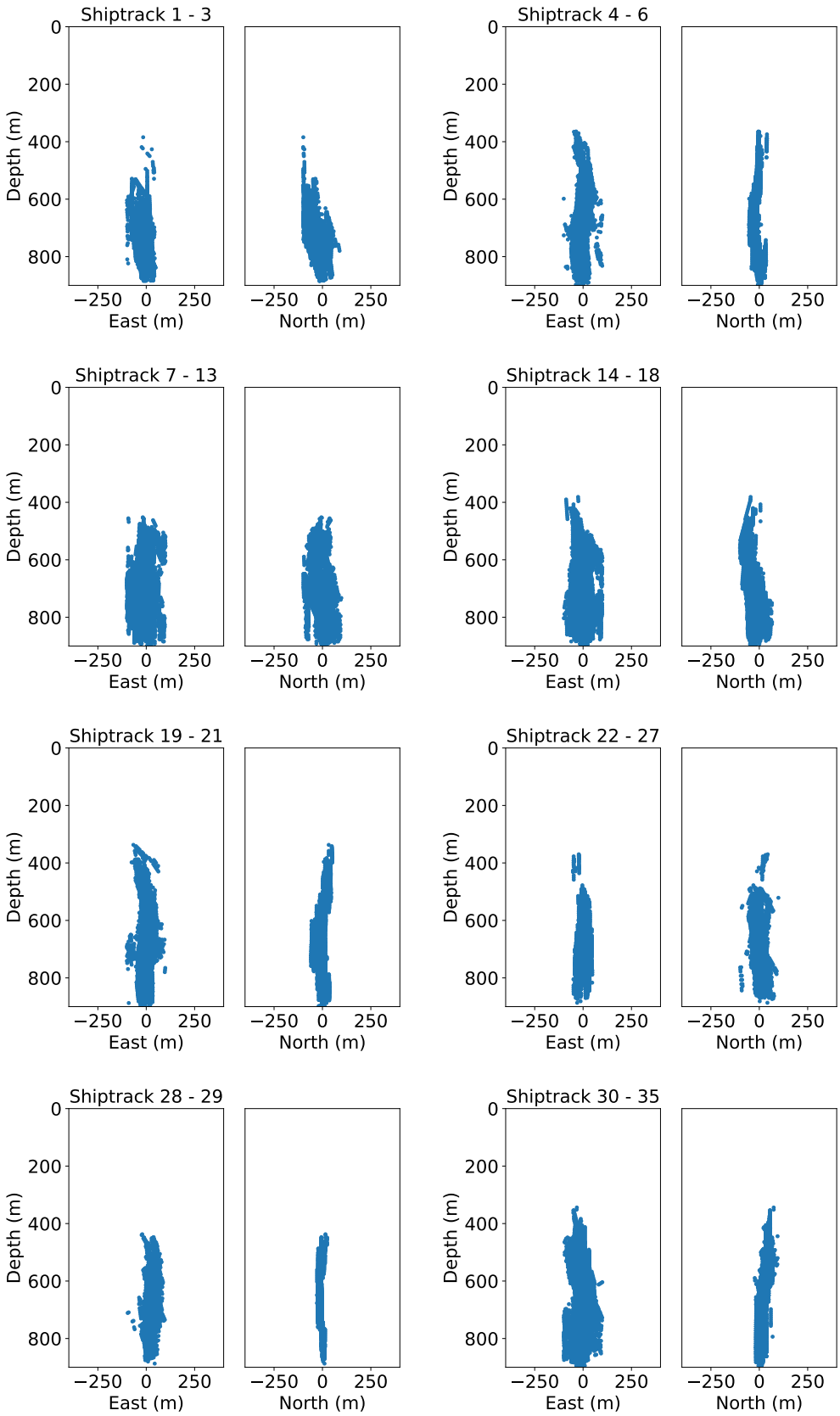

Figure A.3: Categorized trajectories of bubbles emanating from the Sleeping Dragon vent during G08 cruise.

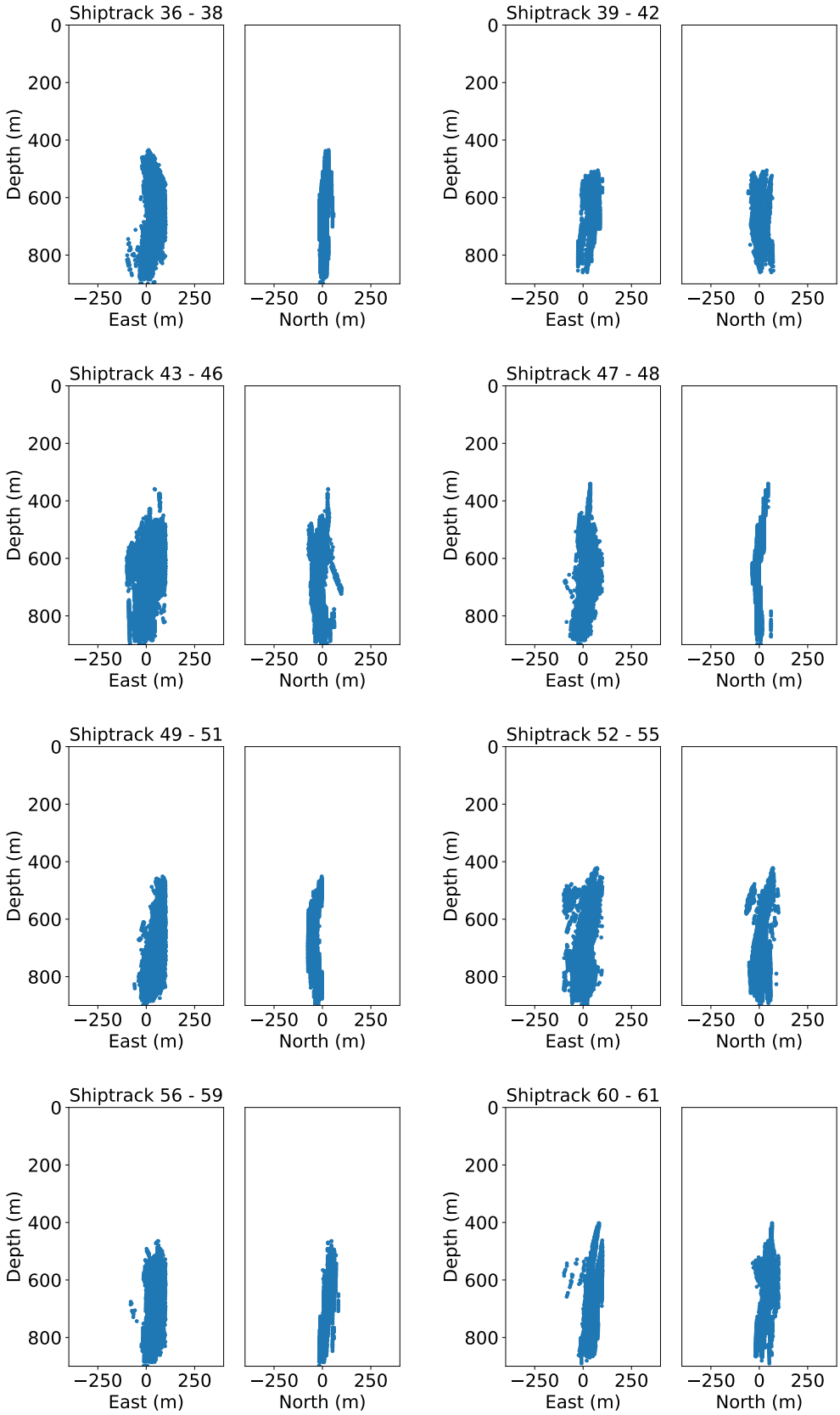

Figure A.3: Continued

A.2 Trajectory of Bubbles in G07 Cruise

Table A.3 shows the measurement time information of acoustic surveys using the Kongsberg EM 302 in G07 cruise. GISR carried out 19 acoustic surveys at the Sleeping Dragon vent site between July 19 and July 20 in 2014 during the G07 cruise.

Table A.3: The measurement time information of acoustic surveys in G07 cruise.

Shiptracking	Beginning of Measurement		End of Measurement	
	Date	Time	Date	Time
1	20140719	14:02:54	20140719	15:19:12
2	20140719	15:27:52	20140719	16:02:38
3	20140719	16:12:20	20140719	16:47:18
4	20140719	16:56:23	20140719	17:29:45
5	20140719	17:38:58	20140719	18:15:27
6	20140719	18:57:54	20140719	19:39:50
7	20140719	19:49:31	20140719	20:20:12
8	20140719	20:32:11	20140719	21:02:17
9	20140719	21:12:43	20140719	21:41:44
10	20140719	21:53:13	20140719	22:53:19
11	20140719	22:58:44	20140719	23:16:11
12	20140720	17:35:17	20140720	18:06:33
13	20140720	18:17:19	20140720	18:45:57
14	20140720	19:00:50	20140720	19:27:23
15	20140720	19:35:22	20140720	20:06:07
16	20140720	20:15:17	20140720	20:40:17
17	20140720	20:46:47	20140720	21:22:02
18	20140720	21:30:52	20140720	21:59:35
19	20140720	22:09:50	20140720	22:22:41

The data handling procedures for acoustic anomalies are listed below.

- Plot the processed acoustic anomalies from EM 302 (Total 19 Cases).
- Extract the main trajectory of bubbles from the source point ($|x_0| < 250$ m and $|y_0| < 150$ m).
- Categorize all cases based on the measurement time and the shape of trajectory (4 cases).

A.2.1 Processed Acoustic Anomalies

Figure A.4 shows the measured acoustic anomalies in the x-y coordinate system at the MC 118 site during the G07 cruise.

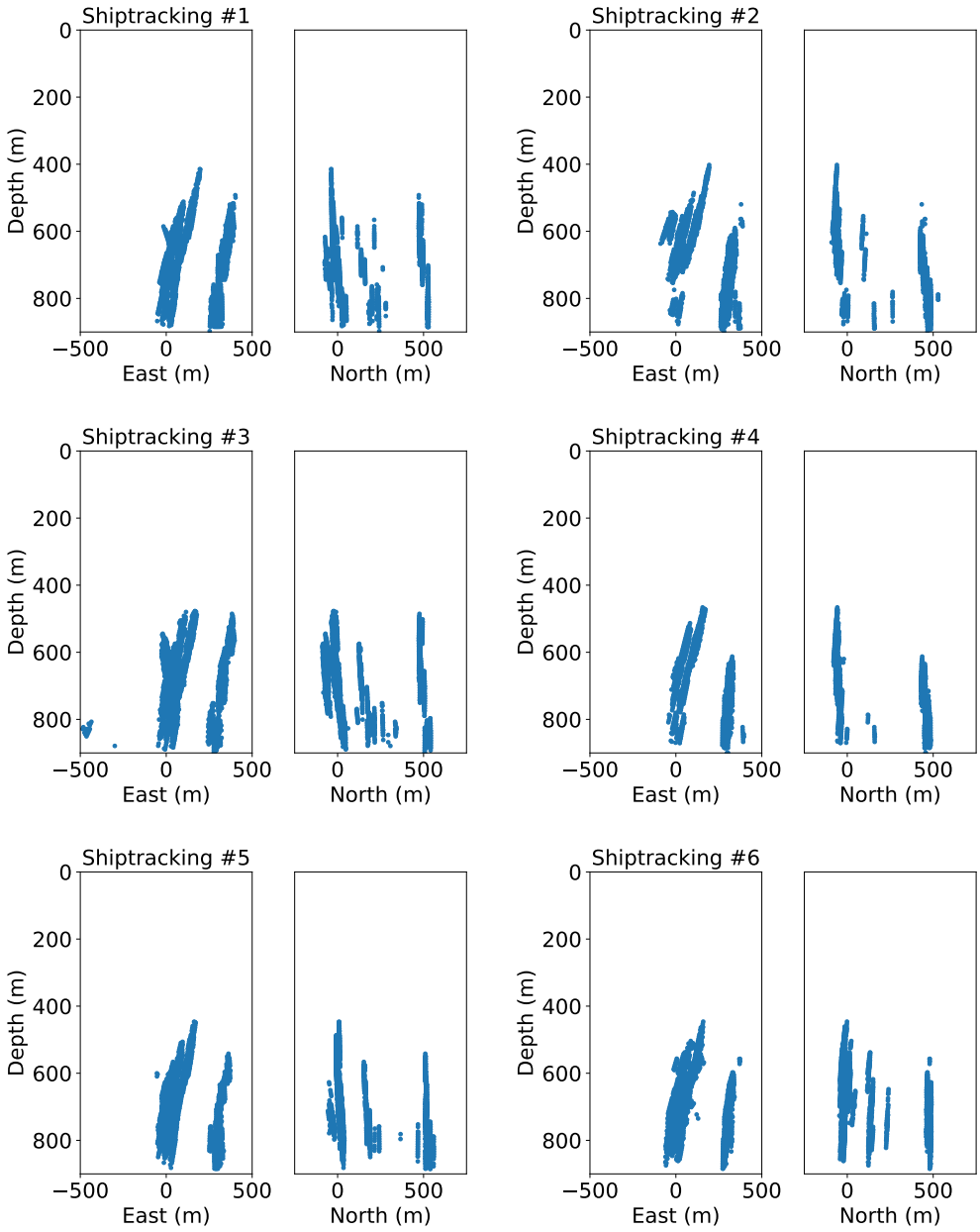

Figure A.4: Acoustic anomalies measured by EM 302 at MC 118 site during G07 cruise.

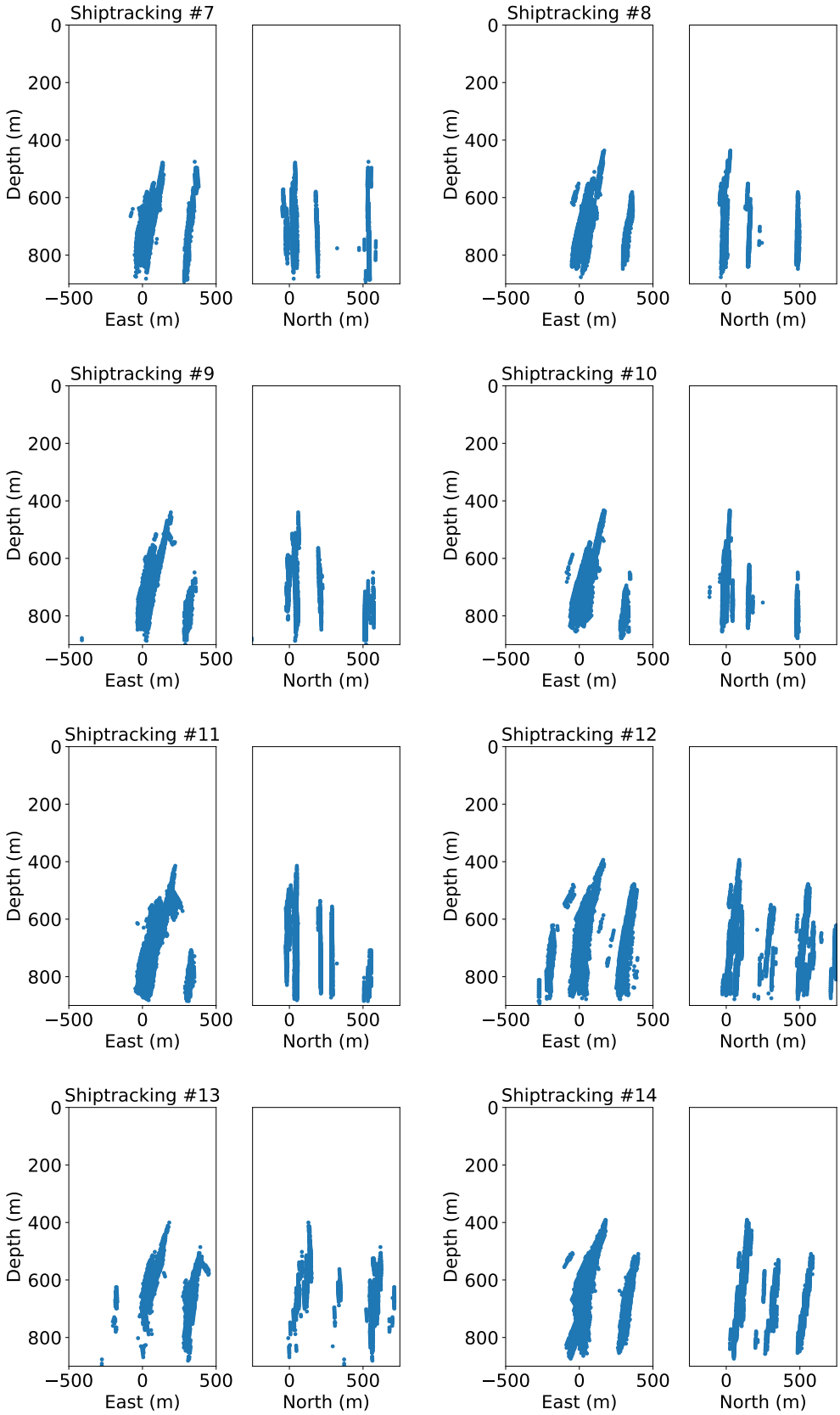

Figure A.4: Continued

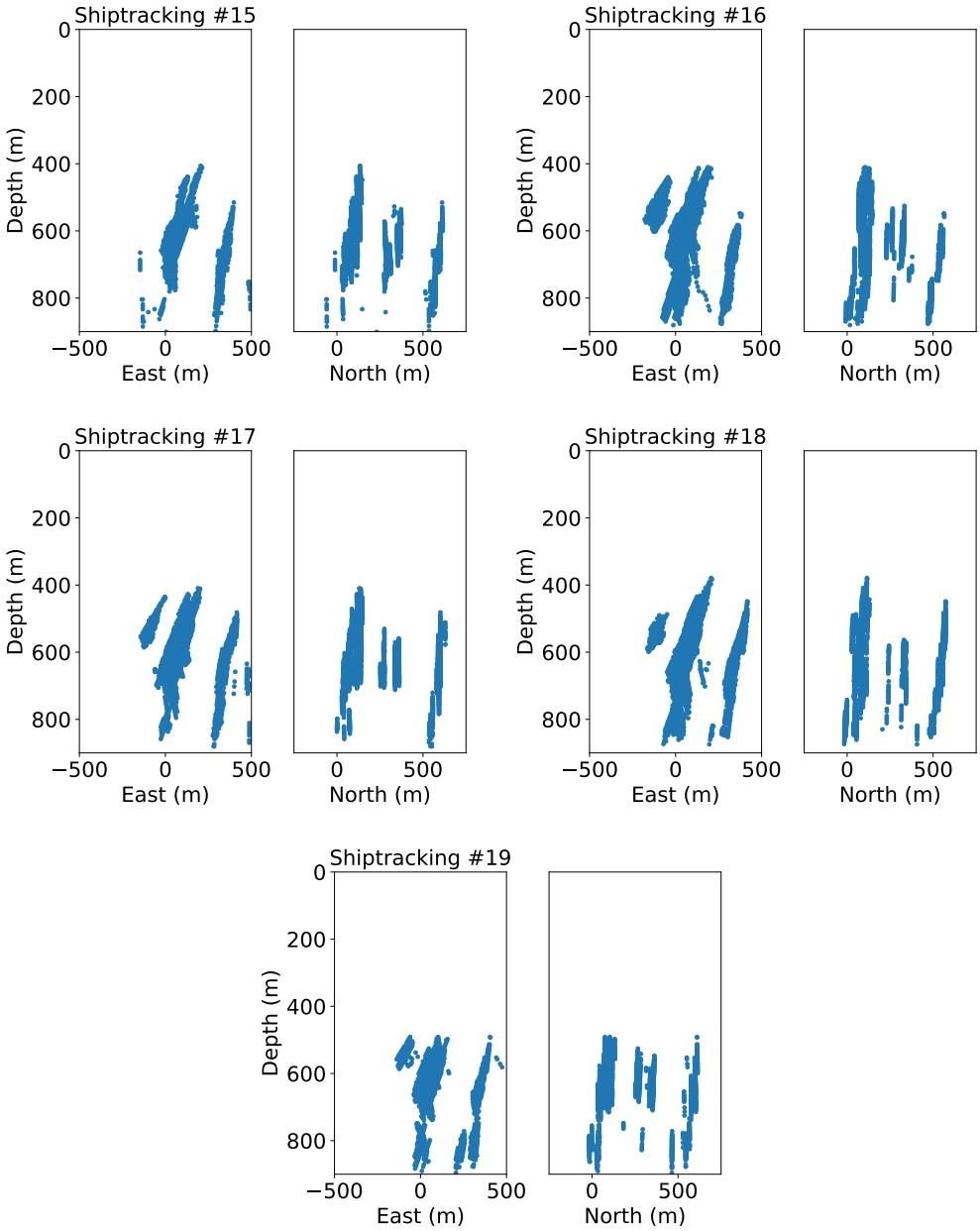

Figure A.4: Continued

A.2.2 Main Trajectories of Bubbles

Figure A.5 shows the main trajectories of bubbles from the Sleeping Dragon vent during the G07 cruise.

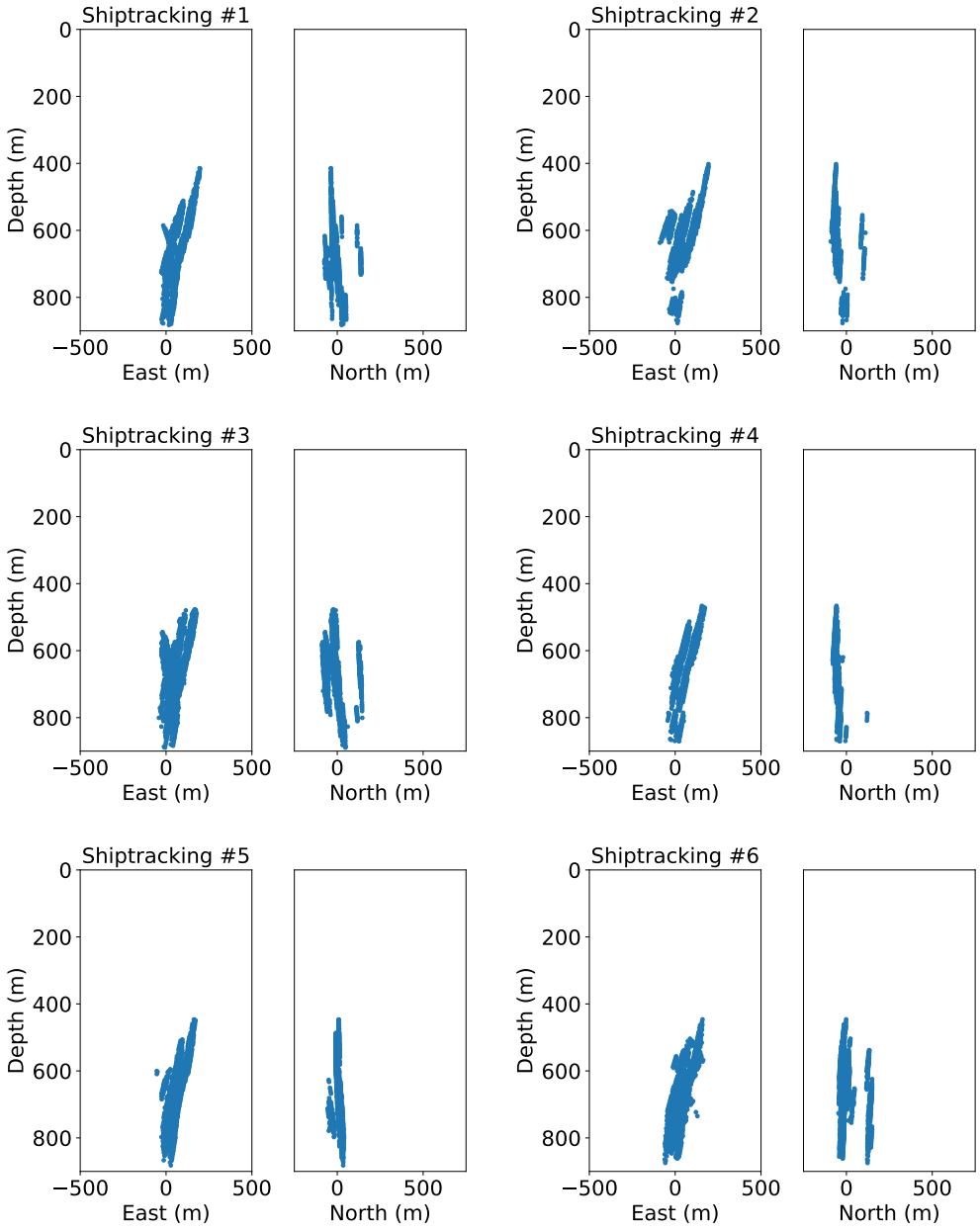

Figure A.5: Main trajectories of bubbles emanating from the Sleeping Dragon vent during G07 cruise.

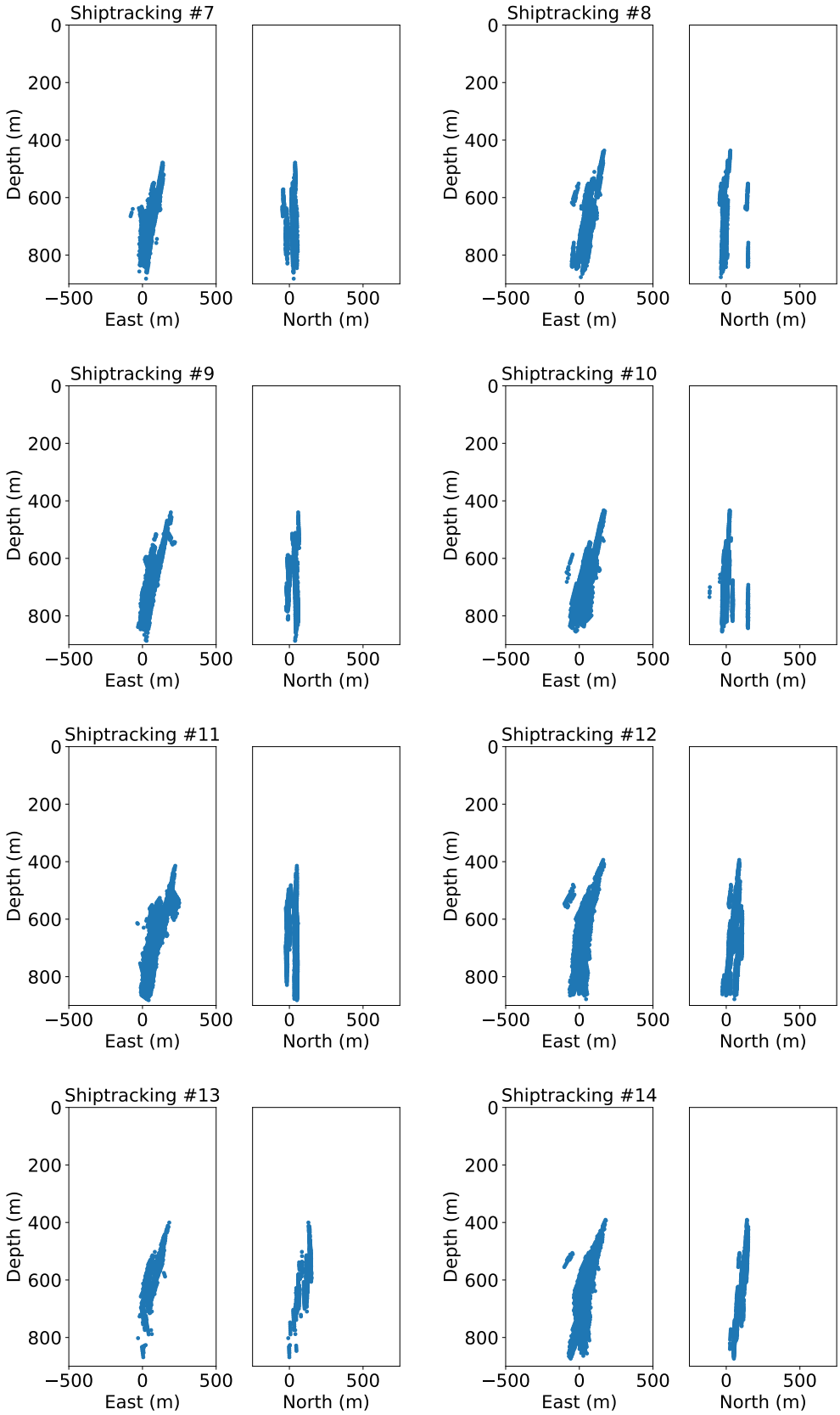

Figure A.5: Continued

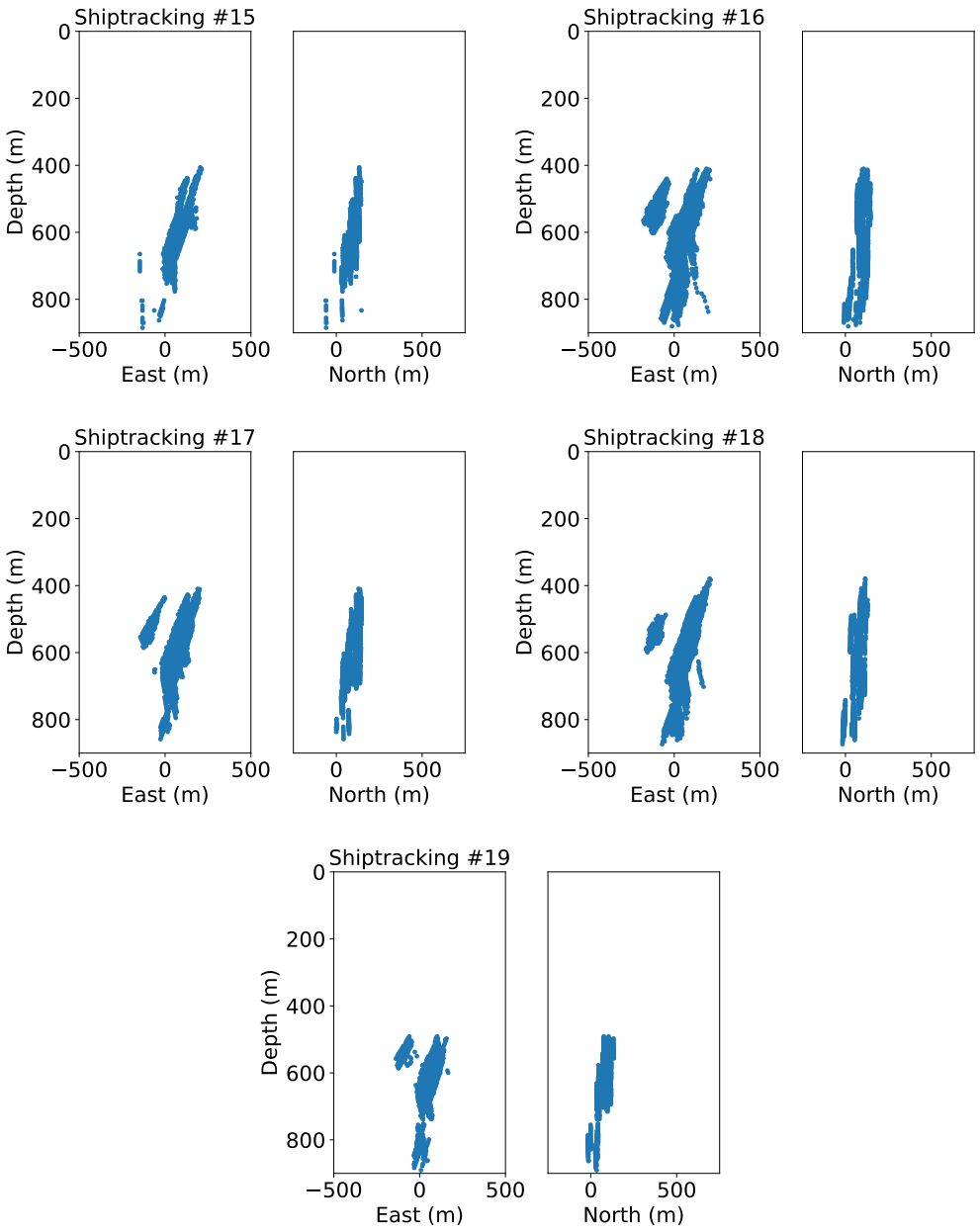

Figure A.5: Continued

A.2.3 Categorized Seep Trajectories

We categorize the trajectory of seep bubbles based on the measurement time and the shape of acoustic anomalies. Table A.4 explains the information of the defined categories in this study, and Figure A.6 shows the categorized trajectories of bubbles from the Sleeping Dragon vent during the G07 cruise. However, the measured current data for the ship-tracking from 12 to 19 are missing. We only focused on the ship-tracking data from 1 to 18 for the simulation.

Table A.4: The defined categories for acoustic surveys in G07 cruise.

Category	Shiptracking	Date	Time
1	1 – 2	20140719	14:02:54 – 16:47:18
2	3 – 5	20140719	16:56:23 – 18:15:27
3	6 – 7	20140719	18:57:54 – 20:20:12
4	8 – 11	20140719	20:32:11 – 23:16:11

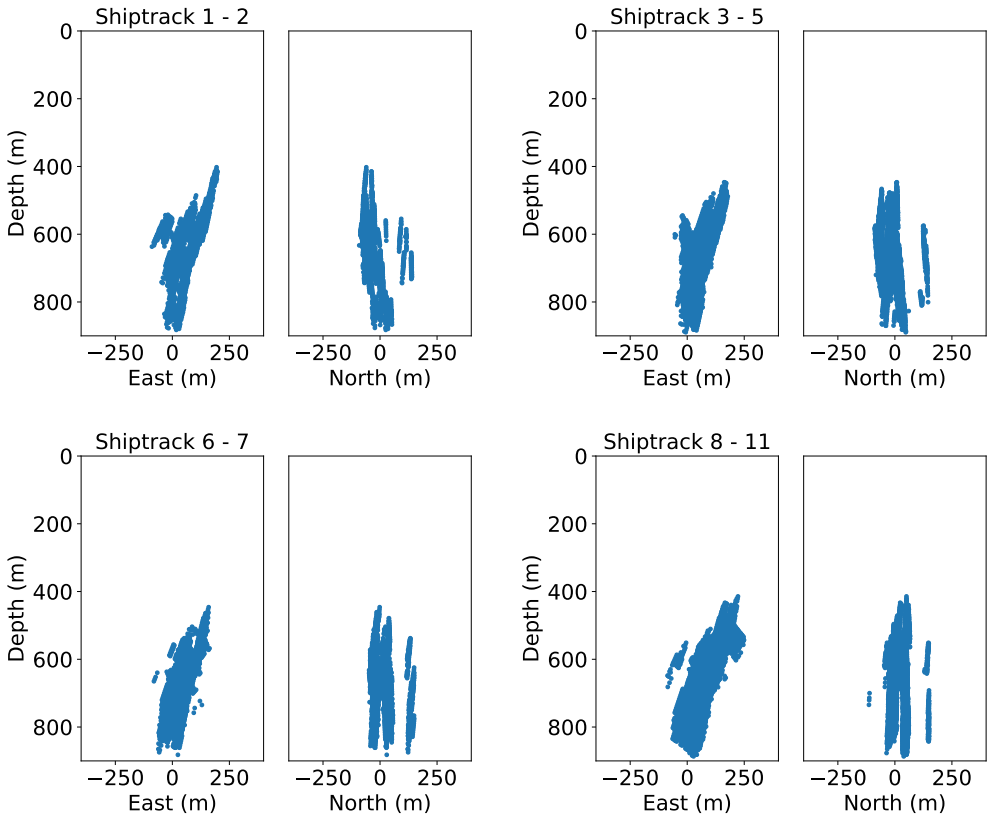

Figure A.6: Categorized trajectories of bubbles emanating from the Sleeping Dragon vent during G07 cruise.

APPENDIX B

HORIZONTAL SPREADING OF BUBBLES IN THE NATURAL SEEPS IN GISR CRUISE

B.1 M3 Sonar Images in G08 Cruise

We use the M3 acoustic images to qualitatively evaluate the transport characteristics of the bubbles. Figure B.1 shows the measured acoustic images of the M3 at the MC 118 site from the G08 cruise. GISR measured the horizontal bubble spreading at the certain water depth by using the M3 sonar. The intensity of the signal in the image depends on the bubble size, the measuring depth, and the frequency level of the equipments. The raw image only can be displayed with the *jet* or *copper* colormap.

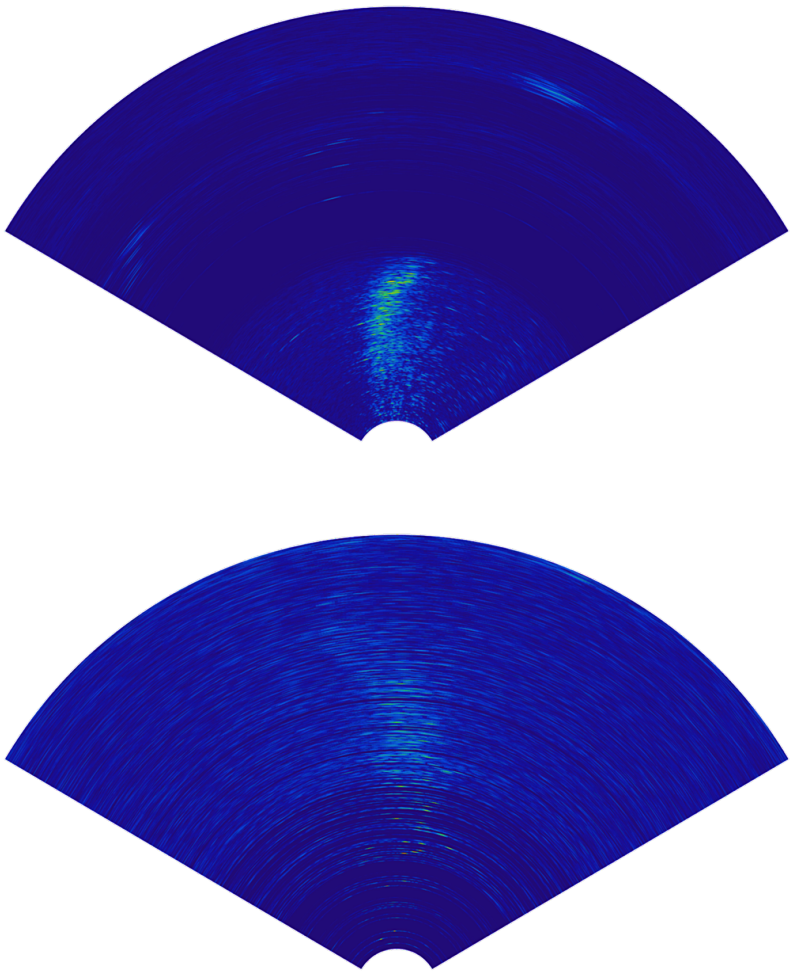

Figure B.1: Observed acoustic images by M3 sonar at MC 118 site during G08 cruise with the *jet* colormap (Case: H1402, H1404, H1406, H1407_1 and H1407_2.)

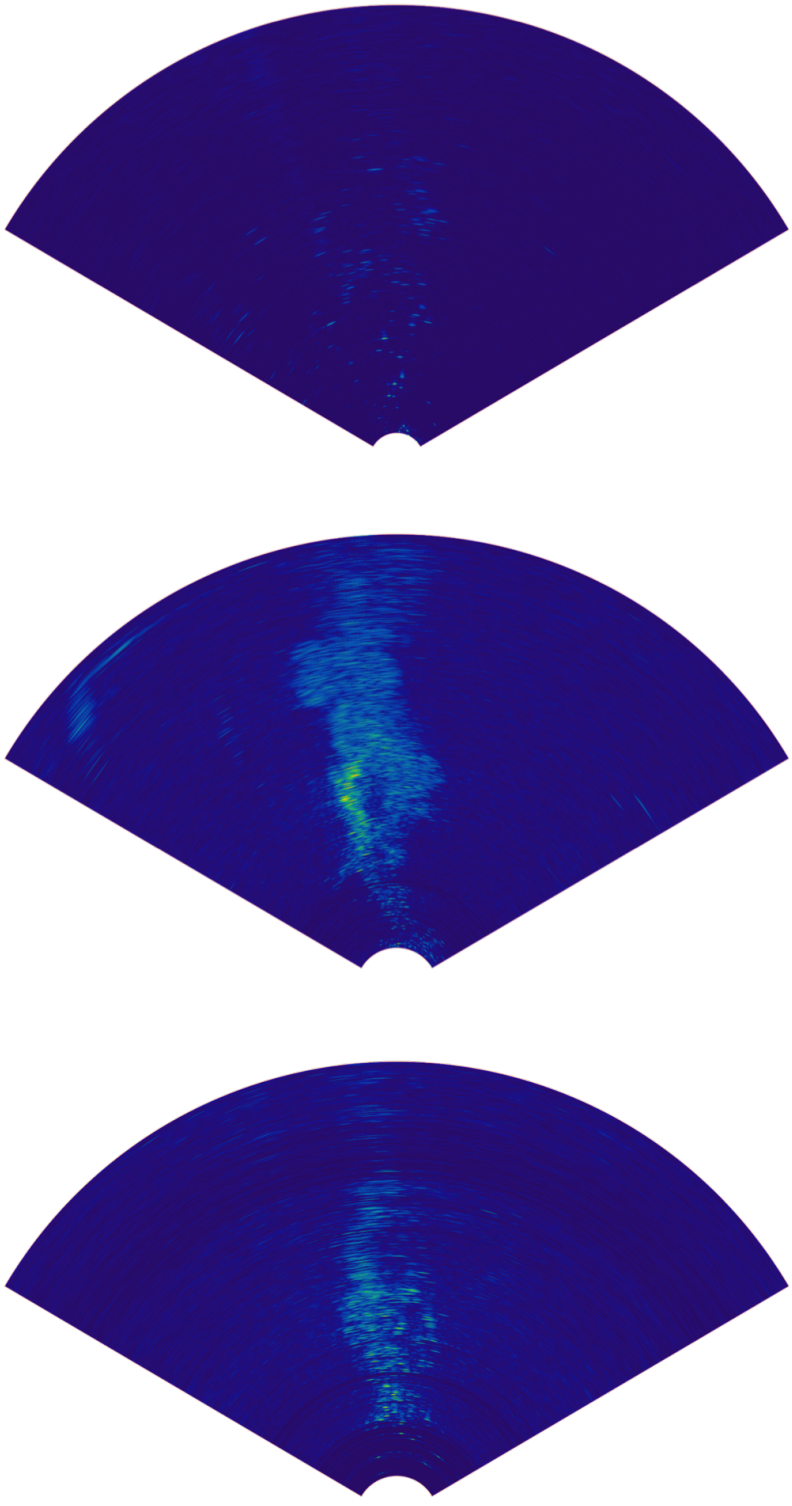

Figure B.1: Continued